FORSCHUNGSZENTRUM
ROSSENDORF e.V.

FZR

Archiv-Ex.:

FZR 93 - 06
March 1993

INSTITUTE OF ION BEAM PHYSICS AND MATERIALS RESEARCH

Annual Report 1992

Content

1. Introduction 4

2. Scientific contributions

On the Mechanism of Carbon-Induced Doping in Implanted Silicon
W. Skorupa, M. Voelskow, K. Schmalz, G. Morgenstern, and P. Gaworzewiski 7

Iron Gettering by MeV-Carbon Implantation
W. Skorupa, R. Kögler, M. Voelskow, and K. Schmalz 9

Formation of Buried $(Fe_{1-x}Co_x)Si_2$ Layers in (100)Si by Ion Beam Synthesis
D. Panknin, E. Wieser, W. Skorupa, G. Querner, H. Vöhse, J. Albrecht, and
W. Henrion 10

Investigation of Pulsed Ion Beam Induced Amorphization/Crystallization of Silicon for Irradiation with Kr^+ Ions of 3.8 MeV
R. Kögler, V. Heera, W. Skorupa, E. Glaser, T. Bachmann, and D. Rück 12

Computerprogram for Calculating Reflectivities of Multi-Layer-Systems
Th. Henkel and V. Heera 14

A Formula for Estimating IBIEC/IBIIA-rates on Silicon
V. Heera 16

High Current FIB System for Micromechanics Application
L. Bischoff, E. Hesse, G. Hofmann, W. Probst, B. Schmidt, and J. Teichert 18

Preparation of the IMSA-100 for Ion Beam Synthesis Purposes
L. Bischoff and J. Teichert 20

Development of a Cobalt Liquid Metal Ion Source
E. Hesse and J. Teichert 22

Two Concentric Emission Bundles From a Lithium Liquid Metal Ion Source
E. Hesse and F.K. Naehring 23

Investigations of the Electrochemical Etch Stop on Silicon Using KOH
B. Schmidt 25

Electrochemical Etch Stop Behaviour on Ion Implanted Silicon pn-Junctions
B. Schmidt 27

A Measurement System for Studying Electrochemical Field Effect Ion Sensitivity
M.T. Pham, W. Taubert, and M. Bürger 29

An Approach to the Cross Sensitivity of the Ion Sensing Membranes
M.T. Pham and S. Howitz 31

ISFETs with Controlled Gate Membrane Opening
M.T. Pham and S. Howitz 33

Ion Beam Modified Insulator Layers as ISFET Membranes for Heavy Metal Ion Detection
J. Hüller, W. Hoffmann, and M.T. Pham 35

Differential Measurements with ISFETs in Microfluid Systems
M.T. Pham and S. Howitz 37

Cooperative Project "Fluidic- ISFET- Microsystem"
S. Howitz and M.T. Pham 39

Depth Profiles of C, N, and O on Carbon Coated Steel Surfaces Made by IBAD
A. Kolitzsch, E. Hentschel, and E. Richter 42

High Dose Implantation of Aluminium into Iron
H. Reuther, O. Nikolov, S. Krujer , R. A. Brand, and W. Keune 45

A Magnetron Source for Ion Implantation
H. Reuther 48

Modelling of Implantation-Induced Transient Diffusion and Electrical Activation of Boron in Crystalline Silicon during Post-Implantation Annealing
H. U. Jäger 50

Computer Simulation of Channeling Implantation of Phosphorus into Silicon
M. Posselt 53

Dielectric Theory of Electronic Energy Loss in a Homogeneous Electron Gas: Effect of First Order Polarization
R. Mathar 56

Molecular Dynamics Simulations of Defect Formation by Low-Energy Ion Bombardement
D. Stock and K.H. Heinig 59

Thermalization in Collision Cascades Investigated by Molecular Dynamics Calculations
K.-H. Heinig and D. Stock 61

Compression Waves Induced in Si by Low-Energy Ions - a Molecular Dynamics Simulation
K.-H. Heinig and D. Stock 63

Molecular Dynamics (MD) Simulations of GRID Experiments
K.-H. Heinig and D. Janssen 64

The Diffractometer of the RCR at the Rez Reactor
A. Mücklich, M. Betzl, P. Reichel, and W. Boede 67

Neutron Diffraction Analysis of Substructures in Polycrystalline Materials
P. Klimanek, T. Kschidock, A. Mücklich, P. Lukás, P. Mikula, and M. Vrána 69

Study of Hardening Portland Cement Paste by Small-Angle Neutron Scattering
F. Eichhorn, F. Häußler, and H. Baumbach 72

Studies of $Sr_xBa_{1-x}Nb_2O_6$ Mixed Crystals by Neutron Diffraction at Temperatures between 15 K and 293 K
F. Prokert and B.N. Savenko 74

The Neutron Time-of-Flight Diffractometer NSHR at IBR-2 in Dubna
J. Heinitz, K. Ullemeyer, and K. Walther 76

7.25 GHz ECR Source for Highly Charged Ions
R. Hentschel, H. Tyrroff, L. Friedrich, E. Huttel, and L. Wiss 79

Improvement of the Experimental Possibilities at the 2 MV Van de Graaff Accelerator
W. Bürger, M. Friedrich, R. Grötzschel, C. Neelmeijer, and S. Turuc 82

Status Report of the 3 MV Tandetron
M. Friedrich, S. Langer, S. Turuc, and E. Wieser 82

Developments for the Accelerator Control and Stabilizing Systems
W. Bürger 84

3. List of publications, conference contributions, and seminary lectures 85

4. Personnel 98

Introduction

On January 1, 1992 the Research Center Rossendorf started its work in succession of the former Central Institute of Nuclear Research. The Institute of Ion Beam Physics and Materials Research, founded in 1991, is now one of the five scientific institutes of the Research Center.
This transformation was connected with two important consequences for our institute. The permanent staff of the institute was reduced to 78 employees, among it 32 scientists. But, as a remarkable success of the first year under the new status we can report that at the end of 1992 the man power of the institute was completed by 15 positions within the framework of additionally funded projects and by 8 doctoral fellowships. Therefore a continuation of all branches of the scientific programme, reported in the status report 1991, was possible. These topics are:

- Modification of Semiconductors and Microbeam Facility
- Application of Ion Beams to Sensors
- Modification of Metals and Other Materials
- Theory of Ion-Beam Induced Processes in Solids
- Fundamentals of Ion-Solid Interaction and Ion Beam Analysis
- Structure Studies Using X-Rays and Neutron Scattering.

A much more serious problem was the missing permission to operate our ion beam accelerators. Only from November 1992 experiments using the implanters were possible. The restart of the electrostatic accelerators is expected for February 1993.
Therefore the scientific output of the experimental departments was limited to the evaluation of data available from the foregoing year. In some special cases we were able to use beam time in external laboratories. With this respect we gratefully acknowledge the help of the accelerator laboratory of TU and LMU Munich (W. Assmann, A. Weidinger), of the GSI Darmstadt (D. Rück), and of the Technical University Chemnitz.

The following introductory review of some main results obtained in the research fields mentioned above proves that also this complicated year may be considered as an important step forwards in the development of the new institute to an efficient center for the use of ion beam techniques in materials research.

During the last year the activities in the field "Ion Beam Modification of Semiconductors and Microbeam Facility" were mainly concentrated on the investigation of samples already prepared in 1991.
For the first time, ion beam synthesis was used to study the formation of buried Fe-Co silicide layers. This was done in order to continue the recent work on the formation of $FeSi_2$ with respect to a possible band gap engineering of the semiconducting β-$FeSi_2$ phase.

The investigation of proximity gettering of iron by MeV-carbon implantation was also continued. Beside the gettering behaviour doping effects due to carbon were studied.
Experimentally determined rates of ion beam induced epitaxial crystallization (IEBIC) were compared with the results of computer modelling. Concerning the basic mechanism this comparison favours the effect of point defect diffusion to the interface.

First experiments carried out at a RFQ accelerator of the GSI Darmstadt led to interesting results on the influence of pulsed ion irradiation on the IBIEC process.
The activities at the microbeam facility were mainly devoted to an overall testing of the apparatus. Final test experiments at a lithium-ion source were performed and a Co-Nd alloy was tested in order to get a Co beam from a liquid metal ion source.

The work of the department of "Application of Ion Beams for Sensors" can be devided into the three topics radiation sensors, chemical microsensors and micromechanics.
One main task was the development of special processes for the fabrication of HP-Ge detectors like the formation of n^+ layers by phosphorus implantation, the preparation of amorphous germanium layers for passivation and contacts by sputtering and the investigation of the growth of germanium oxide during chemical preparation and annealing.
The investigation of ion beam synthesis of chalcogenide glasses and of their sensibilization for the detection of heavy metals by ion sensitive field effect-transistors (ISFET) was continued. A very important event was the start of a new project with the aim to develop an integrated microsystem of ISFET and microfluidic components for the dynamical measurement of ion concentrations in liquids.
The activities in the field of micromechanics were devoted to the realization of sub-μm silicon membranes by anisotropic etching and the development of an electrostatic valve in silicon technique.

Due to the lack of ion beams the work of the department "Ion Beam Modification of Metals and Other Materials" was mainly concentrated on the improvement of the experimental equipment.
The construction of the apparatus for ion beam assisted deposition (IBAD) was completed and the main components of the new implanter "Scanibal" were successfully tested.
Important improvements were obtained considering the equipment for materials testing. A profilometer, a scratch tester, an ultramicrohardness tester and the reconstructed wear tester were taken into operation.
The investigations with the aim to use ultrasonic surface waves in order to study thin film properties were continued with an improved detection system by first experiments on TiN layers on steel. The evaluation of IBAD experiments from 1991 where hard and wear resistant carbon layers were formed by C^+ implantation into a growing carbon layer led to a deeper insight into the acting mechanism.

The activities of our group "Theory of Ion Beam Induced Processes in Solids" were continued with investigations on the interaction of ion beams with materials during implantation and on subsequent re-ordering processes including the development of new theoretical methods as well as collaboration with the experimental groups. A few extensive computer codes were developed to simulate (i) the slowing down of ions in crystalline targets in the framework of the binary collision approximation, (ii) the slowing down of low-energy ions by molecular dynamic calculations, and (iii) the coupled diffusion of impurities and point defects in solids. In the last year the physical problems treated in this way were:

(i) Channeling effects in high and medium energy implantation into silicon,
(ii) MD calculations of the thermalization and defect generation in collision cascades as well as simulations of gamma-ray induced Doppler broadened (GRID) spectra,
(iii) implantation induced transient enhanced diffusion and electrical activation of boron in crystalline silicon during post-implantation annealing.

In 1992 the situation for the department "Fundamentals of Ion-Solid Interactions and Ion Beam Analysis" was especially difficult due to the missing permission to operate the accelerators. Therefore the activities were concentrated on apparative work originally scheduled for a later date.
Thus a new beamline for hydrogen depth profiling by resonance reactions (^{15}N, ^{19}F beams) was designed and assembled. It allows, by a combination of beam sweeping and focusing, a homogeneous irradiation of large area spots on the target in order to minimize hydrogen redistribution.
The reconstruction of the ERDA scattering chamber was completed by the installation of the PC based multiparameter data acquisition system for the Bragg ionization chamber and the dE-E-SSD telescope. This dedicated telescope for recoil atoms of hydrogen isotopes could be tested at the ERDA facility of the Munich MP tandem.
At the 2 MV Van de Graaff accelerator the installation of the switching magnet and the differentially pumped beam line to the UHV scattering chamber was finished.

The department for "Accelerator Technique" used this year mainly for technical improvements of the 5 MV tandem accelerator and here especially for the automatic control of ion source, for the stabilization of the acceleration voltage and for upgrading the radiation safety equipment. This gives the possibility of routine operation with reduced staff.
Extensive work was done in order to reconstruct parts of the tandem building for the installation of the new 3 MV tandetron which is expected for spring 1993.

The most important task for the department "Structure Studies Using X-Ray and Neutron Scattering" was the transfer of neutron scattering equipment from our closed research reactor to external reactor facilities and the extension of the X-ray laboratory in our institute including the installation of new equipment.
A multipurpose neutron diffractometer was installed and tested at the research reactor in Rez near Prague. From autumn 1992 it is in cooperative use together with the TU MA Freiberg for texture studies of alloys, with the Center for Geo Research Potsdam for geological texture investigations and with the TU Chemnitz for structure investigations of melts.
The preparation of an improved double crystal neutron diffractometer for fundamental studies and small-angle scattering experiments for its transfer to the reactor of the Hahn-Meitner-Institute in Berlin was finished.
The time-of-flight neutron diffractometer at the pulsed reactor of the Joint Institute for Nuclear Research in Dubna was in successful operation. Our small group in Dubna investigated about 50 samples from the universities in Göttingen, Rostock, Chemnitz and Berkeley, from the RWTH Aachen and the Center of Geo Research Potsdam. Texture problems of geological samples were the dominating subject of these studies. By our presence in Dubna it was also possible to use the small-angle scattering equipment MURN and the single-crystal diffractometer DN-2.

E. Wieser

On the Mechanism of Carbon-induced Doping in Implanted Silicon

W. Skorupa, M. Voelskow, K. Schmalz[1], G. Morgenstern[1] and P. Gaworzewski[1],

[1]Institute for Semiconductor Physics, POB 409, O-1200 Frankfurt, Germany

Recently, it was shown that the carbon induced donor formation has a maximum concentration at a dose of 10^{15} cm^{-2} [1]. On the other hand, a dose of 10^{13} cm^{-3} does not show any doping effect. This was confirmed by our new results after 5 MeV carbon implantation in that donor formation sets in at 3x10^{13} cm^{-2} and the electrical activation grows increasing the carbon dose to 10^{15} cm^{-2} [2]. For this dose the carrier concentration profile of a CZ- and a FZ-wafer is shown in Fig.1. The profile of the CZ-wafer shows a Gaussian-like shape with a projected range of 4.9 μm. The maximum carrier concentration is 2x10^{16} cm^{-3} subtracting the basic concentration of the wafer. This results, comparing with the maximum atomic concentration measured by SIMS (see Fig.2) of 10^{19} cm^{-3}, in an electrical activation of only 0.2 %. The carrier concentration of the FZ-wafer is distinctly lower and shows a broad distribution. The maximum lies also at the projected range of the other curve, but this profile is further characterised by a broad tail towards the surface. The electrical activation is distinctly lower than for the CZ-material (0.002 %).

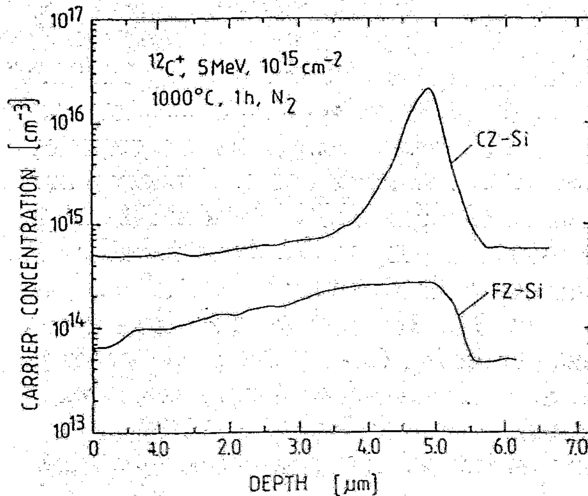

Fig.1:
Carrier concentration profiles evaluated from spreading resistance measurements after carbon implantation and annealing of Czochralski-grown (CZ)- and Float zone-grown (FZ)-silicon wafers.

The SIMS measurements of the atomic profiles after implantation at 5 MeV with a dose of 10^{15}cm^{-2} showed exactly the same carbon profiles independently on the material type - CZ or FZ - or the annealing state - as implanted or annealed at 1000°C. Two of these atomic profiles for CZ- and FZ-material after annealing are shown in Fig. 2. This suggests, the distinctly higher activation in the CZ-material must be caused by the higher oxygen content. The profile tail measured in FZ-material directed to the surface is not caused by any difference of the measureable carbon concentration profiles taking into account that the detection limit of SIMS for carbon is about 10^{17} cm^{-3}. At present, the reason for the seemingly higher carbon level of about 10^{18} cm^{-3} behind the profile is not yet clear.

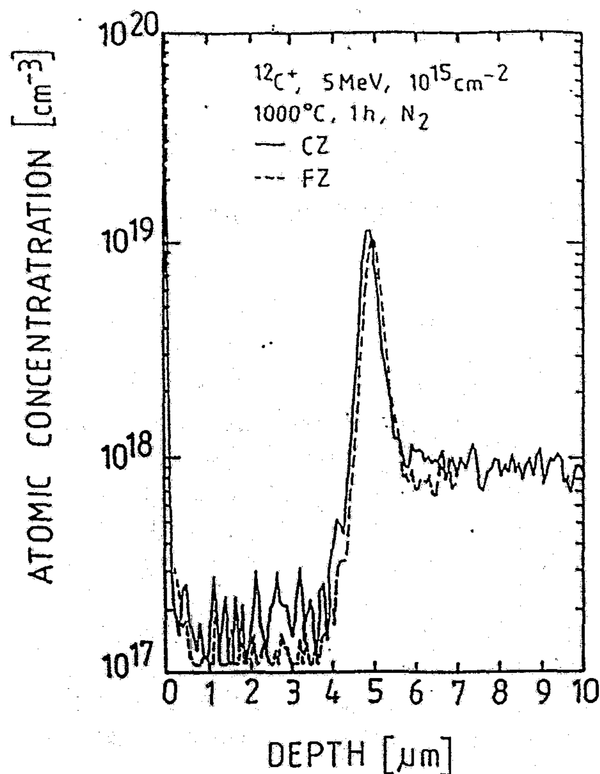

Fig.2:
SIMS profiles of the carbon concentration after carbon implantation and annealing of Czochralski- grown (CZ)- and Float zone-grown (FZ)-silicon wafers.

The question arises if the introduction of implantation damage alone in CZ- as well as in FZ-silicon material leads also to a doping effect, especially in the presence of oxygen. For this end we implanted both Si-material types with 12.5 MeV silicon ions with the same doses as carbon. The choice of the implantation energies - 5 MeV for carbon and 12.5 MeV for silicon - was made to ensure nearly the same projected range of about 5 μm. Moreover, this leads to a comparable energy deposition into electronic and nuclear processes in the same depth regions. In contrast to the results after carbon implantation and annealing at 1000°C, no doping effect was found in the wafers implanted with silicon ions independently on the dose ($3x10^{13}$-$3x10^{15}$ cm^{-3}) or the oxygen content of the wafers (10^{16} cm^{-3} for FZ, 10^{18} cm^{-3} for CZ). This points emphatically to the fact, that the carbon induced doping effect is first of all related to carbon and not to radiation damage alone, or a combination of damage and oxygen. Nevertheless, comparing the results after carbon implantation in FZ- and CZ- material, oxygen plays an essential role in that the carbon induced dopant activation is favoured in oxygen-rich CZ-material.

References

[1] W. Skorupa, R. Kögler, M. Voelskow, K. Schmalz, G. Morgenstern and P. Gaworzewski, Nucl. Instr. Meth. B68 (1992) 408.

[2] W. Skorupa, R. Kögler, K. Schmalz, P. Gaworzewski, G. Morgenstern and H. Syhre Nucl. Instr. Meth. B (to be published)

Iron Gettering by MeV-carbon Implantation

W. Skorupa, R. Kögler, M. Voelskow, K. Schmalz[1],
G. Morgenstern[1] and P. Gaworzewski[1],

[1]Institute for Semiconductor Physics, POB 409, O-1200 Frankfurt, Germany

The gettering efficiency for iron of a buried carbon-rich layer formed by 10 MeV-carbon implantation with doses in the range of 10^{14}-10^{16} cm^{-2} and annealing was investigated. Iron was additionally introduced into the back of the silicon wafers by implantation with an energy of 330 keV and doses of 10^{12} cm^{-2} and 10^{13} cm^{-2}. Gettering of Fe sets in at a carbon dose of 10^{14} cm^{-2} and is completed at the surface of the wafer for a carbon dose of 10^{16} cm^{-2}, both for the highest investigated iron dose of 10^{13} cm^{-2} [1].
Moreover, a through-the-wafer inspection of the iron distribution was made [2]. In Fig. 1 the depth profile of the FeB-pair concentration as revealed by DLTS for a wafer with a thickness of about 300 nm is shown for an iron dose of 10^{13} cm^{-2}. The FeB-pair formation takes place at about 150°C that means in the cooling down phase of the annealing step. Due to the high diffusion coefficient, at the temperature of 1000°C, interstitial iron atoms are homogeneously distributed throughout the wafer. Gettering by carbon leads to a strong lowering of the iron concentration near to the surface up to about three orders of magnitude. For the highest carbon dose of 10^{16} cm^{-2} the iron content is lowered in the whole wafer. This points to iron diffusion toward the carbon implanted layer during the cooling-down phase. For the case of the highest carbon dose of 10^{16} cm^{-2} iron gettering at 1000°C seems to be concerned with the formation of iron-carbon-complexes.

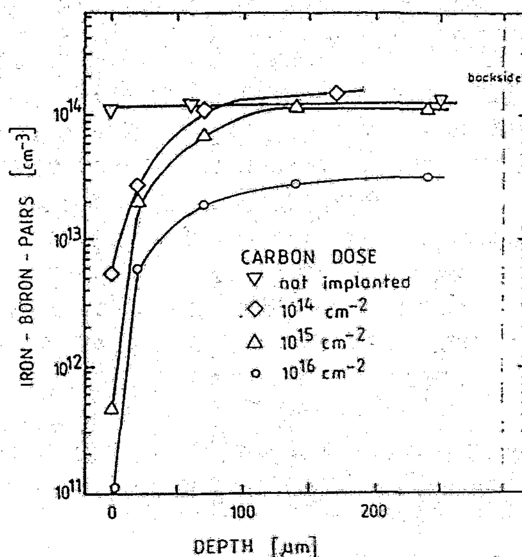

Fig. 1:
Depth profile of the deep level density of iron-boron-pairs in silicon wafers performed by a step-by-step etching procedure.
Fe-dose: 10^{13} cm^{-2},
Annealing: 1000°C, 1 h, dry N_2

References:

[1] W. Skorupa, R. Kögler, M. Voelskow, K. Schmalz, G. Morgenstern and P. Gaworzewski
Nucl. Instr. Meth. **B 68** (1992) 408

[2] W. Skorupa, R. Kögler, K. Schmalz, G. Morgenstern and H. Syhre
Proc. IX. Int. Conf. Ion Implantation Technology, Gainesville (USA), Sept. 21-24, 1992;
Nucl. Instr. Meth. B (to be published)

Formation of Buried $(Fe_{1-X}Co_X)Si_2$ Layers in (100) Si by Ion Beam Synthesis

D. Panknin, E. Wieser, W. Skorupa, G. Querner[1], H. Vöhse[2], J. Albrecht[2] and W. Henrion[3]

[1]Technical University Dresden
[2] Institute Fresenius Dresden
[3]Hahn-Meitner-Institute Berlin

$FeSi_2$ exists in two crystalline modifications: The semiconducting low temperature β-phase and the metallic high temperature α-phase. The transition from β- to α-$FeSi_2$ occurs at 967°C. The formation of a buried iron silicide layer into Si by ion beam synthesis is reported in Refs. [1-3]. The possibility of changing the properties of semiconducting β-$FeSi_2$ by addition of a third element is of interest as it may influence the band gap energy as well as the epitaxial growth of the buried silicide.
In Refs. [4-6] results are summarized concerning the ion beam synthesis of $(Fe,Co)Si_2$ in (100) Si. For these investigations Fe ($4x10^{17}$ cm^{-2} with 300 keV at 350°C) and Co ($5x10^{16}$ cm^{-2} and $1x10^{17}$ cm^{-2} with 180 keV at 350°C) were implanted. For a first series, samples were annealed at 850°C before the Co implantation resulting in a well defined layer of β-$FeSi_2$. For a second series, Co was implanted directly following the Fe implantation. After the Co implantation all samples were annealed at temperatures between 600°C and 1050°C in N_2 atmosphere.
The phase composition of the $(Fe_{1-X}Co_X)Si_2$ system is determined by X-ray diffraction [4]. In Fig. 1 the intensities of selected diffraction peaks in dependence on the post-implantation annealing temperature are shown for x=0.2. In the as-implanted state as well as after post-implantation annealing below 850°C only peaks of the β-$FeSi_2$

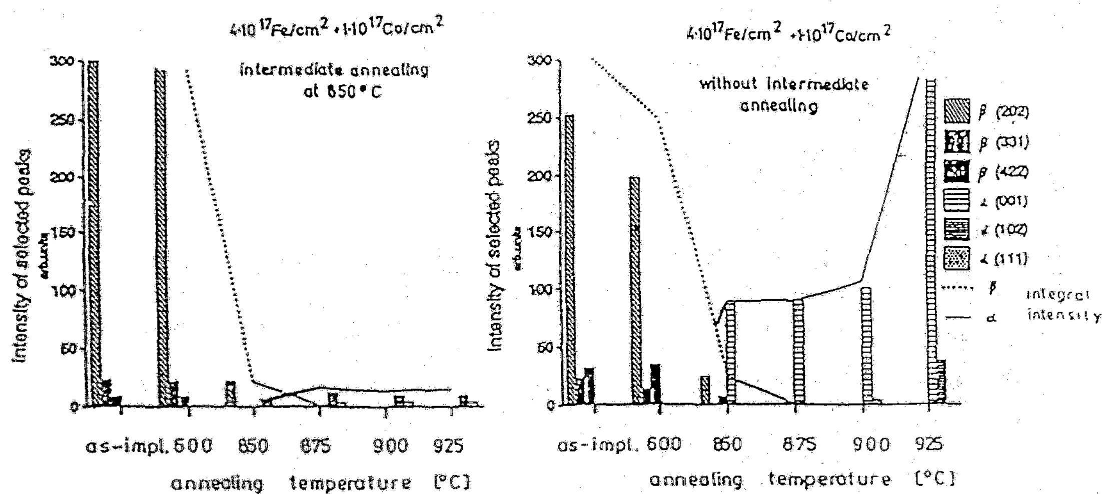

Fig. 1: Intensities of selected X-ray diffraction peaks of $(Fe_{0.8}Co_{0.2})Si_2$ in dependence on the post-implantation annealing
a: with intermediate annealing at 850°C
b: without intermediate annealing

structure are observed. This proves that the polycrystalline semiconducting structure is preserved after the Co implantation. Comparing to pure $FeSi_2$ the temperature of the β- to α-transition is shifted to lower temperatures in dependence on the Co content. The temperature shift of the phase transition is more pronounced for samples without intermediate annealing.
The depth distribution of Fe and Co, measured by Auger Electron Spectrometry, is shown in Fig. 2 after post-implantation annealing at 850°C [5,6].

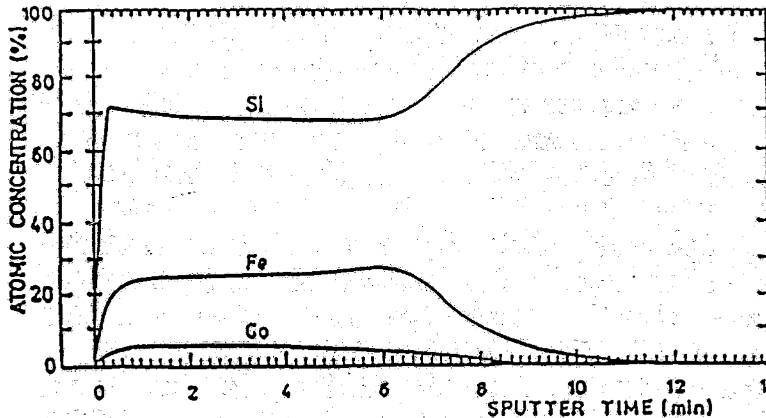

Fig. 2: Auger depth profiles of Fe and Co after annealing at 850°C ($4x10^{17}$ Fe cm^{-2} + $1x10^{17}$ Co cm^{-2}; with intermediate annealing)

For the sample with intermediate annealing a nearly homogeneous distribution of both metals is observed. In this region the stoichiometric ratio Si/(Fe+Co) is near to the stoichiometric ratio Si/Fe of pure β-$FeSi_2$ [1]. This means that the Co atoms substitute Fe in the β-$FeSi_2$ lattice. The results show that up to 20% of the Fe atoms can be substituted by Co. On the other hand, for samples without intermediate annealing a homogeneous distribution is only observed for post-implantation annealing temperatures above the phase transition [5].
The layer system after post-implantation annealing at 850°C consists of a polycrystalline Si top layer with a preferential grain orientation corresponding to the bulk Si. The $(Fe,Co)Si_2$ layer is buried below the Si top layer consisting of grains which form a block structure with preferential orientation. Below the silicide layer a defective layer is observed. The defects anneal only at temperatures above the phase transition [4,6].
Using infrared absorption the $(Fe_{1-x}Co_x)Si_2$ layer shows the existence of a band gap energy for samples with intermediate annealing [5].

References

[1] D. Panknin et al.; Sci. Eng. B12, 119 (1992)
[2] K. Radermacher et al.; Appl. Phys. Lett. 59, 2145 (1991)
[3] H. Reuther et al.; Nucl. Instr. Meth. B68, 241 (1992)
[4] D. Panknin et al.; Mat. Res. Soc. Symp. (1993), to be published
[5] E. Wieser et al.; Nucl. Instr. Meth. B (1993), to be published
[6] D. Panknin et al.; Nucl. Instr. Meth. B (1993), to be published

Investigation of Pulsed Ion Beam Induced Amorphization/ Crystallization of Silicon for Irradiation with Kr^+ Ions of 3.8 MeV

R. Kögler, V. Heera, W. Skorupa, E. Glaser[1], T. Bachmann[1] and D. Rück[2]
[1]FSU Jena, Physikalische Fakultät, Max-Wien-Platz 1, O-6900 Jena
[2]GSI Darmstadt, Postfach 11 05 52, W-6100 Darmstadt

During ion beam bombardment a preexisting amorphous/crystalline (a/c) interface in silicon is moved by ion beam stimulated effects as ion beam induced interfacial amorphization (IBIIA) and ion beam induced epitaxial crystallization (IBIEC). The occurence of IBIIA or IBIEC depends on the dose rate of the irradiation and especially on the target temperature. The IBIIA / IBIEC transition takes place at the well defined reverse temperature (T_R).
At T_R the processes of crystallization and amorphization are in balance and the a/c interface remains on its place. At a target temperature above T_R always crystallization occurs whereas at a temperature below T_R amorphization takes place. For Kr^+ ion irradiation the range of the measured T_R values is between 150°C and 300°C.
However, this rather comprehensive picture is still incomplete if a pulsed ion beam is used. Such beams could be of importance for the application of IBIEC, because RFQ´s deliver high current MeV beams.
We report experimental results using a pulsed ion beam as shown in Fig.1. The somewhat complicated pulse structure consists of triangularly shaped nanosecond pulses of a frequency of 13 MHz. A number of about 13000 of such nanosecond pulses form a one millisecond pulse. These millisecond pulses have a repetition frequency of 20 Hz. That means that each millisecond pulse is followed by an interrupt time of 49 ms.

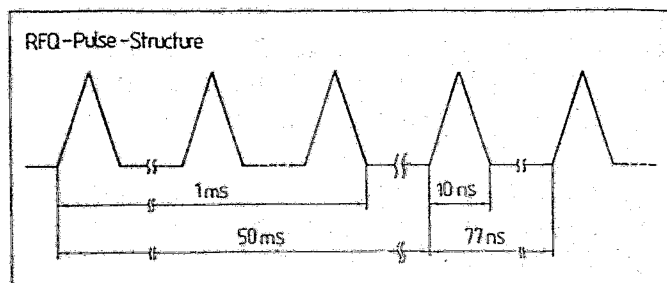

Fig. 1:
Scheme of the ion beam pulse structure

The target holder was cooled and the target temperature during irradiation never exceeded 65°C. More details of the experimental conditions are described in [1]. Data on the beam structure are summarized in Tab.1.

	beam current density	ion dose rate	reverse temperature
all time average	0.05 $\mu A/cm^2$	$3.125*10^{11}/cm^2s$	123°C
millisecond pulse	2.5 $\mu A/cm^2$	$1.560*10^{13}/cm^2s$	175°C
nanosecond pulse (max.)	37.5 $\mu A/cm^2$	$2.340*10^{14}/cm^2s$	220°C

Tab. 1:
Irradiation conditions for the 3.8 MeV Kr^+ implantation into Silicon

The results of RBS/C analysis are shown in Fig.2. The shrinking thickness of the amorphous surface layer is caused by IBIEC.
It is somewhat unexpected to find IBIEC instead of IBIIA. Comparing our ion dose rate and target temperature with those of constant beam current experiments we should be clearly in the regime of amorphization (see Tab. 1). Our target temperature is well below the reverse temperature, but we observe crystallization. The cause of this result is not yet clear. However, this corresponds with results of Linnros et al.[2] who used a pulsed ion beam, but with a frequency below 1 kHz. They found always a shift of the a/c interface displacement into the direction of crystallization. At a target temperature slightly below the reverse temperature, where normally amorphization proceeds, a change from IBIIA to IBIEC could be reached only by an increase of the pulse frequency.

Obviously the dynamic equilibrium between crystallization and amorphization establishing the a/c interface movement is significantly changed by using a pulsed ion beam. It may be that the reverse temperature for the IBIIA/IBIEC transition is considerably reduced for a pulsed ion beam of nanosecond pulses. Further investigations are needed to explain this phenomenon.

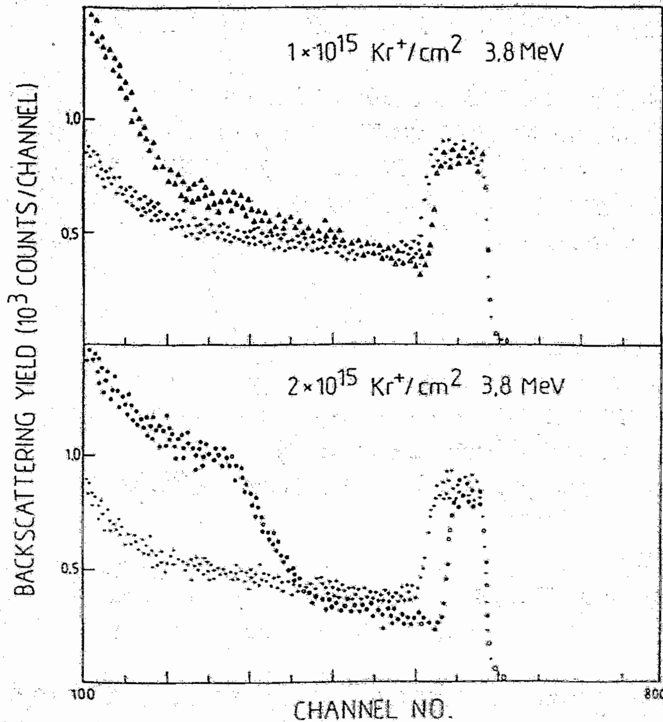

Fig. 2:
RBS/C spectra ($^4He^+$, 1.4 MeV) of the regrown amorphous surface layer for different ion doses, small dots are spectra of the amorphous layer before irradiation

References

[1] R. Kögler, V. Heera, W. Skorupa, E. Glaser, T. Bachmann and D. Rück, Nucl. Instr. and Meth. (to be published)
[2] J. Linnros, W.L. Brown and R.G. Elliman, Mat. Res. Soc. Proc. 100, 369 (1988)

Computer Program for Calculating Reflectivities of Multi-Layer-Systems

Th. Henkel and V. Heera

Since the first reports on ion beam induced epitaxial crystallization (IBIEC) and ion beam induced interfacial amorphization (IBIIA) in the mid-seventies and the beginning of the eigthies, respectively, a considerable research effort has been undertaken in the material science community to develop a comprehensive understanding of the kinetics and mechanisms of ion beam induced phase transformations in silicon thin films.

In-situ diagnostic techniques, especially the method of time resolved reflectivity (TRR) measurements, have been developed to monitor the movement of the crystalline-amorphous interface. The latter has been turned out to be a powerful and flexible tool for determining transformation kinetics in semiconductors over a wide temperature range [1]. This in-situ diagnostic technique providing a time dependent reflectivity curve during the entire experiment is able to demonstrate any interruption of IBIEC or IBIIA and is able to give an estimation of velocities of the individual interfaces.

A computer program REFLECT has been developed for calculating the theoretical reflectivity and for comparison of these values with experimental ones. This program calculates the reflectivity using the method of 2x2 linear matrix transformation [2] for systems with homogeneous, optically isotropic and planar layers and plots the reflectivity curve as a function of time or a function of thickness of the top layer. The following parameters can be varied:

- polarization of the laser beam
- wavelength of the laser
- incident angle of the laser beam
- number of layers located on the substrate (0...10)
- optical constants (real index of refraction, extinction coefficient) of all media
- thicknesses of all layers
- velocity constants of all interfaces

REFLECT has been written in the programming language C using the Borland Compiler Turbo C++ (Version 1.00). The program has got a modular structure, therefore extensions of the software are possible without any difficulties. The user will be guided by means of various menus. By the way, the dynamic management of memory resources controlled by REFLECT represents a powerful feature of this program. In other words REFLECT only occupies RAM-memory as much as needed for calculation. Furthermore one can choose a stepwidth for calculation determining the precision of the computational results and graphic plots. The calculated data can be put out to the screen or to any printer and can also be saved on a floppy or hard disc.

The following figure shows as a representative example the calculated reflectivity versus time for a buried amorphous silicon layer in a crystalline silicon substrate using a linear polarized He-Ne-laser (wavelength λ = 632.8 nm, incident angle i_0 = 0°). The top layer (c-Si) and the second layer (a-Si) have got initial thicknesses of 50 nm and 400 nm, respectively. The latter shrinks with various velocities v1 of the front interface, whereas the velocity v2 of the interface between the a-Si layer and the c-Si substrate remains constant.

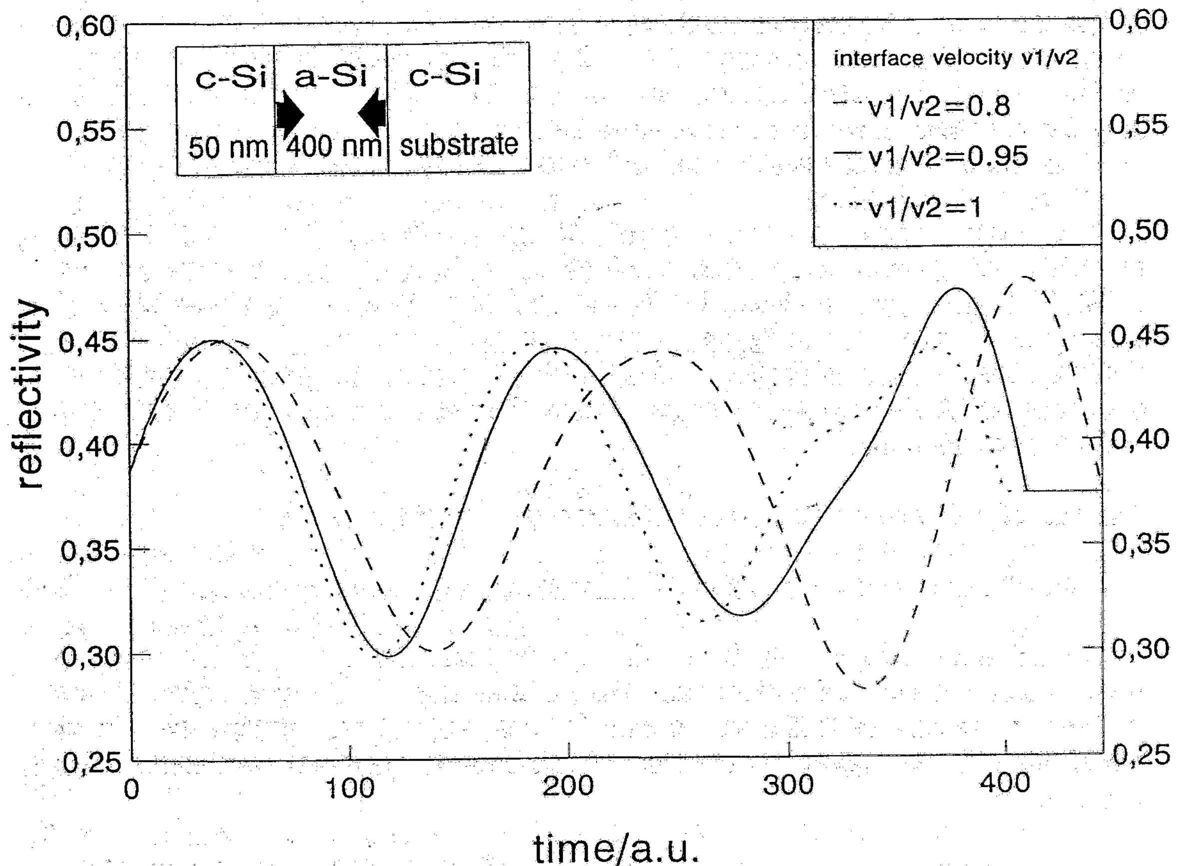

Calculated reflectivity versus time for a buried a-Si layer in c-Si substrate (initial thicknesses: d1 = 50 nm, d2 = 400 nm) using a linear polarized He-Ne-laser (λ = 632.8 nm, i_0 = 0°). Parameter: interface velocity of the front interface v1 (v2 = 1 nm/t.u.)

The figure demonstrates, that even small differences between the regrowth velocities of the front and the back interface can be resolved by means of TRR-measurements.

References

[1] G.L. Olson and J.A. Roth, Materials Science Reports 3, 11, (1988)

[2] R.M.A. Azzam, N.M. Bashara, in: Ellipsometry and polarized light, Elsevier Science Publishers BV., Amsterdam, 1987, p.332

A Formula for Estimating IBIEC/IBIIA-Rates in Silicon

V. Heera

Ion irradiation of an amorphous (a) silicon layer in contact with single crystalline (c) silicon may result in either solid phase epitaxial regrowth or planar amorphization of the a-layer in dependence on ion irradiation parameters [1-5]. The first phenomenon, called ion beam induced epitaxial crystallization (IBIEC), has been extensivly investigated [6] and phenomenological models providing the IBIEC-rate in dependence on irradiation and target parameters have been developed [7-10]. In contrast to IBIEC only few experiments concern the ion beam induced interfacial amorphization (IBIIA) [1-5]. In most cases the transition region between IBIEC and IBIIA was investigated.

Despite numerous experimental data on IBIEC and IBIEC/IBIIA-transition it is rather difficult for people working in this field to make sure predictions about the IBIEC/IBIIA rate under arbitrary irradiation conditions. However, the knowledge of the expected layer growth may be very important for planning experiments and choosing irradiation conditions. That is why the author has extracted a formula for estimating IBIEC/IBIIA-rates in silicon from the available experimental data and theoretical considerations.

The rate of ion beam induced a-layer shrinkage/growth is defined as

$$r = \Delta d \; / \; \Phi = v \; / \; j \qquad (1)$$

where Δd is the change of the layer thickness after irradiation with the ion dose Φ, v the velocity of the a/c-interface and j the ion dose rate. The rate is defined to be positive in the case of IBIEC that occurs for temperatures greater than the critical temperature T_r and negative in the case of IBIIA for temperatures smaller than T_r, respectively.

It was shown by Linnros et al. [3] that the critical temperature T_r is a function of ion dose rate j and the linear density of vacancies Z generated by one ion at the a/c-interface during irradiation. Using j in units of ions/cm^2/s and Z in units of vacancies/ion/Å (which is the common TRIM output) the critical temperature in Kelvin is given as

$$T_r = 13400 \; / \; (57.5 - \ln(j \; Z^2)) \qquad (2).$$

Applying the IBIEC-model of V. Heera [8] and assuming that the IBIEC-rate and activation energy is simply reversed when crossing the critical temperature as indicated by a few experimental results [1,2,4] the following simple expression for the growth rate r in units of nm/10^{15} cm^{-2} can be obtained:

$$r = \pm \, c \; Z^{1.25} \exp[\, \pm \, 2900 \; (1 \; / \; T_r - 1 \; / \; T \,)] \qquad (3).$$

The positive signs stand for IBIEC and the negative ones for IBIIA, respectively.

The proportionality factor c has been fitted from numerous experimental results given in the literature. It scatters between 1 and 10. In many cases $c = 5$ is a reasonable approximation and could be applied for a first estimation of the IBIEC/IBIIA-rate.

It should be noted, that according to formulas (2) and (3) the rate is given only in dependence on ion dose rate, deposited nuclear energy and temperature. No influence of doping or crystal orientation of silicon has been considered, which is known to be very important in the case of thermally induced solid phase epitaxy [11]. Fortunately, recent experimental results have shown that the dependence of doping [9] and crystal orientation [10] on the IBIEC-rate is rather weak and, therefore, may be omitted for a rough estimation.

Once the factor c has been determined for one experiment, the change of the IBIEC-rate during the variation of irradiation conditions in this experiment may be well predicted by the formulas (2) and (3). For instance, the dose rate dependence of IBIEC which follows from formulas (2) and (3) as $r \propto j^{-0.25}$ could be confirmed experimentally [12]. However, the formulas cannot be applied in a small region around the critical temperature ($T = T_r \pm 20$ K). In this transition region the growth rate has been shown [5,7] to be

$$r \propto (1/T_r - 1/T) \qquad (4)$$

In summary, simple formulas are given above that allow to decide which process, IBIEC or IBIIA, occurs under given ion irradiation conditions and to estimate the order of magnitude of the rate of a-layer shrinkage/growth.

References

[1] R. G. Elliman, J. S. Williams, W. L. Brown, A. Leiberich, D. M. Maher, and R. V. Knoell Nucl. Instr. Meth. **B19/20**, 435 (1987)

[2] A. Leiberich, D. M. Maher, R. V. Knoell, and W. L. Brown, Nucl. Instr. Meth. **B19/20**, 457 (1987)

[3] J. Linnros, R.G. Elliman, and W.L. Brown, J. Mater. Res. **3** , 1208 (1988)

[4] A. Battaglia, F. Priolo, and E. Rimini, Appl. Surf. Sci. **56-58**, 577 (1992)

[5] W.L. Brown, R.G. Elliman, R. V. Knoell, A. Leiberich, J. Linnros, D.M. Maher, and J.S.Williams, in : Microscopy of Semiconductor Materials, ed. A.G. Cullis, Institute of Physics, London, 1987, p. 61

[6] F. Priolo and E. Rimini, Materials Science Reports **5**, 319 (1990).

[7] K. A. Jackson, J. Mater. Res. **3**, 1218 (1988).

[8] V. Heera, phys. stat. sol. (a) **114**, 599 (1989); in: EPM ' 89, K. Hohmuth, E. Richter, Akademieverlag Berlin, 1990, p. 510.

[9] F. Priolo, C. Spinella and E. Rimini, Phys. Rev. **B 41**, 5235 (1990).

[10] J. S. Custer, A. Battaglia, M. Saggio, and F. Priolo, Phys. Rev. Lett. **69**, 780 (1992)

[11] G.L. Olson and J.A. Roth, Materials Science Reports 3, 1 (1988)

[12] V. Heera, R. Kögler, W. Skorupa and R. Grötzschel, to be published in Nucl. Instr. Meth. **B** and Mat. Res. Soc. Symp. Proc.

High Current FIB System for Micromechanics Application

L. Bischoff, E. Hesse, G. Hofmann, W. Probst, B. Schmidt and J. Teichert

The Focused Ion Beam (FIB) IMSA-100 was tested and used in an energy range of 25...50 keV [1,2]. The spot size measured by scanning the beam over a knife edge and analysing the rise time was 350 nm. A problem of this method is the erosion of the edge by the high current density ion beam during the measurement leading to a higher rise time. The target current can be varied in the range of 0.5 to 27 nA by changing the beam aperture. A current density near the theoretical value of about 10 A/cm^2 was determined.

For surface imaging a 4-segment coaxial semiconductor secondary electron (SE) detector was introduced which allows to process material and topography contrast images by varying the combination of the four subimage signals. The variation of the SE acceleration voltage allows to adapt the digitized detector output signals to the SE current in a wide range. Another method to image conducting surface structures is to take advantage of the ion current signal.

Although the influence of mechanical vibrations and electrical instabilities could not completely eliminated, all system parameters were achieved in the predicted range.

The use of FIB to micromechanical structuring of three dimensional material offers new fabrication possibilities combining wet chemical anisotropic etch techniques with FIB-sputtering (dry etching) in the sub-μm range. The perforation of holes in ultra-thin silicon membranes with geometrically well defined dimensions and high accuracy can be used in the fabrication of micromechanical sensor and actuator devices.

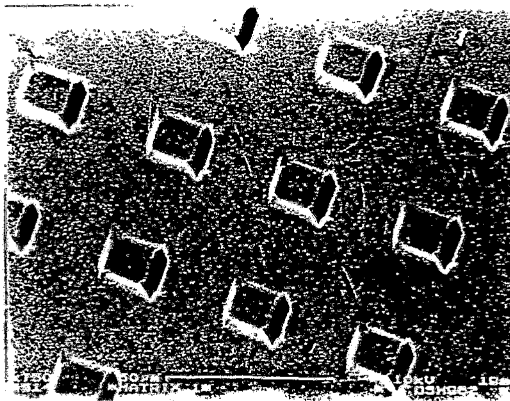

Figure 1: SEM of a groove matrix (area: 18 x 12.5 μm^2, periodicity 40 μm)

As an example FIB-sputtered test structures in a 2 μm thick anisotropically KOH/H_2O-etched <100>-oriented monocrystalline silicon membrane are presented. Fig. 1. shows a scanning electron micrograph (SEM) of a part of a square groove matrix in Si (j = 10 A/cm^2, area of a groove 18 x 12.5 μm^2, dose: 3.3 10^{18} cm^{-2}, writing time: 60 s). The dose for opening a hole amounts to 3.85 10^{18} cm^{-2}, i.e the holes are not completely opened. By variation of the dose one may find the exact point of the change from a groove to a hole, see Fig. 2. (j = 5 A/cm^2, area: 11 x 7 μm^2, dose: 3.5 10^{18} cm^{-2} (left) and 4.1 10^{18} cm^{-2}. The finest geometry opened by the FIB into the membrane was a line with a line width of 75 nm (writing time: 1s), as shown in Fig. 3.

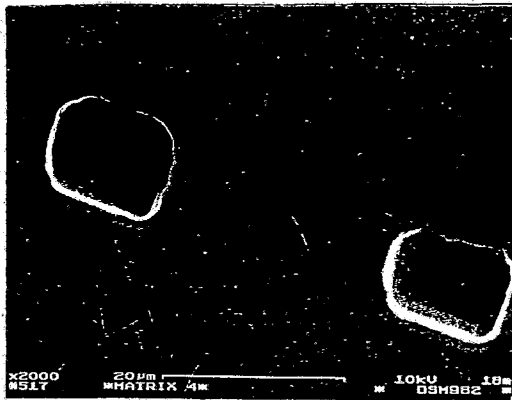

Figure 2: SEM of two square structures made at different doses, see text

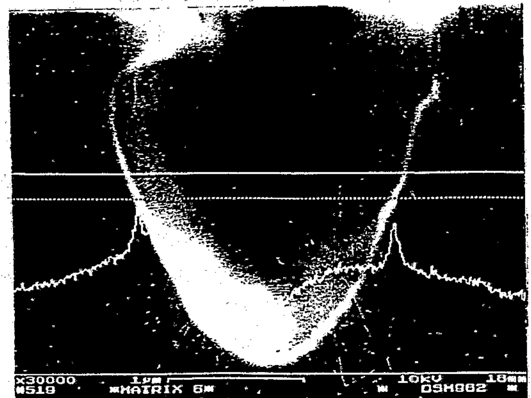

Figure 3: SEM of the finest geometry made by IMSA - FIB with a line width of 75 nm

The Rossendorf focused ion beam IMSA-100 is a useful system for basic and applied research in the field of nanometer technology. The high current density of about 10 A/cm^2 allows to process micromechanical structures from nearly 100 nm up to some ten microns in shortest time as well as opens new aspects of investigations of the beam - target interaction.

References

[1] L. Bischoff et al., Microelectr. Engineering 13, 367 (1991)
[2] L. Bischoff et al., Proc. Int. Conf. Microciruit '92
Sept. 21-24, 1992, Erlangen, Germany

Preparation of the IMSA-100 for Ion Beam Synthesis Purposes

L. Bischoff and J. Teichert

Maskless writing ion implantation and micromachining are some of the most attractive applications of focused ion beams (FIB) at present. The advantages of these micropatterning processes are the high resolution, the flexibility in dose, energy and pattern design as well as the simplification of the fabrication process. A limiting factor is the small throuput compared with other techniques because of the relative low current density of the ion beam.

The Rossendorf focused ion beam IMSA-100 was designed to achieve ion current densities >10 A/cm^2 in an ion energy range from 20 to 100 keV [1] and was successfully tested for micromechanics applications with a gallium beam up to 50 keV [2]. All components of the ion optical column (the liquid metal ion source (LIMS), two electrostatic lenses, a pre-lens octupole deflector, a novel beam blanking system [3], two octupole stigmators and a 4-segment secondary electron detector for topography and material contrast imaging) were cleaned with respect to UHV conditions. The column was reconstructed according to the experience after the first ion beam operation period of 500 hours . A high resolution double E x B mass separation system for the application of ion species other than gallium extracted from alloy LIMS's was introduced into the column. The computer control of the system was improved. A digital scan processor and a fast image storage were tested. High voltage supply units for the mass separators were inserted. A variable sytem to contact the sample in the IMSA-vacuum chamber allows the use of a target heater with temperature control or electrical measurements during beam operation. Fig. 1. shows a schematic drawing of the new IMSA equipment.

The most important aim of the further work is the investigation of writing implantation with cobalt ions from a Co/Nd alloy LMIS to form $CoSi_2$ microstructures on silicon by ion beam synthesis. The advantages using the microbeam in this technology are the short implantation time for doses of 10^{17} to 10^{18} cm^{-2} because of the high current density as well as the implantation without any mask.

The improved IMSA-100 is still able to work on all traditional fields of micro beam applications, e.g. micromachining , surface analysis, etc.

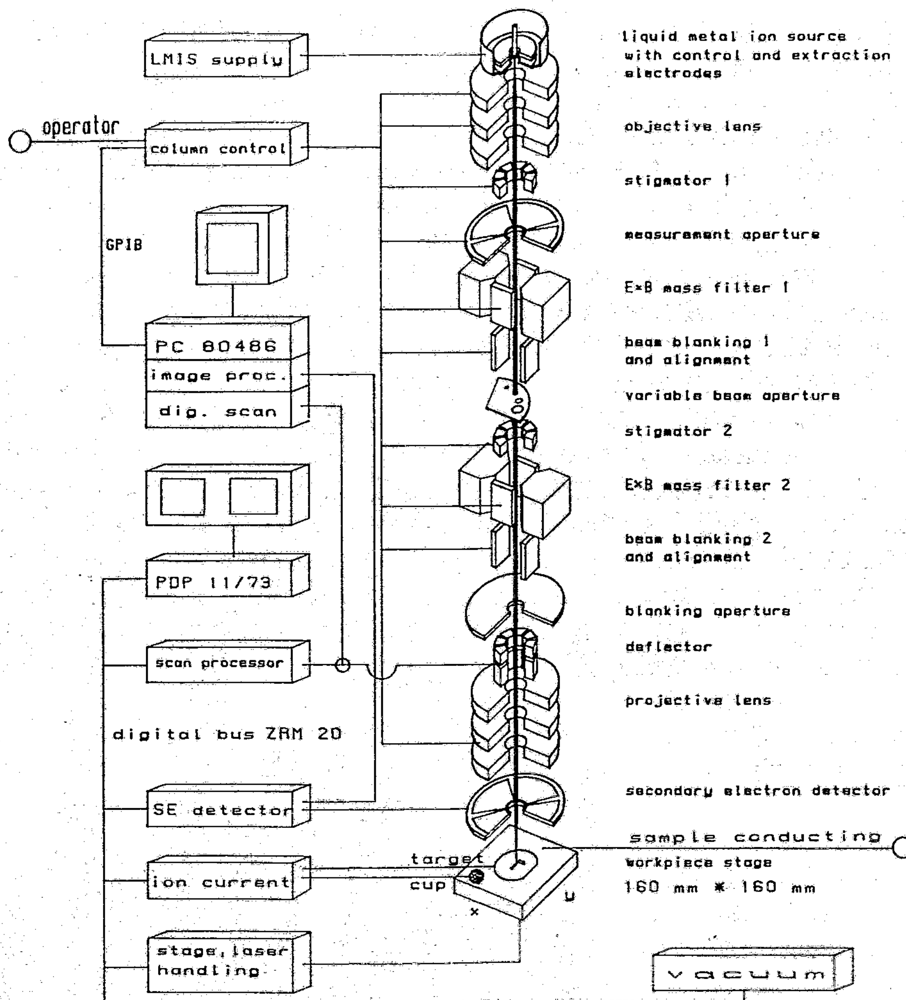

Figure 1: Schematic drawing of the IMSA-100 equipment

References

[1] L. Bischoff et al . Microel. Engineering 13, 637 (1991)
[2] L. Bischoff et al., .Microelectronic Engineering, to be published
[3] J. Teichert and D. Janssen, Optik 91 No.1, 46 (1992)

Development of a Cobalt Liquid Metal Ion Source

E. Hesse and J. Teichert

In order to implant the element Co with a focused ion beam system [1] a liquid metal ion source (LMIS) for cobalt ions has been developed.

Cobalt in elemental form can not be used in a LMIS due to its high melting point of 1495°C. Therefore, the source material must be an alloy or compound containing cobalt. The eutectic alloys of cobalt with one of the rare-earth elements show the lowest melting points [2]. Furthermore the eutectic compositions contain a high portion of cobalt in the alloy and show no dismixing of the constituents. From the rare-earth elements the neodymium has been selected. Its eutectic mixture with cobalt comprises 36 atom percent of cobalt and 64 atom percent of neodymium. The Co-Nd alloy has a melting point of 566 °C. The vapor pressure at this temperature is sufficient low and it shows a good wettability and no corrosive reaction with the emitter material. The large mass difference of cobalt and neodymium permits a simple mass separation. We use a hairpin like emitter made of 0.2 mm tungsten wire. The preparation has been done in the same way as for the well-known gallium LMIS. A meniscus of the alloy which sticks to the heating wire and the needle of the emitter represents the resevoir. The wetting has been performed in the vacuum chamber by dipping the heated emitter in the molten alloy. Figure 1 shows a photograph of the wetted emitter. The source has been tested nearly 15 hours with the parameters given in Table 1.

source material:	$Co_{36}Nd_{64}$
working temperature	ca. 600°C
heating current:	2.5 ... 2.8 A
extraction voltage:	4.5 ... 5.2 kV
emitter current:	2 ... 20 μA
current stability:	±0.5%
(current control mode)	

Table 1:
Parameters of the cobalt LMIS

Fig. 1: Photograph of the Co-Nd emitter

References

[1] L. Bischoff et al. Microelectronic Engineering 13, 367 (1991)
[2] "Binary Alloy Phase Diagrams", ed. T. B. Massalski , ASM International , 1990

Two Concentric Emission Bundles from a Lithium Liquid Metal Ion Source

E. Hesse and F.K. Naehring

From more than ten years experience with liquid metal ion sources it is believed that Taylor cones of light metals will emit ions with lower energy broadening into a beam of higher angular intensity as compared to heavy-mass metals. Lithium may be the best candidate, though its handling is somewhat difficult due to its reaction with ambient gases and other impurities. In an ion optical column of appropriate chromatic aberration the lithium ion source may deliver an ion microfocus of highest current density.

At a lithium liquid metal ion source two concentric emission bundles with sharp outlines are observed in this investigation [1]. They may indicate two different kinds of emitted ions and / or emission mechanisms. The angular intensity of the narrow bundle is the highest one reported for liquid metal ion sources.

During the emission of the lithium liquid metal ion source a red fluorescence is observed at the collector electrode. The emission of red light is associated with the atomic spectrum of lithium. The collector light was presumed to arise out of the excitation of emitter material previously deposited on the collector surface and resputtered [2],[3]. At emitter currents (including secondary electrons) equal to or higher than 4 μA a red spot with homogenous illumination and circular shape is visible. Its diameter corresponds to a divergence half angle of $8° = 140$ mrad. At the boundary of the spot the light intensity decreases steeply. Within an angular range of less than 30 mrad it becomes invisible there. With the ion current increasing, the diameter of this spot remains constant. But the intensity rises.

Additionally, a circular red fluorescent spot larger than that discribed above and concentric to it is observed at emission currents equal to or higher than 10 μA. Its visual intensity is considerably lower than that of the inner fluorescent area. Between 20 and 80 μA at the periphery of the outer fluorescent area a sharp cutoff similar to the above described narrow emission is observed. The transient zone measures less than 55 mrad. The diameter of the included area corresponds to a divergence half angle of 19° or 330 mrad. With the ion current increasing, both fluorescence spots seem to become brighter to the same extent.

Considering secondary electrons in the above described observation, the measured emitter current of 4 μA corresponds to an ion current of about 3 μA. Because of this ion current value and the half beam divergence of 140 mrad the angular intensity is estimated to be 50 μA/sr. That is about twice the value of 24 μA/sr measured at a gallium liquid metal ion source (Fig.1) [4]. This preliminary result is consistent with the experiments and calculations on the atomic mass dependence of angular intensity [5] (Fig.2). In Fig.3 the estimated beam profile for the lithium source at 3 μA total ion current is compared with that measured at gallium and bismuth sources [4]. In the calculations reported in [5], the following reasons for the increase of angular intensity at lower ion masses are taken into account: The higher velocity of lighter ions as compared to heavier ones at the same acceleration voltage results in a faster passing of

the zone of high Coulomb repulsion between the ions. Furthermore, the liquid metal protrusion at the end of the Taylor cone is shortened by the reduced space charge. Thereby the trajectories of the ions are modified.

The unexpected emission features described above may give some hints on the ion interaction in the emitting region regarding ion-ion Coulomb interaction, energy broadening and appearance of different emission mechanisms [1]. The sharp intensity cutoff at the periphery of the emission bundle is ascribed to the low energy broadening.

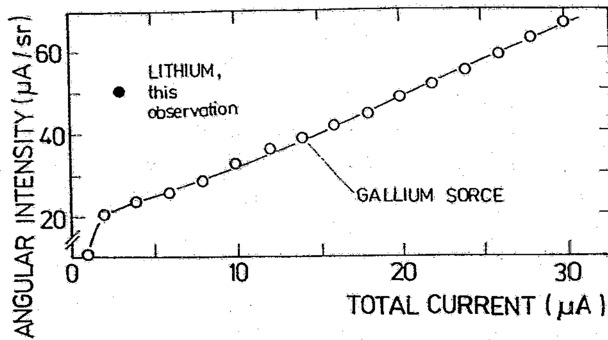

Figure 1: Plot of angular intensity vs total emission current [4] and estimated lithium angular intensity.

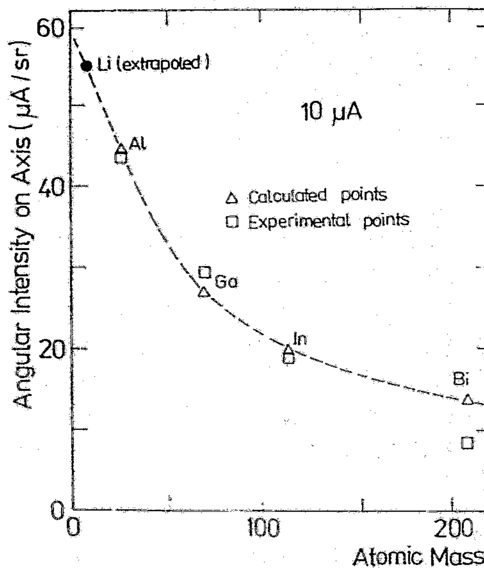

Figure 2: Angular intensities on axis for different elements at 10 μA [5] and extrapolation for lithium.

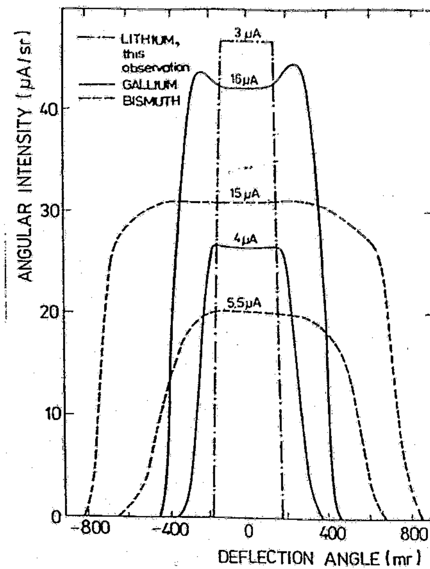

Figure 3: Comparison of the observed lithium angular intensity with experimental results from gallium and bismuth liquid metal ion sources[4]. The width of the depicted inner lithium emission bundle does not change within the used ion current range of 3 to 60 μA.

References

[1] E. Hesse and F. K. Naehring, submitted to J. Phys. D

[2] G. J. R. Mair and A. von Engel, J. Appl. Phys. 50, 5592 (1979)

[3] A. J. Dixon and A. v. Engel, Inst. Phys. Conf. Series 54 Ch.7, Inst. of Phys. Bristol 292 (1980)

[4] L.W. Swanson, G. A. Schwind, A. E. Bell and J. E. Brady, J. Vacuum Sci. Technol. 16, 1864 (1979)

[5] D. R. Kingham and L. W. Swanson, Appl. Phys. A34, 123 (1984)

Investigation of the Electrochemical Etch Stop on Silicon using KOH

B. Schmidt

The electrochemical etch stop technique is an attractive method for fabricating micromechanical structures in silicon because it has the potential for allowing one to fabricate silicon microstructures and membranes with the thickness control on the order of ±0.1 µm and with low doping concentrations [1].
The electrochemical etch stop of ⟨100⟩-silicon in KOH/H_2O-solution arises in such a way, that there is an open-circuit-potential (OCP) of about -1.4 V against a reference electrode (RE). For applied cathodic and somewhat anodic potentials against OCP silicon etches but there is a passivation potential (PP) in the range -(1.0...0.8) V above which a passivating oxid grows (anodization) and the etch rate decreases rapidly.
The optimization of the etch conditions will involve the determination of the PP for n- and p-type silicon in the 30% KOH/H_2O -solution at T = 80 °C. Furthermore , from the knowledge of the PP we can optimize the etch conditions for a reverse biased pn-junction to get ultra-thin monocrystalline silicon membranes of well defined thickness and with high accuracy.
All electrochemical measurements were carried out using a EG&G PARC Model 362 Scanning Potentiostat. The etching was performed in darkness with the etch solution in a thermostat at T = (80±1) °C. The schematic three-electrode electrochemical etch configuration is shown in Fig. 1. Double-polished 3" p- and n-type wafers of (335±15) µm thickness and (1...10) Ωcm resistivity have been used to get the I-U-scans and to determine the OCP- and PP-potentials. The etch mask we used was 1.3 µm thermally grown and patterned wet oxid. The wafers were mounted in a stainless steel holder, which protects the front side of the wafer from the solution. Furthermore, the Ag/AgCl-RE was immersed in a saturated KCl-solution and galvanically connected with the etch bath by a current key. Therefore we can exclude some interaction of the RE with the hot etch solution. During the I-U-scans the potential applied to the silicon wafer was scanned from -1.6 up to 0.0 V with scanrates of (2...5) mV/s (Fig. 2 and Fig.3).
From these measurements we have been determined the following electrochemical potentials versus RE (Table 1):

Substrate	OCP in mV	PP in mV
p-Si	-(1300±10)	-(890±5)
n-Si	-(1460±30)	-(950±10)

Table 1:

Electrochemical potentials for silicon in 30% KOH at T=80°C

These values are similar to that of [2,3] but must be always determined for the given etch conditions. The I-U-curves for n- and p-type silicon especially the currents flowing for cathodic potentials differ very much. p-Si showes the characteristic backward biased diode for negative potentials (U ⟨ OCP), whereas n-Si exhibits a large "leakage" current similar to a forward biased diode. It is important, that in all cases at cathodic potential relatively to the PP silicon will be etched and for anodic potentials grater than PP the anodization and therefore the etch stop will be take place.

From this etch behaviour we conclude the applied etch potential versus RE used in experiments for the electrochemical pn-junction etch stop during fabrication of ultra thin monocrystalline Si-membranes.

References

[1] B. Kloek, S.D. Collins, N. deRooij, and R.L. Smith, IEEE Trans. Electron Devices, **ED-36**, 663 (1989)

[2] H. Seidel, Proc. 3rd Toyota Conference: Integrated Micro Motion Systems, Aichi, Japan, Oct. 1989. F. Harashima (Ed.), Elsevier Science Publishers B.V., 1990, p. 51

[3] S.S. Wang, V.M. McNeil, K.-Y. Ng, and M.A. Schmidt, General Motors Research Publication, GMR-6982, (1990)

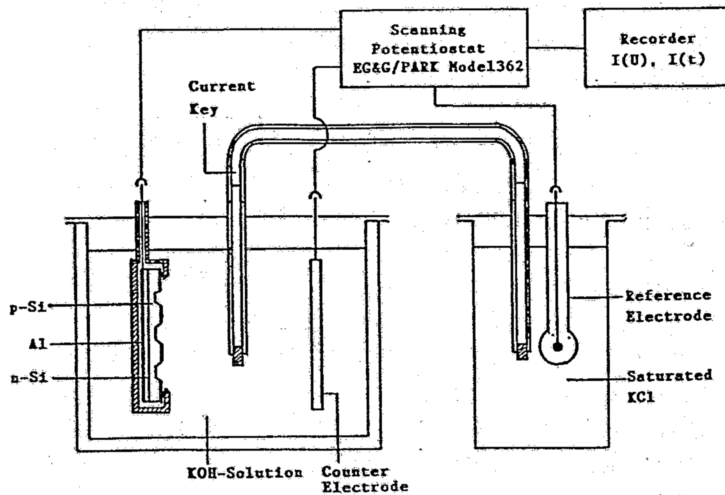

Fig. 1:
Schematic three electrode electrochemical etch configuration

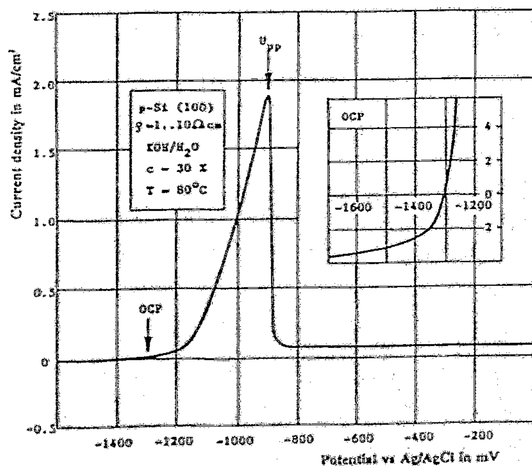

Fig 2: Voltammogram of p-type silicon

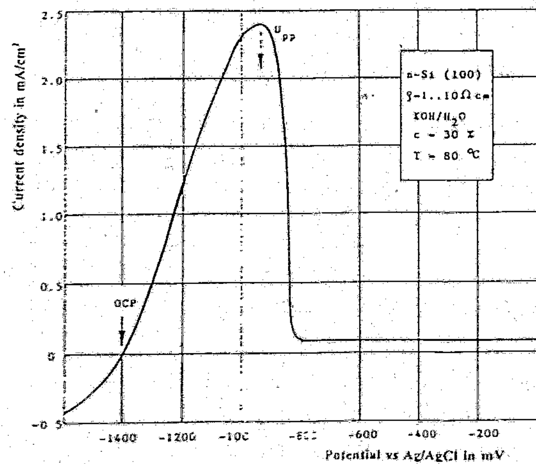

Fig. 3: Voltammogram of n-type silicon

Electrochemical Etch Stop Behaviour on Ion Implanted Silicon pn-Junctions

B. Schmidt

In silicon micromachining the electrochemical etch stop have been often used on pn-junctions, which are usually formed on epitaxial n-type layers with thicknesses $\rangle$ 1 µm on p-type ⟨100⟩-substrates. To obtain ultra thin membranes of precisely controlled thickness smaller than 1 µm n-type layers can be formed by ion implantation of phosphorous or arsenic ions and subsequent annealing and drive-in diffusion .
The aim of the work is to investigate the electrochemical etch stop behaviour in dependence on the implantation energy, the implanted dose and on the annealing and drive-in diffusion conditions.
The experiments have been done with the three-electrode potentiostatic configuration as described in [1]. To form thin n-type layers P^+- and As^+- ions in the energy range E = (30...600) keV and with doses in the range of D = $(1\cdot10^{12}...1\cdot10^{15})$ cm^{-2} have been implanted and annealed (diffused in) at T = (800...1100) °C for 30 min up to 12 h to get a wide range of the pn-junction depth (from 0.1 up to 10 µm). The investigations were carried out on 3" ⟨100⟩-oriented p-type wafers with resistivities of ρ = (1...10) Ωcm. Thermally grown and patterned oxide was used as an etching mask. All samples have been etched in 30% KOH/H_2O-solution at T = 80 °C. The etch rate at these conditions in ⟨100⟩-direction was $R_{\langle100\rangle}$ = (69±2) µm/h, which means an etch time of about 5 h. After a 3.5 h pre-etch the potential of U_{etch} = - (902±2) mV relatively to the Ag/AgCl-reference-electrode was applied to the implanted n-type layer and the current versus time characteristics have been measured by the I(t)-recorder.

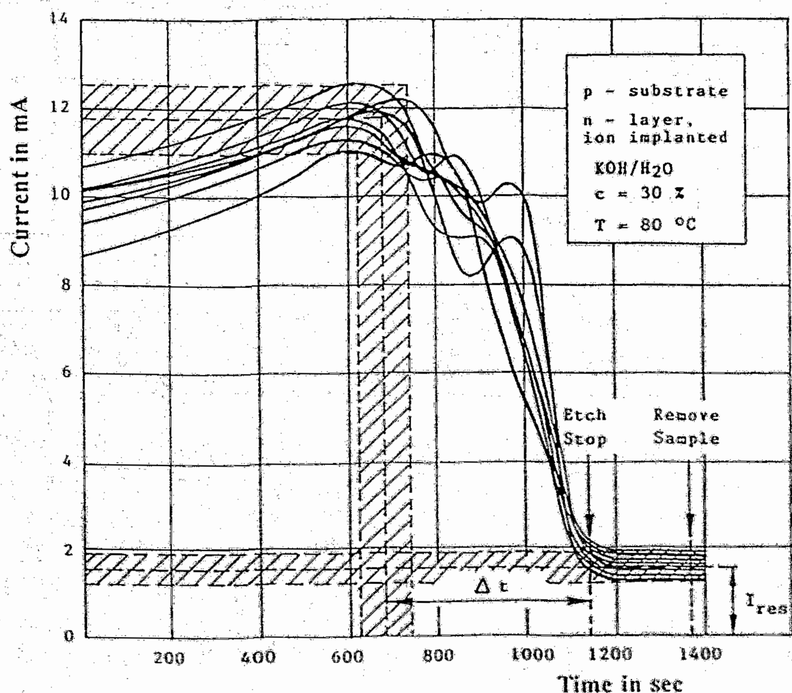

Fig. 1: I(t)-characteristics during the electrochemical etch stop on ion implanted pn- junctions

Fig. 1 gives typical I(t)-characteristics of ten etch samples during the last 20 minutes before the complete etch stop. The I(t)-curves show that the current increases up to (11.5±0.8) mA, corresponding to a current density of (1.8±0.1) mA/cm^2 and after Δt = 7.5 min the complete etch stop will be reached. The remaining current I_{rest} = (1.5±0.3) mA corresponds to the anodization (oxydation) current of the samples. The experiments show that after the complete etch stop the sample may be stay in the etch bath more than 5 min without destruction even for the most shallow pn-junctions formed by 30 keV phosphorous implantation and 30 min annealing at T = 800 °C.
Fig. 2 shows the observed difference of the I(t)-etch characteristics between ultra shallow junctions (implantation energies ≤ 60 keV and short annealing t ≤ 90 min at 1100 °C) and deep diffused junctions (t_{diff} ≥ 5 h at 1100 °C). For shallow junctions the initial current is smaller and and a sharper peak during the etch stop process can be observed. The two maxima in the curve are not yet understood.
The remained membrane thicknesses after etching will be measured using the α - particle absorption (energy loss) technique and additionally for membranes below 5 µm using the Rutherford backscattering technique. From these measurements we can investigate the difference between the thickness, where the etch stop takes place and the metallurgical pn-junction. There are some remarks in the literature [2] that the electrochemical etch stop appears somewhat before reaching the pn-junction, but up to now there are no detailed and quantitative investigations of this effect.

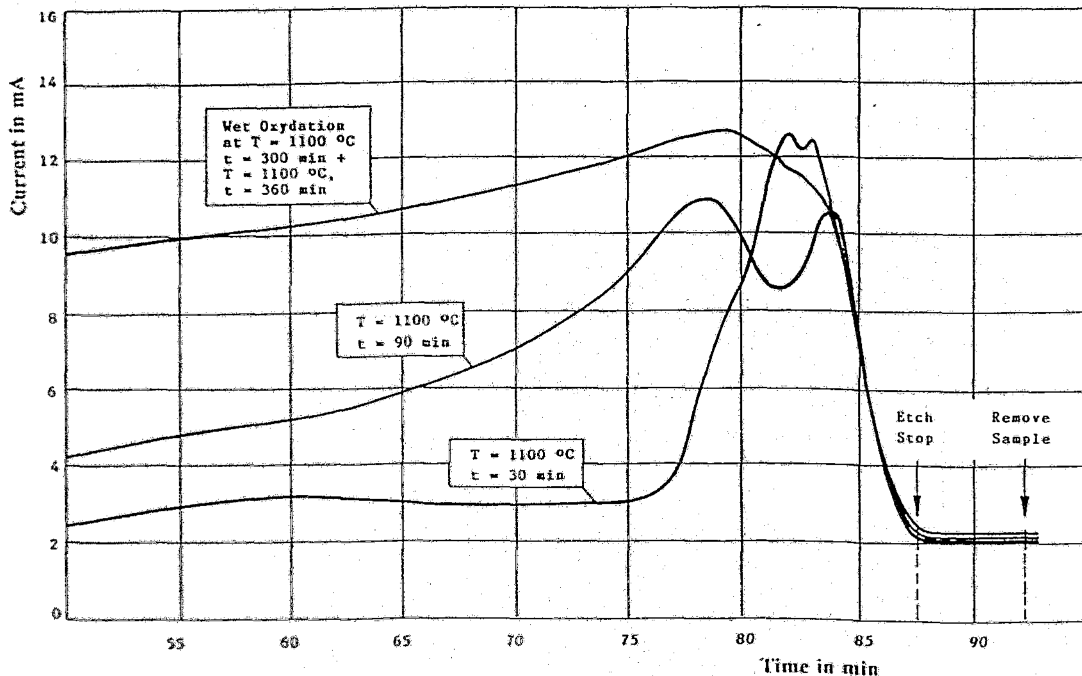

Fig. 2: Typical etch stop characteristics of shallow and deep diffused pn-junctions

References

[1] B. Schmidt, in this report
[2] M.K. Andrews, and G.C. Turner, Sensors and Actuators A, 29, 49 (1991)

A Measurement System for Studying Electrochemical Field Effect Ion Sensitivity

M. T. Pham, W. Taubert, and M. Bürger

CV measurements (capacitance voltage) on EIS structures (electrolyte insulator semiconductor) are the basic means for determining the electrical and electrochemical properties of ion sensing membranes used in ISFET microsensors. Commercially available instruments are highly specialized and are meant either for the characterization of solid-state materials and devices or for purely electrochemical research works. An »in-between« way that covers both aspects is lacking so far.

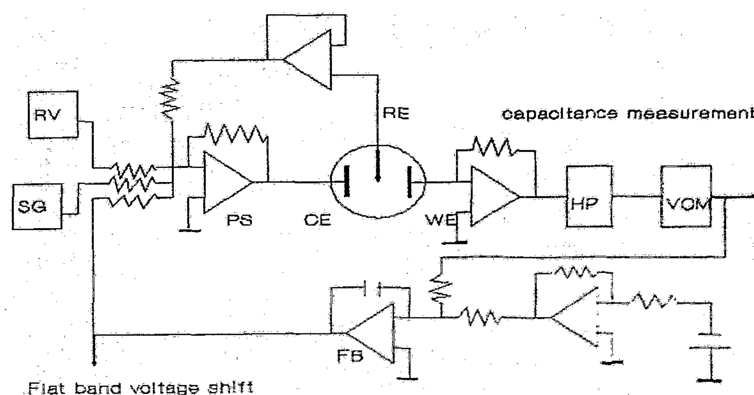

Fig.1: Circuit for dynamic capacitance measurement on EIS structures; CE: counter electrode, RE: reference electrode, WE: working electrode, RV ramp voltage, SG: sine generator, PS: potentiostat, HP: high pass filter, VCM: vector components meter, FB: feedback

The system we are using in Rossendorf for studying electrochemical field effect ion sensitivity represents a synthesis of these two techniques. The measuring scheme is based on the potential-controlled configuration designed for three-electrode cell arrangement, Fig. 1, with the working electrode (WE) being the sample under investigation. The key component of the system is the dynamic capacitance measurement using the phase-sensitive detection principle. A small amplitude sinusoidal potential modulation is added to a ramp voltage via the adder-type potentiostat. The capacitive current phase shifted 90° relative

to the applied ac potential is measured by the vector components meter. For determining the flat-band voltage shift the system operates in the constant capacitance mode via an analog feedback unit. Fig. 2 shows the block diagram of the measuring system. All the analog components are interfaced to a PC. The software used is LABWINDOW. The system is capable to perform 5 basic measuring techniques which are available in one experiment series without need of rearranging the sample under test:

1) Quasi-static CV measurement
2) Small signal CV measurement
3) Measurement of the flat-band voltage shift
4) Determination of the polarization
5) Differential measurement of two capacitances.

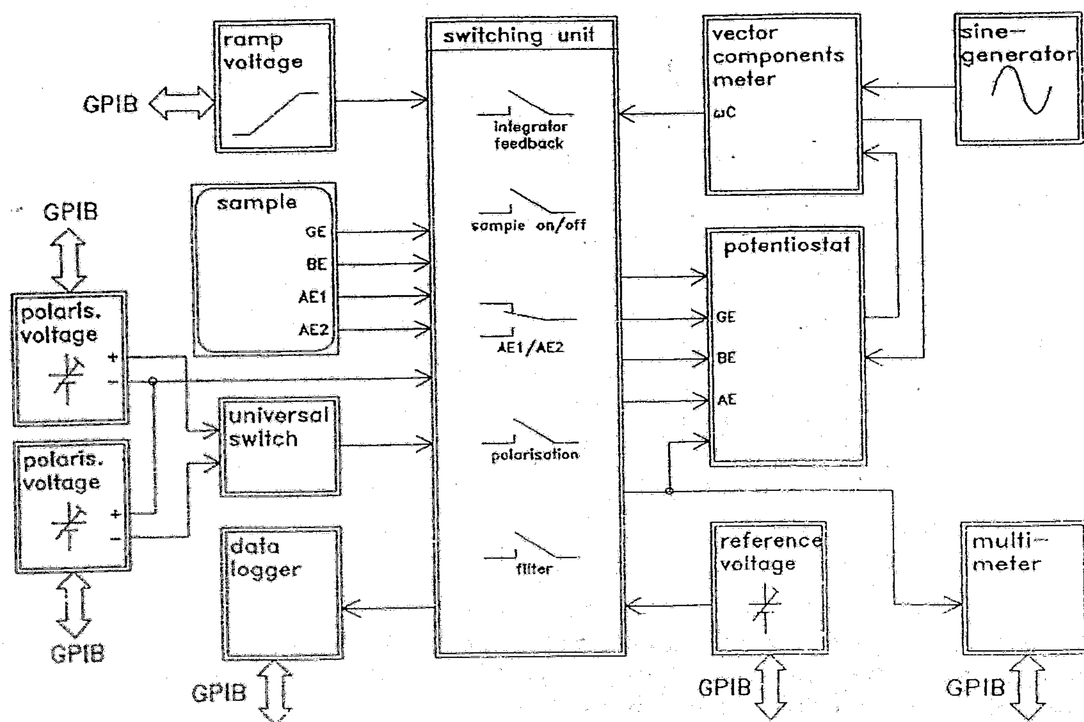

Fig. 2: Schematic block diagram of the measurement system

An Approach to the Cross Sensitivity of the Ion Sensing Membranes

M. T. Pham and S. Howitz

The common practice to take account for the cross sensitivity is to »fit«, usually denoted as conditioning, the sample to the sensor characteristics. This fails in continuous measurements. We will report here on the simultaneous measurement of the analyte and its interfering components using ion implanted membranes of mixed ion sensitivity. Differential measurements with ISFETs of different sensitivities are used as the basic concept. For determining two parameters - pNa and pH - a three-membrane system is considered as a model:

Si_3N_4 : sensitive to pH
NAS1 : sensitive to pH and pNa
NAS2 : sensitive to pH and pNa
(NAS: sodium aluminosilicate)

With this system two independent differential output sig-nals (mV) are available relating to changes in pNa and pH as follows:

$$\Delta_1 = (\partial f/\partial pNa)\, \Delta pNa + (\partial f/\partial pH)\, \Delta pH \qquad \text{for } NAS_1\text{-}Si_3N_4$$

$$\Delta_2 = (\partial g/\partial pNa)\, \Delta pNa + (\partial g/\partial pH)\, \Delta pH \qquad \text{for } NAS_2\text{-}Si_3N_4$$

The four partial differential coefficients are the ion sen-
sitivities S_{11}, S_{12}, S_{21}, S_{22} of the corresponding differential ISFET pairs which were determined experimentally in solutions with constant pNa (or pH). The indexes 1 and 2 refer to the two NAS membranes respectively. The changes in pNa and pH are deduced from Δ_1 and Δ_2 which represent the quantities to be measured in the actual si-tuation:

$$\Delta pH = (S_{11}\, \Delta_2 - S_{21}\, \Delta_1)/(S_{11}\, S_{22} - S_{12}\, S_{21})$$

$$\Delta pNa = (S_{22}\, \Delta_1 - S_{12}\, \Delta_2)/(S_{11}\, S_{22} - S_{12}\, S_{21})$$

The actual value for pH (or pNa) follows corresponding to the calibration as usually, e.g. from $pNa = pNa_0 + \Delta pNa$. With the used membrane system which was characterized by $S_{11} = 50$, $S_{12} = 52$, $S_{21} = 24$, and $S_{22} = 17$ we could follow changes of pNa and pH in the range of 1 - 3 and 2 - 10, respectively. Together with a Pt electrode ISFETs with mentioned membranes were used in pairs in a differential measurement circuit for acquiring the analytical signals. Fig. 1 shows the typical response of our sensing device. The analytical results evaluated are given in Fig. 2.

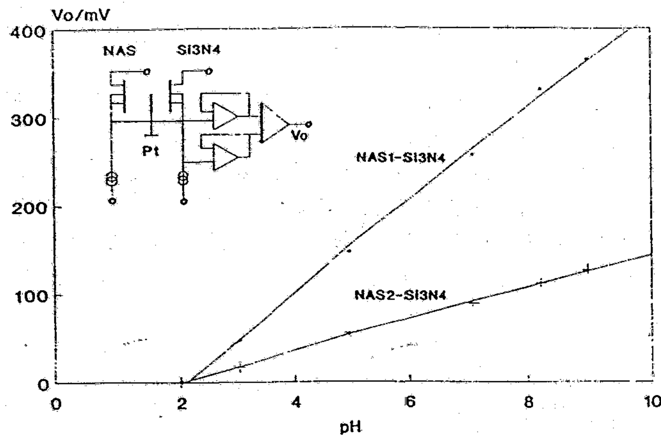

Fig. 1: Example of the sensing function of the integrated sensor with three-membrane system: Si_3N_4-NAS1-NAS2. Measured output signal of the differential pair Si_3N_4-/NAS1-ISFET in dependence on the pH in electrolyte with 0.1 mol/l NaCl. NAS membranes were prepared by implanting Na^+ (42 keV) and Al^+ (60 keV) into the SiO_2 layer of the ISFET gate to a total dose of 2 x 10^{16} ions/cm². The thermal treatment was conducted at 700 °C in N_2 for 20 min. An etch step in buffered HF was followed to reveal the buried membrane.

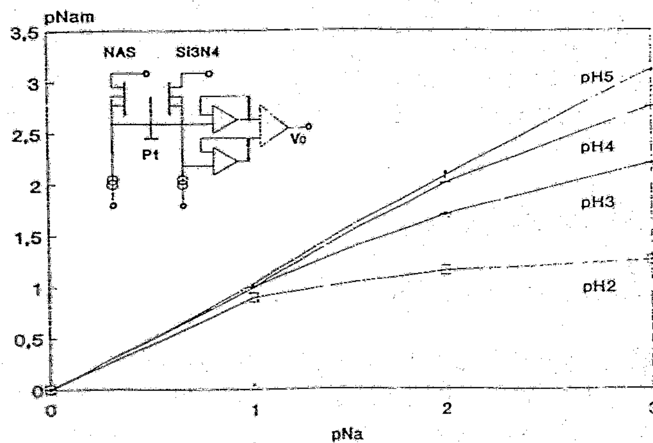

Fig. 2: Determination of pNa (denoted by m) from S and Δ showing the dependence of the detection limit on pH

ISFETs with Controlled Gate Membrane Opening

M. T. Pham and S. Howitz

ISFETs with an acceptable lifetime are needed in continous measurements in closed flow systems which do not permit any interruption during the system operation. Currently available ISFET microsensors suffer from the fact that they are either short-lived or the lifetime is indefinable.

We present here the concept »redundancy sensor« based on ISFETs with buried gate membrane. The new structure enables the ISFET to appear in two defined states: active and passive. In the passive state the buried membrane has no direct contact to the electrolyte, thus it is protected from any electrolyte attack being one serious cause for deteriorating the lifetime. In the active state the membrane is exposed to the electrolyte. Using such ISFETs in an array a desired lifetime of the system may be achieved by controlled opening of the gate membrane.

The common structure of an ISFET is the one with open gate window required for exposing the membrane to the test solution. We design here a new structure having buried gate membrane and study the technique for the insitu opening of the gate window in the measuring solution. The buried structure used in this experiment is a SiO_2 membrane covered by a metal layer having parameters similar to those of the ISFET gate: metal/CVD-SiO_2/Si_3N_4/SiO_2/p-Si (with 100 nm CVD-SiO_2, 100 nm Si_3N_4, 70 nm SiO_2). Exposed to the electrolyte solution the membrane has no contact to the medium and remains thus in the passive state as long as the metal coating is still present. Only after removing the metal coating the membrane can develop its ion sensing function by directly contacting the solution. The anodic dissolution of the coating metal was studied for opening the gate membrane using a cylinder cathode of Pt. The anode area exposed to the solution was defined by an epoxy encapsulation. The electrolytes were solutions of defined pH (2, 7 and 10) containing 0.1 mol/l NaCl. The dissolution process was followed microscopically. For Al (thickness of 100, 600 and 1000 nm) as coating metal the following results were obtained:

a) A favorable working regime was found to be 1.2 - 1.4 V for the anode-cathode voltage with a current density of 5 - 8 A/dm^2. b) A more clean removal of Al was achieved with solutions at pH 2 and 10 compared to that at pH 7. c) The dissolution is accompanied by an intensive gas development which favors the dissolution by intensifying the mass transport in the solution. d) The dissolution process was seen to be laterally inhomogenenous resulting in a proper removal in the edge regions adjacent to the epoxy encapsulation while leaving behind isolated islands unetched in the centre. Although a quantitative removal of Al is thus not achievable in the present configuration there are no detrimental consequences to be expected with respect to the ion sensing function because the potentiometric measurement does not depend on the surface geometry. Fig.1 gives an

example of a buried oxide membrane after the window opening.

140 μm

Fig. 1: Microscopic picture of a buried SiO2 membrane after removing the coating layer Al, 1000 nm indicating the encapsulation boundary (black vertical line, left), the unetched remainder of Al (isolated islands visible as bright spots scattering from the middle to the right edge) and the membrane region (remaining dark background)

Ion Beam Modified Insulator Layers as ISFET Membranes for Heavy Metal Ion Detection

J. Hüller, W. Hoffmann*, and M. T. Pham
*KfK Karlsruhe

Our work of the ion beam modification of membranes for ISFET has been extended to modification of heavy metal ion sensitive membranes last year.
Basic material and orientation for the kind of modification is a group of new solid-state inorganic materials: chalcogenide glasses [1]. They have been successfully used as ion sensitive membranes for determination of Ag^+, Cu^{2+}, Pb^{2+}, Cd^{2+}, Hg^{2+}, Fe^{3+} and Tl^+ concentrations in liquid media [2], [3].
We have realized three different types of preparations of the $Si/SiO_2/Si_3N_4/SiO_2$ layer structure.
In the first case the upper CVD-SiO_2-layer was etched away and replaced by a 300nm thick As_2Se_3- or As_2S_3 layer, respectively, deposited by r.f. sputtering done at the St.Petersburg University Chemical Sensors Laboratory.
These layers were undoped or homogeneously doped with 10 at% Cu or Ag, respectively.
In the second case the undoped As_2Se_3 was ion implanted with Cu in the dose range from $1x10^{15}$ cm^{-2} to $1x10^{16}$ cm^{-2}.
In the third case - in sequence the first - the upper SiO_2 layer was implanted with different doses of Cu and/or Se at 30 keV energy in the dose region from 10^{14} to $4x10^{16}$ cm^{-2}.

These experiments were destinated to clear up the principal phenomena concerning the measurability of such electrolyte insulator semiconductor (EIS) layers.
We have investigated: shape of the quasistatic and small signal C(U)-curve; position of the flatband voltage U_{Fb} within the measuring range of the ATIR capacitance measuring device of +/-8V; wettability of the surface; chemical etching behaviour; influence of the ionic strength of the measuring liquid; influence of the type of the reference electrode (Pt or calomel). Fig. 1 shows the Cu-sensitivity curve of a sputtered As_2Se_3-layer.

This type of graph is typically for CONCAP membrane sensitivity measurements at constant capacity near U_{Fb}. Besides of the Cu-sensitivity effects as drift, response, hysteresis and reproducibility may be studied with this method. The sputtered chalcogenide glass layers have a poor adhesion and homogeneity. This may be the reason for a remarkable pH-cross-sensitivity, caused by the underlaying Si_3N_4-layer.
The aim of our future work will be the synthesis of doped buried As_2Se_3 layers by direct implantation of As, Se and Cu in SiO_2. In correlation to electrochemical properties as sensitivity and selectivity it is necessary to optimize the implantation and annealing conditions.

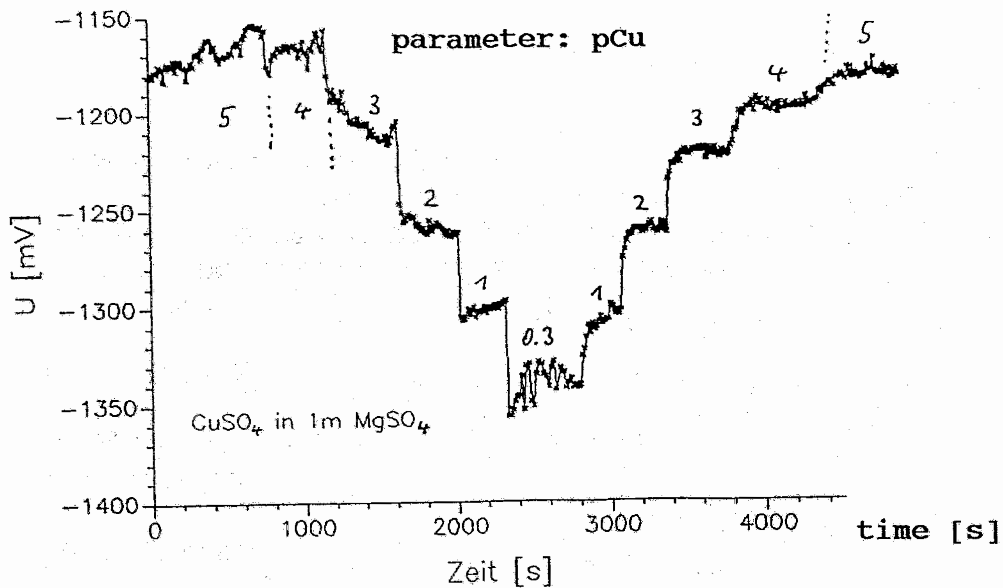

Fig. 1: Cu-sensitivity of a sputtered As_2Se_3 layer, homogeneously doped with 10% Cu

References

[1] Yu. G. Vlasov, E. A. Bychkov and A. M. Medvedev, Analytica Chimica Acta **185**, 137 (1986)
[2] Yu. G. Vlasov, Fresenius Z. Anal. Chem. **335**, 92 (1989)
[3] Yu. A. Tarantov, Yu. G. Vlasov, A. Mesentsev and Y.L.Averyanov
Sensors and Actuators, **B1**, 390 (1990)

Differential Measurements with ISFETs in Microfluid Systems

M. T. Pham and S. Howitz

The microfluid system represents the »backbone« of the Fluidic ISFET Microsystem (FIM) for chemical analysis which we are currently developing in a project financially supported by the Sächsische Staatsministerium für Wirtschaft und Arbeit [1]. It comprises an array of microsensors linked up to a system of microcapillaries and both components are an integrated unit assembled on a Si wafer. The measurements are conducted for a) gaining a first insight into the constructive details for technology optimization and designing works, b) learning to control fluid movements towards destined sensor elements embedded in the microcapillaries, c) studying the signal development and acquisition under dynamic measurement conditions.

Fig. 1 gives the schematic cross section of the microfluid system. Using the KOH-Si

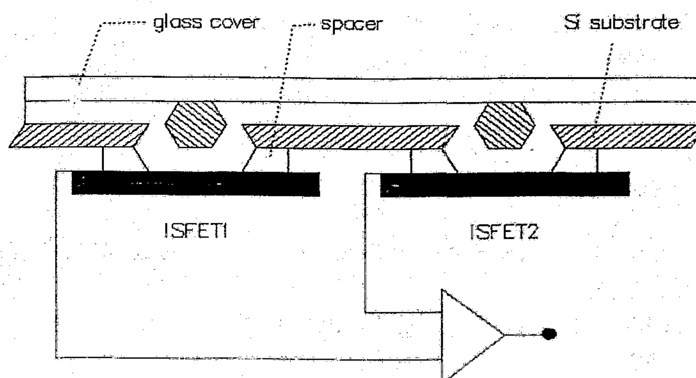

Fig. 1: Cross sectional view of the microfluid system prepared by KOH-Si etching, electrochemical drilling, glass-silicon anodic bonding and epoxy gluing

etching a meander microtrench of a total length of 2.4 m and a cross section of 200 x 500 μm^2 was etched into a Si wafer and covered by a glass sheet by anodic bonding to form the microcapillaries. The latter are provided with a series of via openings for sensor installation while several drill holes for fluid inlet and outlet are available on the glass cover side. Microsensors used are ISFETs with Si_3N_4 membrane. External pumps and valves were used in this experiment. The differential signal between two ISFETs was measured in response to perfusing the fluid channel with two pH solutions alternately. The recrod shown in Fig.2 is typical for the serial ISFET arrangement demonstrating

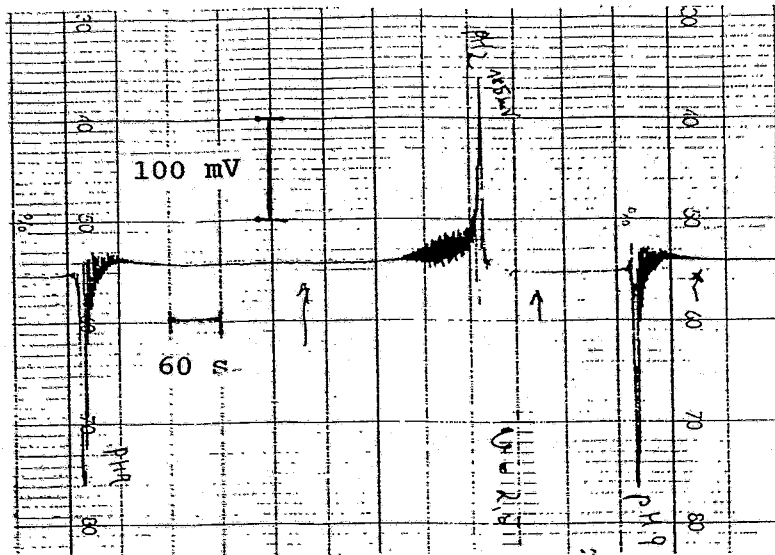

Fig. 2: Differential signal of two pH ISFETs serially arranged in the fluid channel in response to pH changes, arrows indicating the moment of solution inlet, the recording was obtained for a constant flow rate at room temperature, solutions used were pH buffers at 2 and 9 containing 0.1 mol/l NaCl

the usefulness of the system. A number of problems have to be studied in more detail, and in particular we might note:

- dependence of the response time on the direction of concentration changing
- hydrodynamic aspects in correlation with the capillary construction for controlling the radial and axial fluid tranfer rate
- contamination of the medium due to the wall adhesion resulted from increasing surface to volume ratio by scaling down the fluid channel
- fluid mixing and the system sensitivity determining the detecting resolution
- response time and fitting sensors into the fluid channel

References

[1] S. Howitz and M. T. Pham, Fluidic ISFET Microsystem, this Report.

Cooperative Project "Fluidic-ISFET-Microsystem"

S. Howitz and M. T. Pham

If using systems in static measurement, there are generally still a number of serious problems arising from ISFET inherent characteristics,and in particular we might note: signal drift, cross sensitivity, restrictive lifetime and micro reference electrode. The concept of creating a dynamic measurement system which enables chemical analysis to be done reliably by using ISFETs with currently available properties is the new motivation for research and development of ISFET based micro sensors. The FLUIDIC-ISFET-MICROSYSTEM (FIM)[1] represents one alternative way to employ ISFETs in a dynamic measurement mode useful for the multiion analysis.

The new approach followed by the ISFET research team in Rossendorf is to link up present-day results from ISFETs with present-day results on the field of micro system technique for example micro mechanics, micro elctronic measurements, micro packagings and sensor research. The dynamic measurement system will make possible the defined sampling of the analyte in the μl-nl range, the real- time calibration, the differential measurement with ISFETs of identical properties, and the intelligent data evaluation. The crux of this idea is the utilization of ISFETs of the current technical level for the exact multiion analysis. The applicative flexibility of the FIM will be reached by a fully modular and hybrid micro packaging. A system of micro packaging and micro interconnection technologies will permit the intelligent combination of sensors, actuators, and logic elements. The aim of that cooperative project currently in progress is the simultaneous detection of pH, pNa, pK, and pNO_3. Participants of the project started in Nov. 92 are Centre-Microelectronic-Dresden, Fraunhofer Institute of Microelectronic Circuits and Systems Dresden, Institute Fresenius Dresden, and Research Centre Rossendorf. In Fig. 1 are shown all elements of the FIM-microsystem schematically.

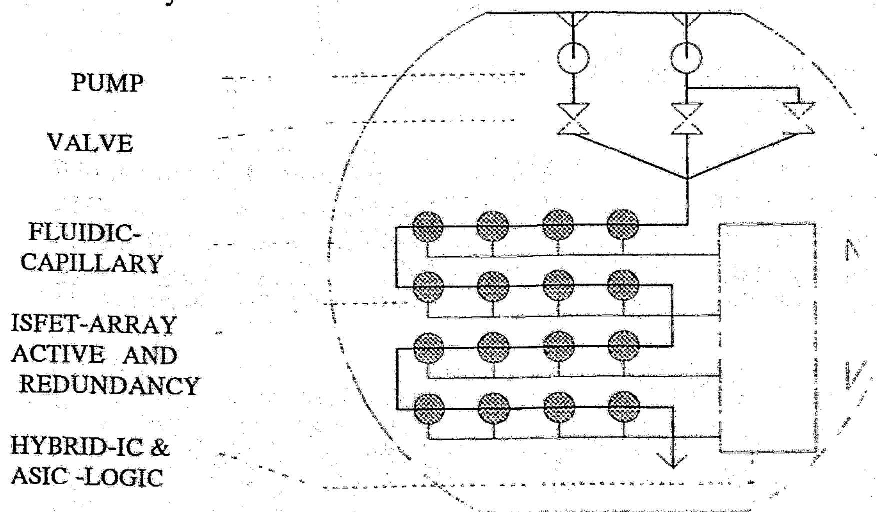

Fig. 1: Schematic view of FIM fully modular mounted upon the anodic bonded silicium-glass-substrate

The innovative scientific intentions of project FIM:

I.Back-Side-Membrane ISFET; examination of the following alternative SOI-technologies, a) Separation by Implanted Oxygen SIMOX; b) Separation by Implanted Nitrogen and Oxygen SIMNOX; c) p-n junction etch-stop and LPCVD-Si_3N_4 of the sensitive membrane area

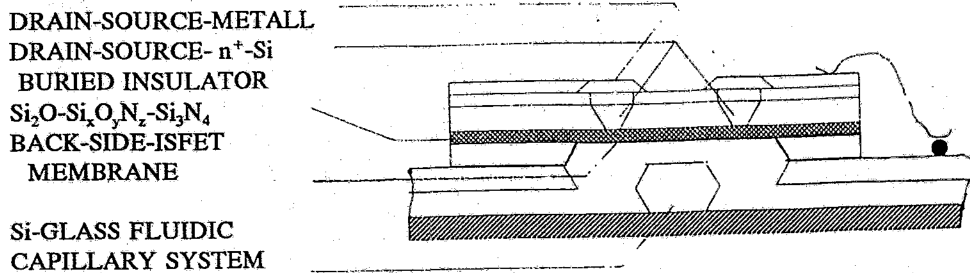

Fig.2: Cross section of a Back-Side-Membrane ISFET in SIMNOX using the N^+-O^+-implantation in silicon

II. Redundancy-ISFET[2]; based on the idea to passivate a conventional solid-state membrane of ISFET using Cr-, Cr-Ni- or Al- thin films which can be removed away, if required, by an electrochemical dissolution process (Fig.3).

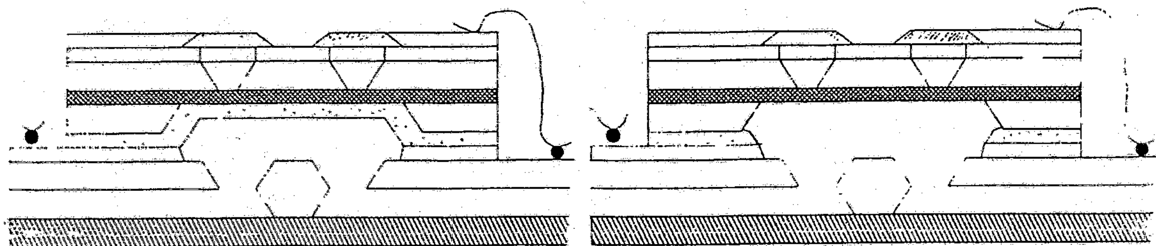

a) b)

Fig.3: Back-Side-Redundancy ISFET; a) before and b) after the electrically stimulated activation

III.The micromachined fluidic system is made by Silicon-glass technology and comprises piezoelectric actuated planar valves (two-way valves from Joswig are used [3]) and forced flow ISFET sensors embedded in a fluidic capillary system as integrated components. The assembly will be qualified by the help of FEM modelling and simulation calculations.

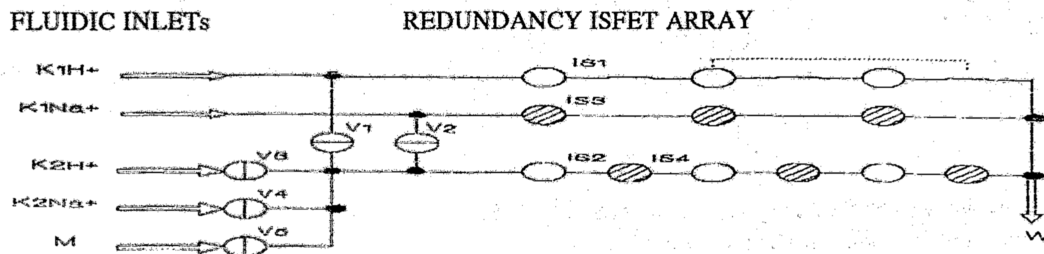

Fig. 4: Schematic view of FIM for measuring two types of ions in an fluidic capillary system(V1-V5 Valves, IS1-IS4 ISFETs)

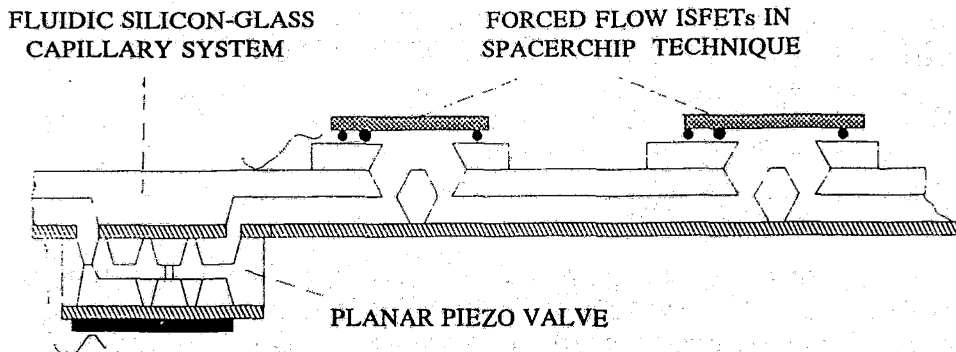

Fig.5: Cross section through the fluidic capillary with piezoelectric actuated valve, active ISFET, and Redundancy ISFET

IV. The system of intelligent data evaluation:In the first stage a suitable macro measuring system as shown in Fig.6 is developed, the macro system will be able to evaluate measuring signals delivered by a matrix of ISFETs with cross sensitivity. The effective procedures of calibration and evaluation are to be found here. The second stage consists in an optimization and miniaturization process where necessary components for specific ASICs are to be developed.

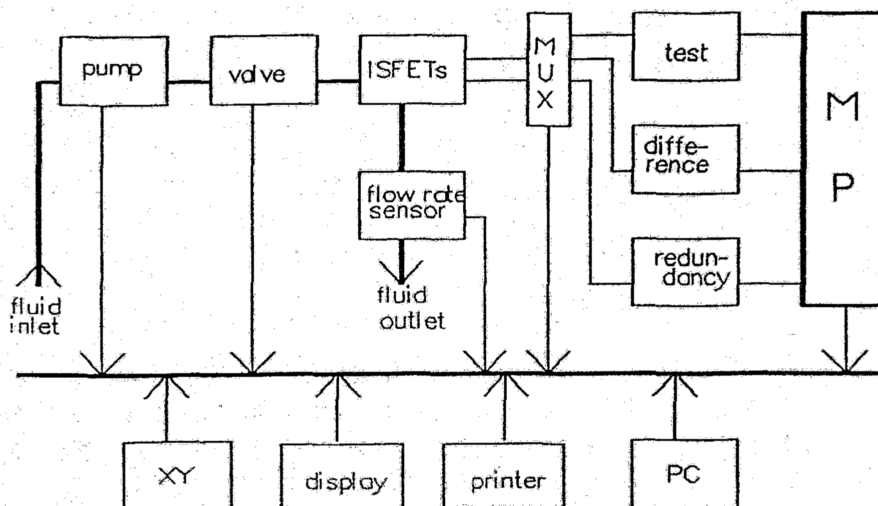

Fig.6: Schematic view of apparatus setup of macro measuring system [4]

References

[1] M.T. Pham, S. Howitz, COOPERATIVE PROJECT "FLUIDIC-ISFET-MICROSYSTEM";advanced by the Sächsisches Staatsministerium für Wirtschaft und Arbeit; Nov.1992-Dec.1994

[2] M. T. Pham, S. Howitz, ISFETs With Controlled Gate Membrane Opening; this report

[3] J. Joswig, Active Micromechanic Valve; Congress "Gerätetechnik und Mikrosystemtechnik"; Chemnitz 16.-18.March 1992

[4] M. T. Pham, M. Bürger, Differential Measurement with ISFETs of identical properties in FIM; Statusseminar-FIM, FhG IMS-2, Dresden 18.Dec.1992

Depth Profiles of C, N and O on Carbon Coated Steel Surfaces Made by IBAD

A. Kolitsch, E. Hentschel, and E. Richter

The influence of simultaneous deposition of carbon layers during ion implantation of nitrogen ions to the wear and friction behaviour of tool steel surfaces was investigated . An ion implanter without mass separator and a vacuum system with oil diffusion pumps was used. Such a vacuum system is a potential source of target contamination by hydrocarbon cracking products especially in connection with long implantation times. It is to investigate the influence of this carbon layer in means of wear and friction data and the characteristics of this layer system by elastic recoil detection analysis (ERDA).
In comparison to the ERDA results also AES depth profile measurement was used.

Samples of 210Cr46 tool steel were implanted with $8x10^{17}$ nitrogen ions/cm^2 of 50keV energy and a low beam density of 4μA/cm^2 at different vacuum conditions and different oxygen admixture of the ion source gas inlet (Table 1).

Table 1: Sample preparation

sample no.	baffle temperature	gas inlet for ion source
1	25°C	100% N_2
2	40°C	100% N_2
3	25°C	80% N_2/ 20% air
4	40°C	80% N_2/ 20% air
5	25°C	60% N_2/ 40% air
6	40°C	60% N_2/ 40% air

A conventional ERD geometry has been applied at the Rossendorf Tandem accelerator. The primary beam of 35 MeV ^{35}Cl ions was directed onto the target and a Bragg-ionisation chamber (BIC) was mounted at an angle of 30° with respect to the beam axis. The orientation of the target surface was chosen to keep a glancing angle of 15° for the incoming and outgoing particles. The quantitative treatment of extracting depth profiles has been done at a VAX station 3100 M76. The calculation of the stopping power is based on the code of Ziegler et al. [1] and on the Bragg rule for a composed system. Assuming only elastic processes with the Rutherford cross section the spectra of the recoiled Fe, O, N and C ions as well as of the scattered primary Cl ions are calculated. The target matter is simulated in 300 slabs by trial profiles of Fe, O, N and C. The trial profiles are fitted in an automatical procedure by comparing the calculated and measured spectra. Typically 30 to 50 iterations are necessary to produce a perfect fit of all the recoil spectra and a fairly well approximation of the projectile spectrum. A physically re-liable data smoothing is done by using a Wiener-Kolmogoroff-filter.

The wear is reduced drastically after N^+ implantation in the samples No. 3 and 4 with a small oxygen inlet in the nitrogen ion source followed by samples No. 1 and 2 without oxygen inlet (see Fig.1). The implantation with a higher oxygen content of the nitrogen

ion beam decreases the wear resistance (samples No. 5 and 6) up to the values of non implanted steel (No. 0).
On the other hand, it is to recognise that in all cases the implantation with 40°C tempered baffles of the oil diffusion pumps produces a better wear resistant layer than with 25°C tempered baffles. The wear resistance as a function of optimised carbon coating process means to optimise the deposition rate as a function of the baffle temperature and means to optimise the carbon layer thickness as a function of the duration in the implantation chamber.
Fig.2 illustrates the attached energy spectrum of the ^{35}Cl projectiles and the recoiled Fe, C, N, and O atoms.
The calculated depth profiles of Fe, C, N, and O are to see in Fig. 3. The range order of these elements in the surface region is well defined. The start of the iron profile is not exactly at the surface. To be observed is a wide oxygen profile immediately on the iron surface and with a range into the iron surface. It is evident that the original steel surface is coated by an iron oxide film caused by the stay in air.
On this oxygen profile was analysed a carbon layer immediately at the steel surface. And the analysed nitrogen profile has a range order through the carbon, oxygen, and iron surface profiles. The nitrogen profile resulting from the implantation process with 50 keV N^+ ions has not only caused the composition of chemical compounds in the steel matrix but also an ion beam induced mixing process is effected in the surface region. This mixing effect at the interfaces and the ion beam assisted deposition of the carbon layer are creating the good wear resistance by high adhesion of the carbon layer and formation of chemical compounds. The flat geometry of the nitrogen profile refers to the dynamical growth of the carbon layer on the surface at the long implantation time.
The samples 1...6 show nearly the same depth profiles. The resulting range order of the depth profiles is not changed. The different wear resistance cannot be explained by depth profiling. The most thick carbon layer with greatest peak height has been measured after implantation with an ion beam without oxygen particles, but this sample doesn't show the best wear resistance. The sample with the best wear resistance is the smallest carbon layer of sample No. 4 with a medium air inlet into the ion source. An increasing of the hydrocarbon cracking products in the vacuum chamber causes a thicker carbon layer. The comparable investigations of this layer system by AES depth profiling have the same results.

The results have shown that elastic recoil detection analysis is a very good instrument for depth profiling of thin layers of light elements in metals. The method allows the analysis of profiles down to concentrations of about 0.01% of the stoichiometric ones and the depth resolution up to 5 or 10 nm.
The investigated problem of ion beam assisted deposition of carbon layers simultaneously to the nitrogen ion implantation into steel caused by coating of hydrocarbon cracking products of oil diffusion pumps could be explained in direction to the layers structure, the range order of the surface layers, and the element distribution in the near surface region. For the explanation of the wear resistance behaviour it is necessary to analyse additionally the phase state, lattice parameters, and chemical bonding especially of the carbon layer in direction of diamond like carbon and the sp^2/sp^3 bonding.

References

[1] J.F. Ziegler, J.F. Biersack and U. Littmark, The stopping and range of ions in solids Pergamon Press, New York, 1985.

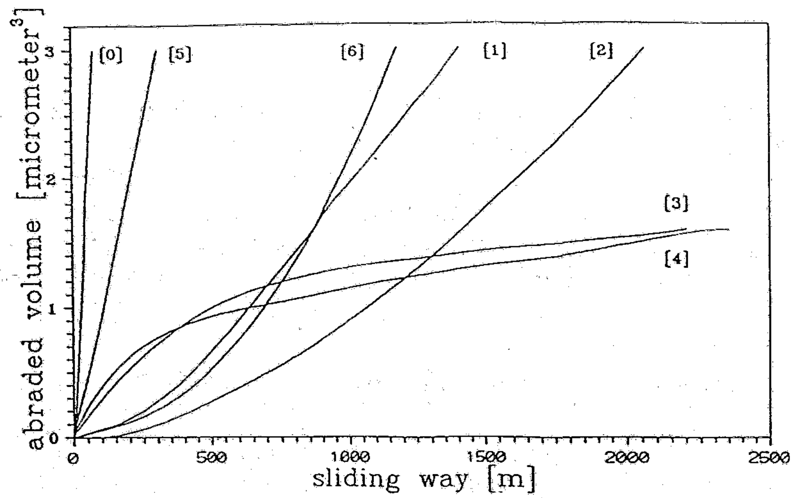

Fig. 1: Volume abrasion vs sliding distance for nonimplanted (No. 0) and implanted (No. 1 ... 6) 210Cr46 tool steel

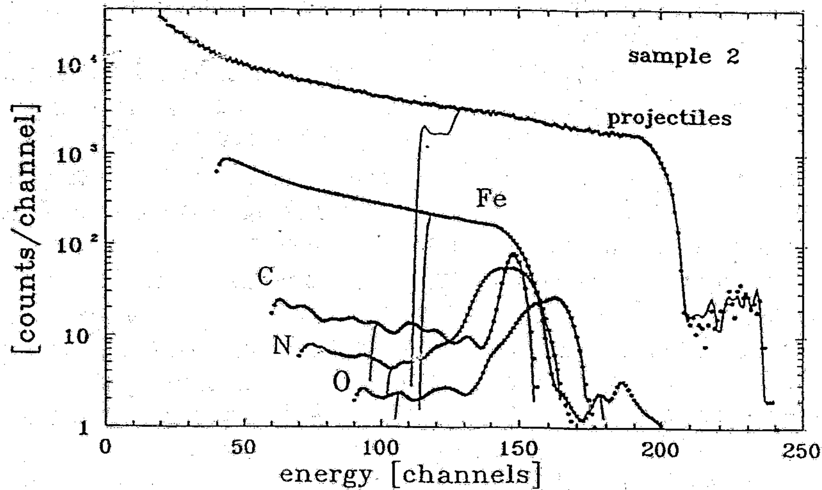

Fig. 2: Energy spectra measured at sample 2 from atomic charge number 6 (C), 7 (N), 8 (O), 26(Fe) and 17(Cl)

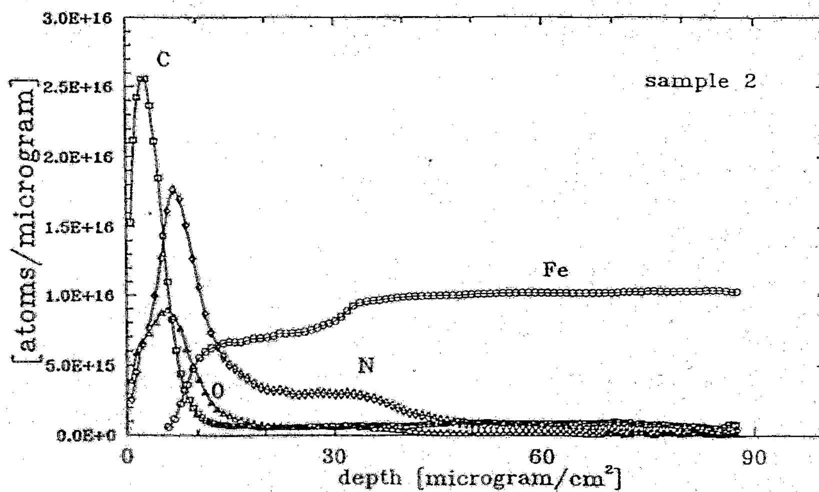

Fig. 3: Depth profiling of carbon, oxygen, nitrogen and iron measured by ERDA in 210Cr46 tool steel after ion implantation with 50keV N^+, $8x10^{17}$ ions/cm^2, 4μA/cm^2, 600 minutes stay in the vacuum chamber, 40°C thermostating of the baffles cooling water, gas inlet into ion source: 100% purest N_2

High Dose Implantation of Aluminium into Iron

H. Reuther, O. Nikolov[++*], S. Kruijer[++], R.A.Brand[++], W. Keune[++]
[++]Universität Duisburg, Laboratorium für Angewandte Physik, Lotharstr. 1–21, W–4100 Duisburg, Germany
[*] Permanent address: Institute of Nuclear Research, 72 boul. Tsarigradsko Shosse, BG–1784 Sofia, Bulgaria

Iron–aluminium alloys are of some interest both for fundamental research and for technology. Especially the iron–rich alloys show interesting magnetic properties because there is a transition from ferromagnetic Fe_3Al to non–magnetic FeAl at 33 at% Al [1]. In surface layers they can be produced by ion beam techniques especially by ion beam mixing [2–4] or by direct ion implantation [5]. In this paper the dose limit for the formation of the non–magnetic phases was determined. Moreover, depth selective CEMS (DCEMS) was applied to investigate which compounds or structures are formed at different depth.

Iron samples (1 mm thick, 99.99 % Fe) were implanted with doses between $1x10^{17}$ and $5x10^{17}$ cm^{-2} (50 and 100 keV energy) and $1x10^{18}$ cm^{-2} (200 keV). For the DCEMS investigations a 7 μm thick α–iron foil enriched to 95.10 % ^{57}Fe was used and implanted with $5x10^{17}$ cm^{-2} at 50 keV. The CEMS measurements were performed at room temperature. The same conditions as described earlier [6] were used. A description of the DCEMS system will be published later.

In Fig. 1 the CEM spectra and the calculated hyperfine field distributions of the aluminium implanted iron samples are shown for an energy of 100 keV. It is seen that a dose of $4x10^{17}$ cm^{-2} is necessary to produce non–magnetic components (singlet line). At an energy of 50 keV a dose of $5x10^{17}$ cm^{-2} was necessary while at 200 keV even with $1x10^{18}$ cm^{-2} other than ferromagnetic fractions appeared (a quadrupole doublet). At lower doses only hyperfine field distributions with ferromagnetic components were found. Moreover, all spectra contain the characteristic six–line–pattern of α–iron.

These results showed that not only the concentration but also the deposited energy is responsible for the kind of the formed structures.

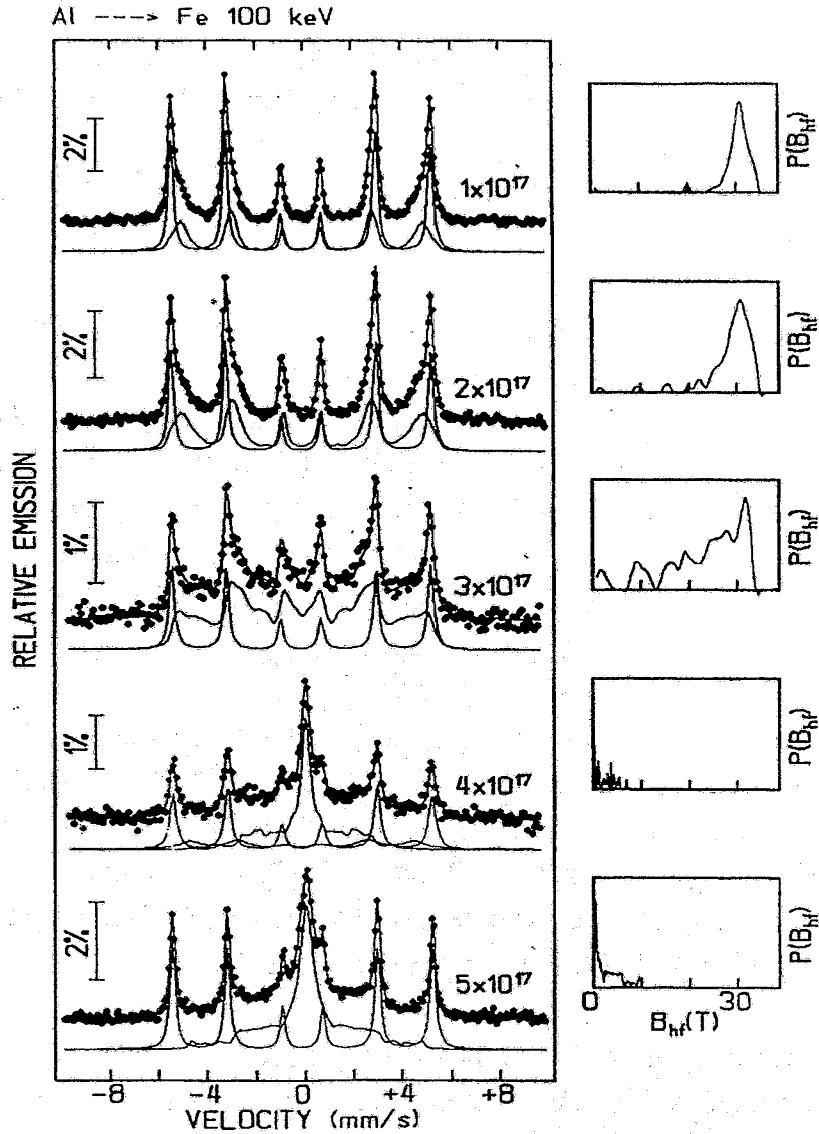

Fig. 1: CEM spectra and calculated hyperfine field distributions of Fe implanted with Al

The results of the DCEMS measurements are shown in Fig. 2. The spectra are plotted for various electron energies from top to bottom in the order of increasing probing depths. While for 6900, 6600, and for 13400 eV the spectrum consists of a main nonmagnetic component with minor magnetic fractions in the case of 12750 and 10500 eV magnetic components predominate. This means that the nonmagnetic phase is formed only in and near the sample surface.

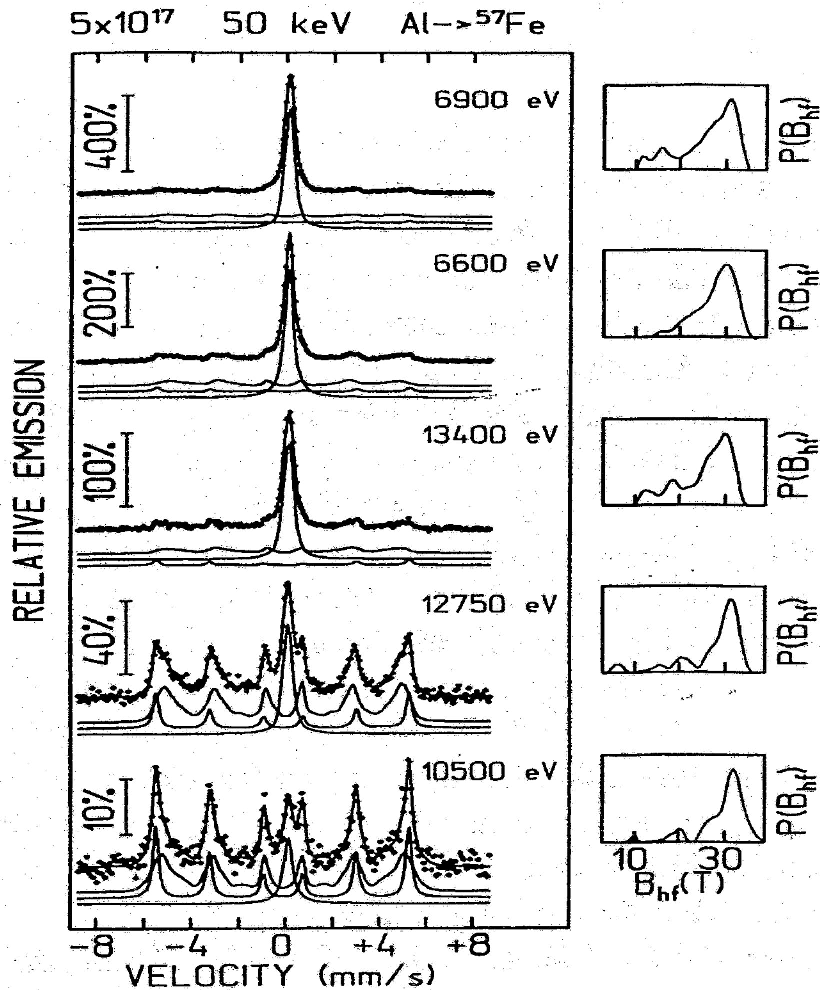

Fig. 2: DCEM spectra and calculated hyperfine field distributions of the Al implanted ^{57}Fe foil

References

[1] H. Chacham, E. Galvao da Silva, D. Guenzburger, and D.E. Ellis, Phys. Rev. B35, 1602 (1987).

[2] V.P. Godbole, S.M. Chaudhari, S.V. Ghaisas, S.M. Kanethar, S.B. Ogale, and V.G.Bhide, Phys. Rev. B31, 5703 (1985).

[3] C. Jaouen, J.P. Eymery, E.L. Mathe, and J. Delafond, Mat. Sci. Eng. 69, 483 (1985).

[4] M.A.Z. Vasconcellos, S.R. Teixeira, F.L. Freire, jr., M.C.S. Nobrega, P.H. Dionisio, W.H. Schreiner, and I.J.R. Baumvol, Mat. Sci. Eng. A104, 169 (1988).

[5] H. Reuther, Nucl. Instrum. Methods B53, 167 (1991).

[6] H. Reuther, Nucl. Instrum. Methods B30, 61 (1988).

A Magnetron Source for Ion Implantation

H. Reuther

In the past the implantation of metal ions in sufficient doses ($5x10^{17}$ cm^{-2} and more) caused difficulties because of the lack of suitable ion sources. It was necessary to use light volatile or vaporable compounds of the metal and to separate the ion beam with the disadvantage of decrease of beam intensity [1].
Due to the development of sputter and vacuum arc sources (CHORDIS [2,3] and MEVVA [4]) these disadvantages have been redressed. Here an additional sputter source utilizing the magnetron sputter principle is presented.
The ion source was constructed on base of the well known magnetron principle used for sputter deposition [5]. A target is situated on a permanent magnet which generates the required magnetic gap field. The configuration of the magnetic field and the electrode array creates a ring shaped plasma of high density on the target surface. The discharge current contains both electrons, ions of the carrier gas and ions of the target. Moreover, a large amount of neutral particles is sputtered from the target.
The idea of the present work was to utilize the ionic fraction of the magnetron discharge current for an ion source. At bias sputtering at less than 500 V the ion current can already amount to up to 8 % of the total current [6]. The ion fraction is composed by ions of both the carrier gas and the target.
Using a magnetron discharge for an ion source two main problems have to be solved. The first is to overcome the difference between the pressure necessary for operating the magnetron (>0.1 Pa) and the pressure normally used for ion implantation ($<10^{-3}$ Pa). The second is to minimize the carrier gas fraction in the ion current. Both problems have been solved by the construction of the source and optimization of the working parameters.
Fig. 1 shows a section of the magnetron source. Heart of the source is the magnetron composed by the target (1), the rod magnet (2), the ring magnet (3), and the pole piece (4) producing the circular magnetic field, the inner (5) and the outer shielding (6), and the insulator in between (14). The target is water cooled (8). The argon carrier gas is filled in by the gas inlet (13). The magnetron discharge is started by putting a voltage of some 100 V between target and outer shielding. This is the normal magnetron operation which could be used for deposition processes.
The idea was to include the magnetron discharge in a chamber with a small aperture for the ion extraction flux. Therefore the outer shielding was lengthened and closed

with a lid (9). This lid has a circular aperture and serves as ion extraction screen. The lid is water cooled. In front of the extraction plate an also water cooled plate for suppressing secondary electrons (10) is situated. Behind it the screen at implanter terminal potential is mounted (11).

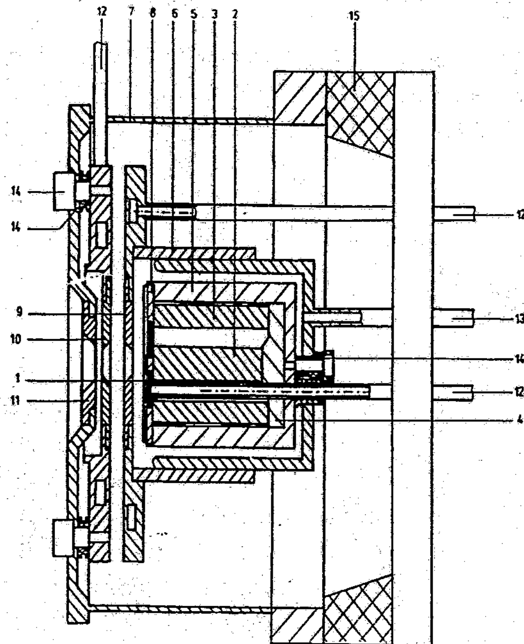

Fig. 1: Section of the magnetron ion source

The source holder together with the power and water cooling connections is mounted on a flange. Between this and the implanter terminal beam line the high voltage insulator (15) is situated. The source is screened from the other components of the implanter terminal beam line by a cylindrical tube (7).

The inclusion of the magnetron in a pot with an only small aperture has the advantage that the pressure in the source can be much higher than in the recipient. It is necessary both for the magnetron operation and the ion implantation process.

The source was tested with Mo, Al, Cu, Ti, and Ta sheets as source targets. The fraction of metal ions in the ion beam was determined at different carrier gas pressures. Argon was the carrier gas in every case. The highest metal ion fractions were surprisingly detected at the highest carrier gas pressure. The integral currents were in the range of some mA, the maximum metal ion fraction was between 47 % for Ti and 83 % for Cu. [7]

References

[1] N. Sakudo, Nucl. Instrum. Methods **B21**, 168 (1987).

[2] R. Keller, P. Spädtke, and H. Emig, Vacuum **36**, 833 (1986).

[3] B. Torp, B.R. Nielsen, D.M. Rück, H. Emig, P. Spädtke, and B.H. Wolf, Rev. Sci. Instrum. **61**, 595 (1990).

[4] I.G. Brown, M.R. Dickinson, J.E. Galvin, X. Godechot, and R.A. MacGill, Proc. 7th Int. Conf. on Surface Modification of Metals by Ion Beams, Washington, D.C., July, 1991.

[5] S. Schiller, U. Heisig, and K. Goedicke, J. Vac. Sci. Technol. **14**, 815 (1977).

[6] S. Schiller, U. Heisig, and K. Goedicke, Thin Solid Films **40**, 327 (1977).

[7] H. Reuther, Nucl. Instrum. Methods **B71**, 87 (1992).

Modelling of Implantation-Induced Transient Diffusion and Electrical Activation of Boron in Crystalline Silicon during Post-Implantation Annealing

H. U. Jäger

The formation of shallow p-type regions in crystalline silicon by low-energy boron ion implantation and subsequent thermal annealing is characterized by some specifics (see refs. [1,2], and the refs. cited therein). Fig. 1 shows typical experimental data from the literature as well as results from our simulations. For such a low-temperature furnace annealing at 800°C the normal diffusion is known to be negligible. However, in case of post-implantation annealing the as-implanted boron profiles become modified in their tail regions up to a critical concentration c_{enh} of about $4x10^{18}$ cm^{-3}, which is of the same order of magnitude as the intrinsic carrier concentration n_i at this temperature, but far below the corresponding boron solid solubility limit c_{sol} = $3.2x10^{19}$ cm^{-3}. This implantation-induced tail diffusion relaxes within a time period of about 30 min. The non-diffusing, static boron peak region above c_{enh} is found to be electrically inactive (Fig. 1c). It becomes electrically active only after annealing periods of many hours.

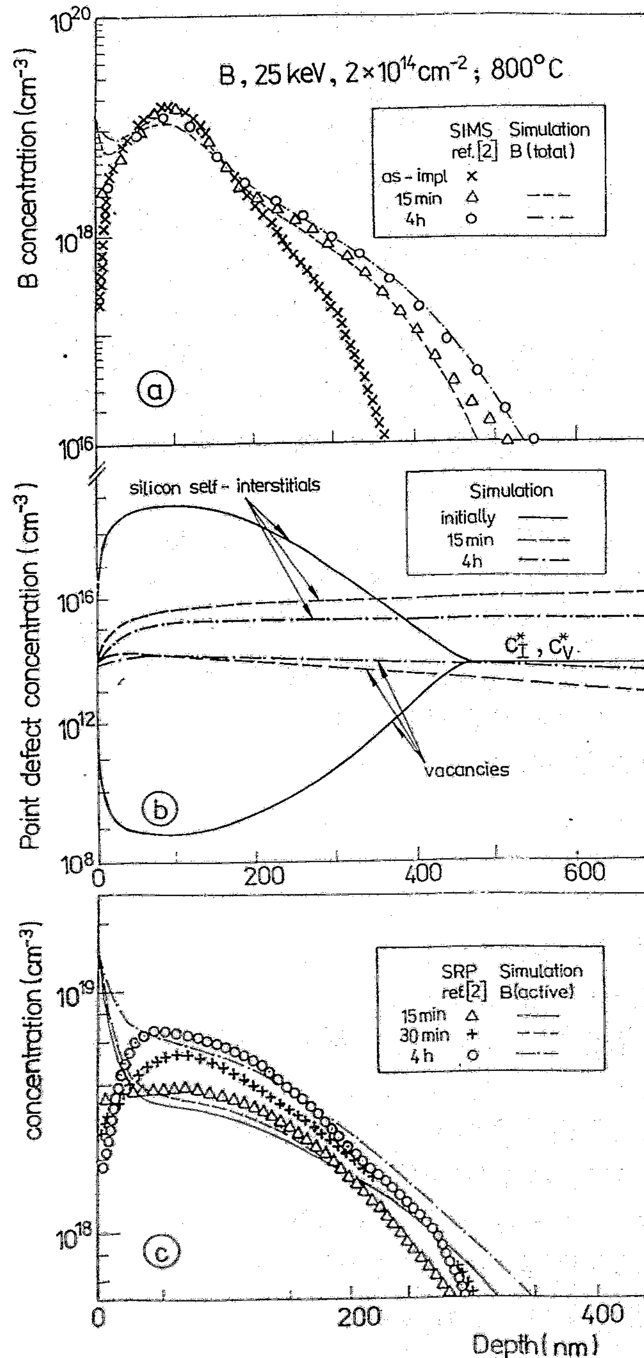

Fig. 1: Time evolution of a) boron atomic profiles, b) point defect distributions and c) electrical profiles in silicon during 800°C furnace annealing after 25keV $2x10^{14}cm^{-2}$ B ion implantation. The simulations are compared with boron profiles which have been measured by Cowern et al. [2] using secondary ion mass spectroscopy (SIMS) and spreading-resistance profiling (SRP).

We have modelled this boron diffusion and activation by a system of coupled diffusion-reaction equations [3]. For the diffusion terms in the equations, the concept of point defect impurity pair diffusion [4] has been adopted. A dopant concentration $c_{A,solved}$ not exceeding the solid solubility limit c_{sol} is assumed to consist of ionized substitutional dopant atoms A^q_{sub} (acceptors: q=-1) and of neutral dopant atoms A_{int} on interstitial sites. Besides vacancies V^z and silicon self-interstitials I^z in various charge states z are taken into account. The substitutional dopant atoms and the point defects form the pairs

$$A^q_{sub} + I^z \Longleftrightarrow (A^q_{sub} I^z) , \quad (1)$$

$$A^q_{sub} + V^z \Longleftrightarrow (A^q_{sub} V^z) \quad (2)$$

which are postulated to be the only dopant-containing diffusing vehicles. In addition, there have been assumed (i) local equilibrium between the reaction partners in eqs. (1) and (2), (ii) local equilibrium for all reactions changing the charge states of the species, and (iii) pair concentrations which are dilute compared to the concentrations of isolated dopants and point defects.

We suggest that during annealing the interstitial outdiffusion to the surface or into the bulk leads to an increase of boron activation via the "kick-out" reaction

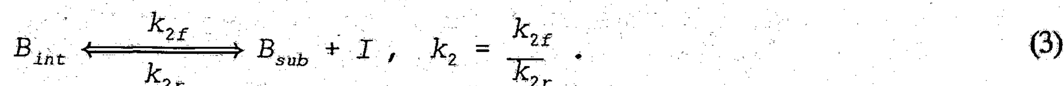

$$B_{int} \underset{k_{2r}}{\overset{k_{2f}}{\Longleftrightarrow}} B_{sub} + I , \quad k_2 = \frac{k_{2f}}{k_{2r}} . \quad (3)$$

If this idea is accepted, it is formally straightforward to take into account also the interstitial-vacancy annihilation or generation

$$I + V \underset{k c_I^* c_V^*}{\overset{k}{\Longleftrightarrow}} 0 , \quad (4)$$

and the incorporation of boron on substitutional sites by vacancy annihilation (Frank-Turnbull mechanism)

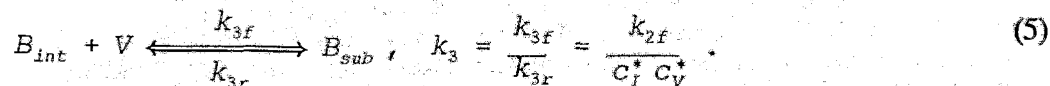

$$B_{int} + V \underset{k_{3r}}{\overset{k_{3f}}{\Longleftrightarrow}} B_{sub} , \quad k_3 = \frac{k_{3f}}{k_{3r}} = \frac{k_{2f}}{c_I^* \, c_V^*} . \quad (5)$$

These reactions have been taken into account under nonequilibrium conditions, their respective reaction rates in foreward and backward direction are defined in formulae (3) -(5), too. The symbols c_I^* and c_V^* denote, as usual, the equilibrium concentrations of neutral interstitials and vacancies, respectively.

The present investigations are aimed at the modelling of implantation-induced effects in boron diffusion and activation, but the details of defects evolution during ion implantation and during heating up to the annealing temperature are beyond the scope of this study. Therefore the problem arises to find adequate initial defect distributions. Let us postulate that a very early stage of annealing exists, where diffusion is still unimportant, but local equilibrium between the reactions (3) - (5) has been already achieved. The local equilibrium obtained can be characterized by the concentration difference $Q = c_I - c_V - c_{B,sub}$, which is not changed by the reactions (3) - (5). A depth region with originally equal numbers of interstitials and vacancies and only inactive boron atoms ($c_{B,sub}$=0) is characterized by Q=0 and equilibrates, in this approximation, to the concentrations

$$c_{B,sub} = c_I = \frac{k_2}{2}\left(-1+\sqrt{1+\frac{4c_{B,solved}}{k_2}}\right), \quad c_V = \frac{c_I^* c_V^*}{c_I} < c_I . \tag{6}$$

The states in eq. (6) calculated for all individual depth intervals represent our initial distribution in solving the complete system of diffusion-reaction equations.

The calculations have been performed using the new module for point defect - based diffusion [5] in the one-dimensional process simulator TESIM [6]. All the diffusion parameters, incl. c_I^* and c_V^*, have been adopted from the work of Rorris et al. [7]. The other kinetic parameters characterizing the reactions (3) - (5) have been obtained by fits to experimental data. As a consequence of our model parameters both the interstitial-assisted boron diffusion (1) and the interstitial-assisted boron activation (3) are predicted to be dominant. Our assumption that interactions between a substitutional boron atom B_{sub} and an interstitial I may lead to two different reaction products (compare eqs. (1) and (3)) is new. It is considered to be a possible approach and has conceptually a similar function as the dynamic clustering model in the investigations of Cowern et al. [8].

Acknowledgements
This work was supported in part by the Bundesministerium für Forschung und Technologie under Grant No. 211-5291-03-HE3ROS. Thanks are also due to the Fraunhofer-Institut für Mikroelektronische Schaltungen und Systeme, Institutsteil Dresden for the possibility to work in this institute as guest scientist.

References

[1] S. Solmi, F. Baruffaldi, and R. Canteri, J. Appl. Phys. **69** , 2135 (1991)
[2] N. E. B. Cowern, K. T. F. Janssen, and H. F. F. Jos, J. Appl. Phys. **68** , 6191 (1990)
[3] H. U. Jäger, 8th International Conference on Ion Beam Modification of Materials, Heidelberg, Germany, Sept. 7 - 11, 1992, contr. paper P232; to be published in Nucl. Instr. & Meth. Phys. Res. B
[4] B. J. Mulvaney and W. B. Richardson, Appl. Phys. Lett. **51** , 1439 (1987)
[5] J. Pönisch, Diploma Thesis, Technische Universität Chemnitz, Sektion Mathematik, 1990
[6] TESIM4, Fraunhofer-Institut für Mikroelektronische Schaltungen und Systeme, Institutsteil Dresden; Grenzstraße 28, O-8080 Dresden, Germany
[7] E. Rorris, R. R. O'Brien, F. F. Morehead, R. F. Lever, J. P. Peng, and G. R. Srinivasan, IEEE Trans. Comp.-Aided Design **9** , 1113 (1990)
[8] N. E. B. Cowern, H. F. F. Jos, K. T. F. Janssen, and A. J. H. Wachters, Mat. Res. Soc. Symp. Proc. **163** , 605 (1990)

Computer Simulation of Channeling Implantation of Phosphorus into Silicon

M. Posselt

In the last two years detailed experimental investigations on channeling implantation of phosphorus, boron and nitrogen at energies between 10 keV and 2 MeV have been performed (cf. [1-5] and references therein). Theoretical calculations of range distributions for channeling implantation of heavy ions are relatively difficult since the shape of the range profiles is strongly influenced by the radiation damage produced during ion bombardment. Furthermore, the shape of the range distributions depends on the alignment and the divergence of the ion beam and on the thickness and the structure of the thin amorphous oxide layer on silicon. We developed the binary collision code Crystal-TRIM to simulate ion implantation into single-crystalline solids. This program has been elucidated in detail in refs. [3-5]. The electronic stopping of the ions is described by a modified Oen-Robinson formula: The electronic energy loss is an exponential function of the impact parameter. It is normalized to the ZBL electronic stopping cross-section [6]. The motion of the projectile in the thin amorphous surface layer is simulated similarly to the TRIM program [6] using the mean atomic distance as the free flight path. The generation and accumulation of radiation defects during ion irradiation is taken into account approximately [3-5]. We assume that in the crystalline target Frenkel pairs are produced by ballistic processes. The recombination of vacancies and interstitials is neglected. The lattice positions of the interstitials during ion bombardment are not known exactly. In our algorithm we regard the interstitials as randomly displaced from tetrahedral sites within a sphere. As the radius of the sphere we choose the mean atomic distance in the crystalline target. The ion dose D_o is simulated by N pseudoprojectiles. Each pseudoprojectile corresponds to a dose increment $dD = D_o/N$. In a depth interval $(x, x+\Delta x)$ of the target the

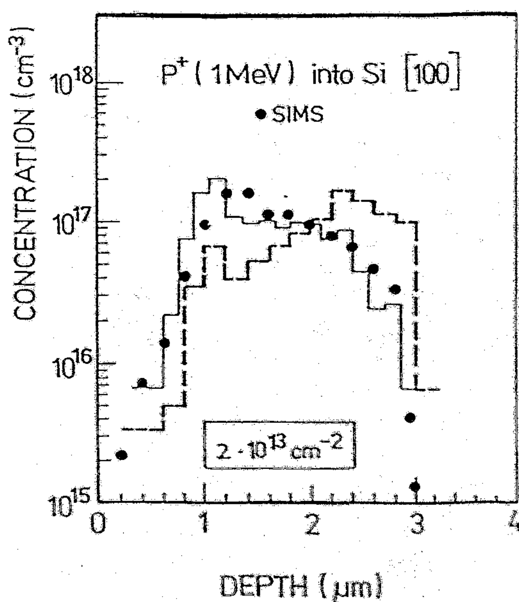

Fig. 1: Range profiles for 1 MeV channeling implantation of P^+ into silicon. The experimental data were obtained by SIMS depth profiling (Raineri et al. [1,2]). The theoretical profiles were calculated without (thick dashed line) and with (thin solid line) the consideration of an amorphous surface layer of $50 \AA$ thickness.

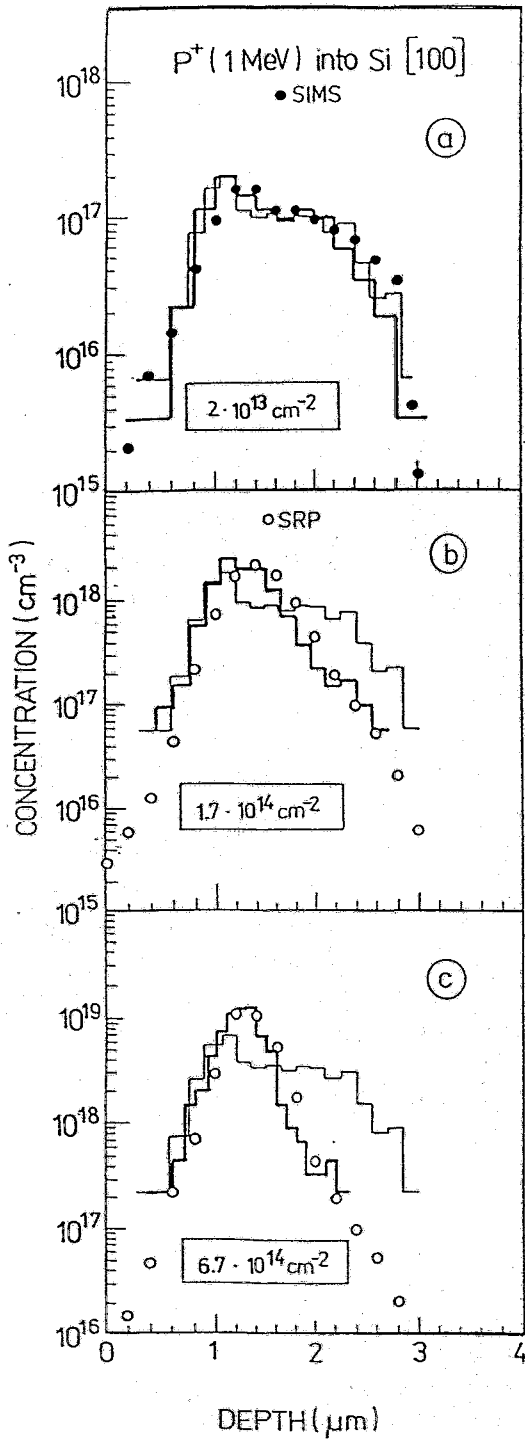

Fig. 2: Range profiles for 1 MeV channeling implantation of P^+ into silicon at different doses. The experimental data were obtained by Raineri et al. [1,2] using SIMS and spreading resistance depth profiling (SRP). The theoretical profiles were calculated without (thin solid lines) and with (thick solid lines) the consideration of radiation-induced defect production. The thickness of the amorphous surface layer was assumed to be 50 Å.

probability dp_{d} that an atom is displaced by a pseudoprojectile is given by

$$dp_{\mathrm{d}} = \frac{1}{n}\,(\frac{N_{\mathrm{d}}}{\Delta x}dD)\;(1-p_{\mathrm{d}}) \tag{1}$$

where n is the atomic density in the crystalline target. The quantity N_{d} denotes the number of displacements which would be created in $(x, x+\Delta x)$ if the pseudoprojectile would be implanted into a virgin crystal. The reduction of the number of atoms which can be displaced from their sites is taken into account by the factor

$(1 - p_d)$. The probability p_d is equal to the probability p_V that a lattice site is occupied by a vacancy. In general the depth profiles of vacancies are nearly equal to the depth distributions of the interstitials apart from a small shift. Therefore, we set the probability p_I that in the depth interval $(x, x + \Delta x)$ an interstitial site is occupied equal to p_V. In $(x, x + \Delta x)$ uniform distributions of vacancies and interstitials according to the probabilities p_V and p_I are assumed.
For the first time the dose dependence of range profiles in high energy channeling implantation was simulated by a binary collision code. Range distributions calculated by Crystal-TRIM are shown in Figs. 1 and 2. The range profiles obtained from channeling implantation experiments of Raineri et al. [1,2] are also given. Fig. 1 shows theoretical range profiles calculated without and with the consideration of a thin amorphous oxide layer. In both cases the generation and accumulation of radiation-induced defects was not taken into account. The amorphous surface layer leads to an important reduction of the channeling component of the range distribution. The best fit to experimental results is obtained if a layer thickness of about $50 \AA$ is assumed. However, the real thickness of the surface oxide was less than $20 \AA$ [7]. Fig. 2a shows that at the low dose of $2 \times 10^{13}\ cm^{-2}$ the additional consideration of radiation-induced production of vacancies and interstitials does not yield significant changes. However, with increasing dose this effect becomes more and more important. This is illustrated by the comparison of the range profiles calculated with and without the consideration of radiation-induced defect production (Figs. 2b and c). The agreement between experimental data and simulations at higher doses shows that the simple model of radiation-induced defect production works. The main reason is the fact that concerning the channel of incidence a nearly complete dechanneling occurs already at small defect concentrations. Consequently, the shape of the range distributions does not depend on details of the defect evolution at higher defect concentrations. We also performed computer simulations of $1\ MeV$ phosphorus implantation into silicon into the $< 110 >$, $< 111 >$ axial and into the (110) planar directions. Similar results as in the example discussed here were found.

References

[1] V. Raineri, R. Setola, F. Priolo, E. Rimini and G. Galvagno, Phys. Rev. B44, 10568 (1991).

[2] G. Galvagno, V. Raineri, R. Setola, F. Priolo and E. Rimini, Nucl. Instr. & Meth. Phys. Res. B 67, 476 (1992).

[3] M. Posselt, Int. Conf. on Computer Simulations of Radiation Effects in Solids (COSIRES'92), Berlin, Aug. 23-28, 1992, inv. paper 1.9, to be published in Radiation Effects & Defects in Solids (1993).

[4] M. Posselt, 8th Int. Conf. on Ion Beam Modification of Materials (IBMM'92), Heidelberg, Sept. 7-11, 1992, contr. paper P012, to be published in Nucl. Instr. & Meth. Phys. Res. B (1993).

[5] M. Posselt, MRS 1992 Fall Meeting, Symposium A: Beam-Solid Interactions: Fundamentals & Applications, Boston, Nov. 30 - Dec. 4, 1992, contr. paper A1.3, to be published in MRS Symp. Proc. (1993).

[6] J.F. Ziegler, J.P. Biersack and U. Littmark, The Stopping and Range of Ions in Solids, Pergamon Press, New York, 1985.

[7] V. Raineri, private communication.

Dielectric Theory of Electronic Energy Loss in a Homogeneous Electron Gas: Effect of First-Order Polarization

R. Mathar

The electronic energy loss of a bare ion with charge $\rho(\mathbf{r},t)=Z_1 e\delta(\mathbf{r}-\mathbf{v}t)$ travelling through a homogeneous medium characterized by the dielectric function ε is given by [1].

$$S=-\frac{Z_1^2 e^2}{2\pi^2\varepsilon_0 v^2}\int_0^\infty \frac{dk}{k}\int_0^{kv}\omega\,\mathrm{Im}\frac{1}{\varepsilon(k,\omega)}\,d\omega$$

Z_1 denotes the ion atomic number, e the elementary charge, and v the ion velocity. The theory covers the whole non-relativistic velocity range. The Dyson equation for the effective interaction potential associates ε with the bare Coulomb potential $U_0(k,\omega)=e^2/(\varepsilon_0 k^2)$ and the proper polarization $\Pi^*(q)$ [2]

$$\varepsilon(q)=1-U_0(q)\Pi^*(q),$$

the solo arguments meaning both, wavenumber and frequency. We take an electron gas with homogeneous positive background as the medium: a reliable estimate of ε also serves as an input to other places: the exchange-correlation energy functional in density functional theory [3] or the contribution of nonlinear susceptibilities to electronic stopping [4]. The widely used random phase approximation (RPA) cuts the expansion of Π^* into powers of the electron-electron interaction potential

$$\Pi^*(q)=\Pi^{*(0)}(q)+\Pi^{*(1)}(q)+\ldots$$

behind the zero order [5]. This work tests the scope of the RPA by adding $\Pi^{*(1)}$, i.e. the

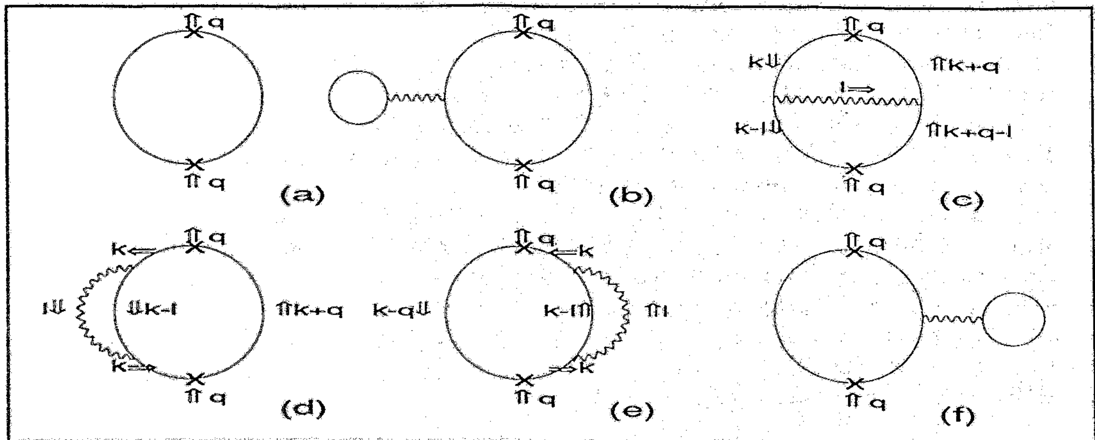

Fig. 1: Feynman diagrams of zero-order polarization (RPA) (a) and first-order polarization (b)-(f)

sum of the other five Feynman diagrams depicted in Fig. 1. As the previous equation is also an expansion in powers of the mean electronic distance, the RPA becomes exact at high electron densities. The three Feynman integrals

$$\Pi_{c}^{*(1)}(q)=(-2)\left(\frac{i}{\hbar}\right)^{2}\int\frac{d^{4}k\,d^{4}l}{(2\pi)^{8}}G^{0}(k)\,G^{0}(k-l)\,G^{0}(k+q-l)\,G^{0}(k+q)\,U_{0}(l)$$

$$\Pi_{d,e}^{*(1)}(q)=(-2)\left(\frac{i}{\hbar}\right)^{2}\int\frac{d^{4}k\,d^{4}l}{(2\pi)^{8}}G^{0}(k)\,G^{0}(k-l)\,G^{0}(k)\,G^{0}(k\pm q)\,U_{0}(l)$$

could be reduced to analytical expressions containing double integrals, which were finally evaluated numerically. The indices refer to the individual diagrams of Fig. 1. G^{0} denotes the Green's function of the non-interacting electron gas. $\Pi_{b}^{*(1)}$ and $\Pi_{f}^{*(1)}$ are zero. $\Pi_{c}^{*(1)}$ is known to be the only first-order term to contribute to the second-order correlation energy [6]. Fig. 2 shows the change of the electronic stopping due to the improved calculation at several electron gas densities versus the ion velocity.

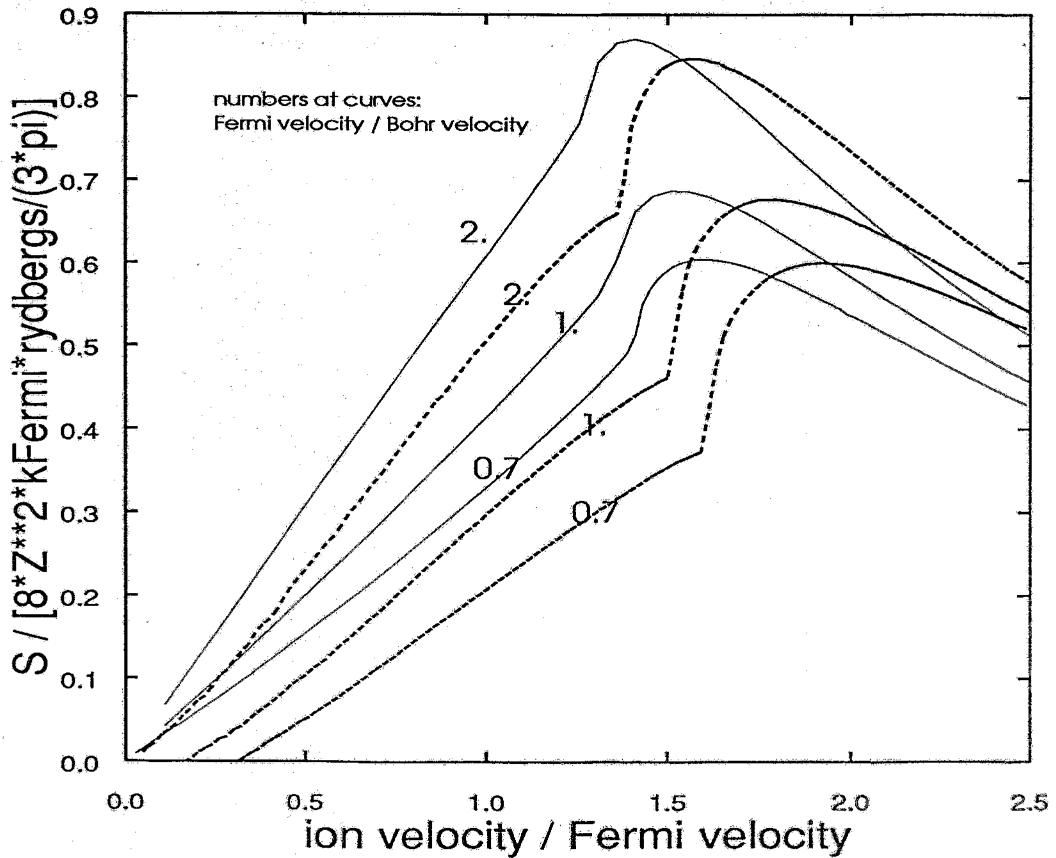

Fig. 2: Stopping of a bare ion by RPA only (full lines) and with first-order polarization included (dashed lines) in units of (8 Z_1^2 k_F rydbergs)/(3π)

The stopping power is strongly reduced compared to RPA in the low velocity and increased in the high velocity regime: whereas $\Pi_{c}^{*(1)}$ increases the stopping at low velocities, $\Pi_{d+e}^{*(1)}$ diminishes it roughly twice as much. The start of plasmon excitation is shifted towards higher energies. The improved calculation approaches the RPA in the limit of Fermi velocities much higher than the realistic values chosen in Fig. 2.

Stopping powers less than zero in the low velocity, low density regime indicate the insufficiency of the calculations just up to order $\Pi^{*(1)}$ as well. The inclusion of the nonlinear response of the homogeneous electron gas is predicted to increase the electronic stopping at low velocities [4]. Consequently, the RPA needs not to be as bad as Fig. 2 holds.

This work is supported by the Bundesministerium für Forschung und Technologie, grant No. 211-5291-03-HE3ROS.

References

[1] J. Lindhard and A. Winther, Mat. Fys. Medd. Dan. Vid. Selsk. 34, no. 4, 1 (1964)
W. Brandt and M. Kitagawa, Phys. Rev. B 25, 5631 (1982)
[2] A. Fetter and J. D. Walecka, Quantum Theory of Many Particle Systems, Mc-Graw-Hill, 1971
[3] P. Hohenberg and W. Kohn, Phys. Rev. 136, B864 (1964)
[4] C. D. Hu and E. Zaremba, Phys. Rev. B 37, 9268 (1988)
[5] J. Lindhard, Dan. Mat. Fys. Medd. 28, no. 8, 1 (1954)
[6] L. Onsager, L. Mittag and M. J. Stephen, Ann. Physik, Bd. 18, 72 (1966)

Molecular Dynamics Simulations of Defect Formation by Low-Energy Ion Bombardment

D. Stock* and K.-H. Heinig
*Friedrich Schiller University, Faculty of Physics and Astronomy,
Max-Wien-Platz 1, O - 6900 Jena

Recent applications of ion beams for nonequilibrium processing and modification of materials have caused a considerable need for a detailed understanding of the dynamics of energetic collision cascades including the production of damage. The controlled modification of the structural kinetics at the surface and in the near-surface region by low-energy ($< 1keV$) ion bombardment, in particular, requires a subtle knowledge of the number and the spatial configuration of the produced elemental point defects.
By using computer simulations based on binary collision codes such as Crystal-TRIM, however, it is difficult to obtain quantitatively reliable results for the generation and the possible migration and recombination of defects.

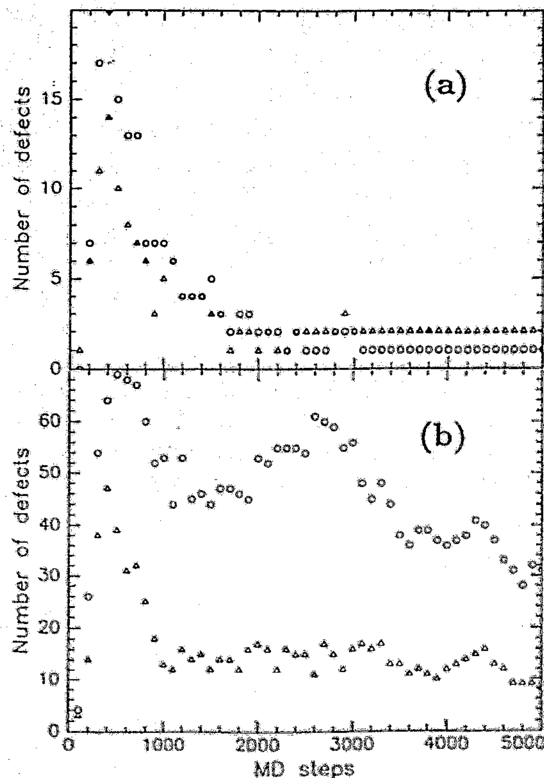

Fig. 1: Temporal evolution of the number of defects for (a) $100eV$ and (b) $500eV$ Si bombardment of (001) Si; circles: vacancies, triangles: tetrahedral interstitials

We have studied the defect formation during the Si ion bombardment of a Si (001) surface layer by molecular dynamics (MD) simulations. The crystallite has a surface of $10a_0 \times 10a_0$ ($a_0 = 5.42$ Å is the lattice constant) and a depth of $6a_0$; it contains 4800 atoms. The trajectories of the incident Si ion and all target atoms have been calculated numerically by integration of Newton's equations of motion using the Stillinger-Weber potential for silicon which has been splined to a screened Coulomb potential towards higher energy (> 30 *eV*) as described in ref. [1]. The applied boundary conditions are the same as in ref. [2]. The lattice damage caused by low-energy ion bombardment can be understood in terms of creation of vacancy-interstitial pairs. Fig. 1 illustrates the typical temporal evolution of the number of vacancies and tetrahedral interstitials during collision cascades initiated by 100 *eV* and 500 *eV* Si ions incident on a (001) Si surface with a tilt angle of 7°. In the collisional phase of the cascade, until $0.2 - 0.3$ *ps* (600 - 900 MD steps), the lattice is in maximum disorder. A maximum number of "vacancies" and "interstitials" have formed. This corresponds to the formation of extended voids (clusters of vacancies) surrounded by interstitial atoms. However, these defects are not stable, and as in the case of 100 *eV* bombardment (Fig. 1a), many of them spontaneously recombine within the next half of a *ps*. It should be noted that due to the strong lattice distortion during the early phase of the cascade the definition of a defect may be difficult. After 1.2 *ps* (3000 MD steps) the number of defects is constant. One vacancy - interstitial pair has formed. In the case of 500 *eV* bombardment (Fig. 1b) we clearly observe that the vacancies need more time to relax than interstitials. This is obviously due to the fact that vacancies are produced near the surface, where the primary collision started. The depth distribution of defects is not shown here [1]. The difference between the number of vacancies and the number of tetrahedral interstitials balances the number of nontetrahedral interstitials plus the number of adatoms plus the number of sputtered target atoms.

References

[1] K.-H. Heinig and D. Stock, to appear in Nucl. Instr. and Meth.;
D. Stock and K.-H. Heinig, MRS Fall Meeting, Symposium A Beam Solid Interactions: Fundamentals & Applications, Boston, USA, Nov. 30 - Dec. 4, 1992, contr. paper A7.11.

[2] K.-H. Heinig and D. Stock, Thermalization in Collision Cascades Investigated by Molecular Dynamics Calculations, this annual report.

Thermalization in Collision Cascades Investigated by Molecular Dynamics Calculations

K.-H. Heinig and D. Stock*
*Friedrich Schiller University, Faculty of Physics and Astronomy,
Max-Wien-Platz 1, O-6900 Jena

The slowing down of a low-energy ion in a solid through atom-atom collisions leads to fast dissipation of its kinetic energy. After a few 10^{-13} s, in the region of the collision cascade a thermal velocity distribution is expected, therefore a local temperature can be defined. This elevated temperature lasts for a few 10^{-12} s, then the heat will have been transferred to the surrounding material by heat conduction. Despite of the transient and local character of the temperature increase, one expects a strong influence on the kinetics of amorphization and defect production. On the one hand, the elevated temperature delivers the excitation energy necessary for a partial annealing of defects produced by the collision cascade. On the other hand, if after the collision cascade the local temperature exceeds the melting temperature of the target material, amorphization could be produced by rapid melting and subsequent quenching of the melt in "thermal spikes".
Here, these qualitative arguments have been verified for silicon by molecular dynamics calculations [1]. The trajectories of the low-energy ion and all target atoms have been calculated numerically by integration of Newton's equations of motion using the interatomic interaction potential described in ref. [2]. Our simulation cell is a crystallite with the dimensions of $15a_o \times 15a_o \times 15a_o$ ($a_o = 5.42$ Å is the lattice constant) consisting of 27000 Si atoms. In x- and y-direction periodical boundary conditions are used. The top layer (at $z = 0$) is a free crystal surface where no constraints were applied. On the opposite side of the crystallite the atoms of the bottom layer were fixed to their lattice positions in order to simulate the substrate. To ensure dissipation of energy transferred to the simulation cell by the projectile, the atoms of the four crystal layers next to the bottom layer act as a heat bath.

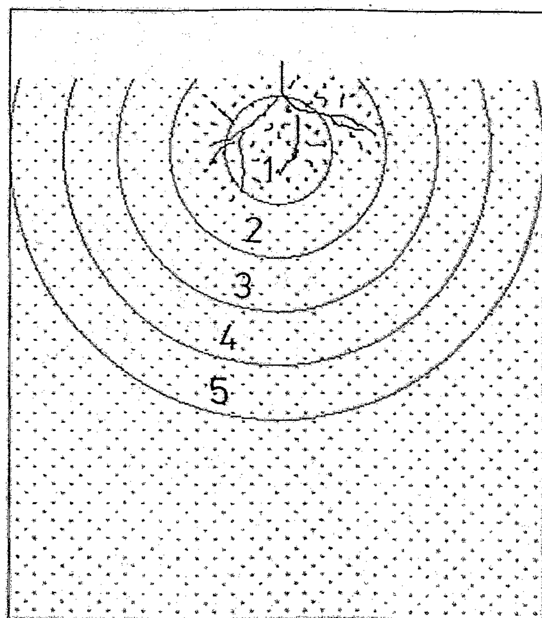

Fig. 1: The cross section $y = \frac{15}{2}a_o$ of the simulation cell consisting of 27000 Si atoms ($15a_o \times 15a_o \times 15a_o$). All atoms in the lattice plane at $y = \frac{15}{2}a_o$ as well as in one lattice plane above and in one lattice plane beneath this lattice plane are shown. The traces of the incident Si atom (500 eV) and the Si atoms of these 3 layers illustrate the evolution of the collision cascade (up to 0.1 ps). A sphere of the collision cascade ($R = 1.5a_o$, $z = 2a_o$) and shells surrounding this sphere are defined for the calculation of local temperatures.

Fig. 1 shows a cross section of the simulation cell. The traces of the incident Si ion (500 eV) and all recoils illustrate the evolution of a particular collision cascade up to about 100 fs after the ion impact. The initial temperature is $T = 0\ K$.

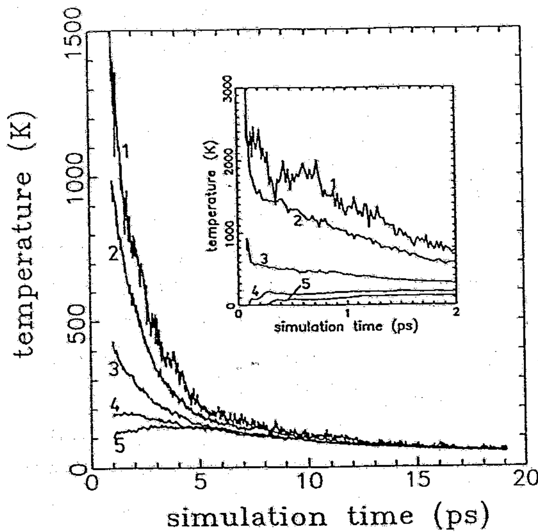

Fig. 2: Temperature of the regions defined in Fig. 1 versus time for the particular collision cascade of Fig. 1. 10^{-13} to 2×10^{-13} s after the ion impact thermalization is obtained, i.e. a local temperature can be defined. There are strong temperature fluctuations in region 1 due to the small number of atoms (less than 200). The temperature of the inner sphere remains for nearly 1 ps above the melting temperature (ca. 1680 K). The longtime behaviour of the temperature corresponds to classical diffusion.

Fig. 2 shows the temperature in the regions defined by Fig. 1 for the particular collision cascade of Fig. 1. It should be noticed that the temperature in the inner sphere remains above the melting temperature for nearly 1 ps.

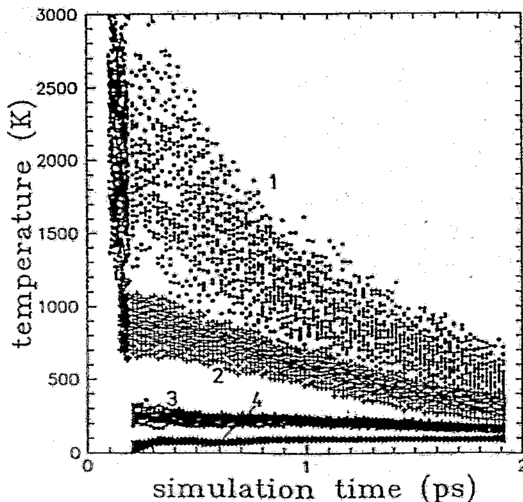

Fig. 3: Plot of the statistics of temperatures for many collision cascades. The temperatures are calculated for the regions defined in Fig. 1. The calculation has been carried out for 25 different collision cascades produced by Si ions of $E_i = 500\ eV$ with normal incident on the (100) surface, where the impact points were distributed over an elementary cell.

The features of the collision cascades of different ions may be very different. For that reason, especially for the inner sphere different temperatures are expected even for the same ion energy. Fig. 3 represents such statistics for 25 ion trajectories. It can be seen that for about 50 % of the collision cascades the temperature exceeds the melting temperature for some tenth of a picosecond. Our results should be a reliable input for thermal spike models.

References

[1] K.-H. Heinig and D. Stock, to appear in Nucl. Instr. and Meth.;
D. Stock and K.-H. Heinig, MRS Fall Meeting, Symposium A Beam-Solid Interactions: Fundamentals & Applications, Boston, USA, Nov. 30 - Dec. 4, 1992, contr. paper A7.11.

[2] K.-H. Heinig and D. Janssen, this annual report.

Compression Waves Induced in Si by Low-Energy Ions – a Molecular Dynamics Simulation

K.-H. Heinig and D. Stock*
*Friedrich Schiller University, Faculty of Physics and Astronomy,
Max-Wien-Platz 1, O-6900 Jena

Some years ago Carter discussed the possibility of ion impact induced shock processes in solids [1] which are important for the sputtering yield. Using a semi quantitative model his results are more or less on a qualitative level. We study the slowing down of low-energy ions in silicon by full molecular dynamics (MD) calculations which is at present the most realistic method. Collective phenomena resulting from a collision cascade, e. g. shock waves and/or compression waves, are directly accessible by this first principle method.

The equations to be solved and the potential taken into account are described in refs. [2,3]. Our simulation cell is the same as in ref. [4]. Fig. 1 illustrates a typical compression wave found by our MD calculation. The simulation cell is viewed from the y- and x-direction (left and right part of Fig. 1, respectively). If we define that the center of the collision cascade is the origin of a co-ordinate system, then Fig. 1a shows the radial shifts of the atom positions with respect to their positions before the ion impact. The 'radius of the atoms' in Fig. 1a represents the amount of the radial shift, full circles mean atoms shifted away from the center, empty circles are radial shifts towards the center. The shell of shifted atoms (Fig. 1a) is surrounded by a shell of compression (Fig. 1b, smaller interatomar distances). The wave moves with the longitudinal velocity of sound ($v_l^{<100>} = 8400\ ms^{-1}$).

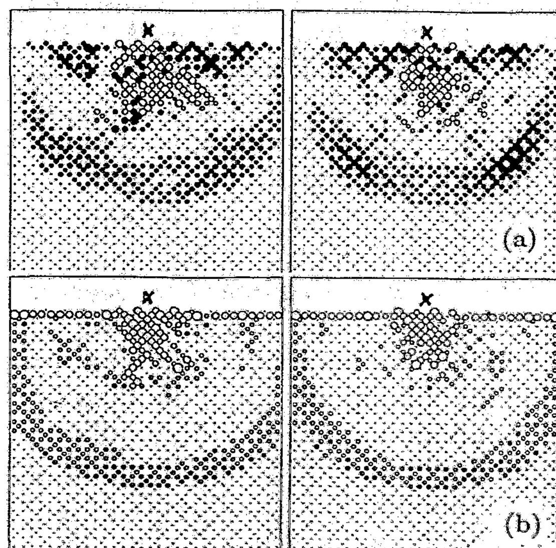

Fig. 1: Snapshot at $t = 0.5\ ps$ of a compression wave produced by a 500 eV Si ion (initial position marked by a cross) incident on a (100) Si surface. (a) Radial shifts of the atom positions. (b) Deviation of the local mean interatomic distance from the equilibrium value.

References

[1] C. Carter, Radiation Effects Letters 43, 193 (1979); ib. 50, 105 (1980).
[2] K.-H. Heinig and D. Stock, to appear in Nucl. Instr. and Meth.; D. Stock and K.-H. Heinig, MRS Fall Meeting, Symposium A *Beam-Solid Interactions: Fundamentals & Applications*, Boston, USA, Nov. 30 - Dec. 4, 1992, contr. paper A7.11.
[3] K.-H. Heinig and D. Janssen, this annual report.
[4] K.-H. Heinig and D. Stock, this annual report.

Molecular Dynamics (MD) Simulations of GRID Experiments

K.-H. Heinig and D. Janssen*
*Institute of Nuclear and Hadronic Physics

Full MD calculations are the most realistic method to simulate the slowing down of low-energy ions in solids through atom-atom collisions [1]. The basic idea of the MD calculations is that the positions and velocities of both the low-energy ion and the target atoms are calculated by numerical integration of Newton's equations of motion

$$\frac{d\mathbf{r}_i}{dt} = \mathbf{v}_i, \qquad \frac{d(m_i\mathbf{v}_i)}{dt} = -\sum_{j\neq i}\left(\frac{dV(r)}{dr}\right)_{r=r_{ij}} \frac{\mathbf{r}_{ij}}{r_{ij}}, \tag{1}$$

where $\mathbf{r}_i$, $\mathbf{v}_i$ and m_i are the position, velocity and mass of atom i, respectively, and $V(r)$ is the interatomic two-body potential. In view of the fact that the Si crystal consists of atoms held in place by strong and directional bonds, in our case eqs. (1) become more complicated due to the use of pair and triplet potentials [2] for $V < 0\ eV$. At $V > 50\ eV$ the strong chemical bonds become unimportant, here we use an universal nuclear interaction potential [3]. The two regions are connected by a spline of fourth order. The equations of motion (1) were integrated in time using the Verlet algorithm in the velocity form. In ref. [1] we used this method to investigate ion implantation phenomena.

Very recently, we applied our MD method to simulate γ-lines of recoiling excited nuclei [4], which are measured by the γ-ray induced Doppler-broadening (GRID) method [5]. In the GRID method a recoiling excited nucleus is produced by the emission of a primary γ-ray of energy E_p from the compound nucleus after thermal neutron capture. When the recoiling nucleus decays further by the emission of the secondary γ-ray of energy E_γ, the measured Doppler shift ΔE_γ of E_γ depends on the velocity $\mathrm{v}(t)$ of the recoiling atom at the time t after the emission of E_p and the angle θ under which E_γ is observed relative to the recoil direction, i. e. $\Delta E_\gamma = E_\gamma \beta(t) \cos\theta$, where $\beta(t) = v(t)/c$ and c is the velocity of light.

The Doppler broadened γ-line contains information on the lifetime of the nuclear state and/or the stopping power of the recoiling atom in the solid. However, in general it is not possible to reproduce the measured γ-profile and to extract the lifetime of the nuclear state without a theoretical description of the collisions between the recoiling and the lattice atoms. Several procedures of theoretical analysis are currently applied to the GRID data, the most appropriate MD method has been employed for the first time by Kuronen [6]. Improved lifetimes of excited nuclear states and first experimental information on the interatomic interaction potential in the energy range of a few 100 eV have been obtained.

Up to now it has been assumed [6] that, as the direction of the primary γ-ray is isotropically distributed, θ is not fixed by the experiment and thus does not enter explicitly. Then one obtains for the Doppler-broadened line shape

$$I(\Delta E_\gamma) = \int_0^{t_{max}} \mathrm{d}t\ \mathrm{e}^{-t/\tau} \int_0^{v_{max}} \mathrm{d}v' \frac{f(v',t)}{v'}. \tag{2}$$

Here I is the intensity of secondary γ-rays with Doppler shift $\Delta E_\gamma = E_\gamma v/c$, $t_{\max}$ is the time up to which the simulation events are calculated, τ is the lifetime of the nuclear level under study, and $v_{\max}$ is the maximum velocity of the recoiling atom. The distribution function $f(v,t)$ of the absolute values of velocities is obtained from the MD simulations. In ref. [7], for polycrystalline titanium measured lineshapes are compared with lineshapes calculated with eq. (2). The smooth shapes of the line profile allow the fit of one quantity at best, in the actual case the lifetime of the nuclear state. If another interatomic interaction potential is taken for the MD simulation, the fit gives a modified lifetime. To fit both, lifetime and potential, for a transition a more structured lineshape or a series of lineshapes is necessary but not available by this procedure.

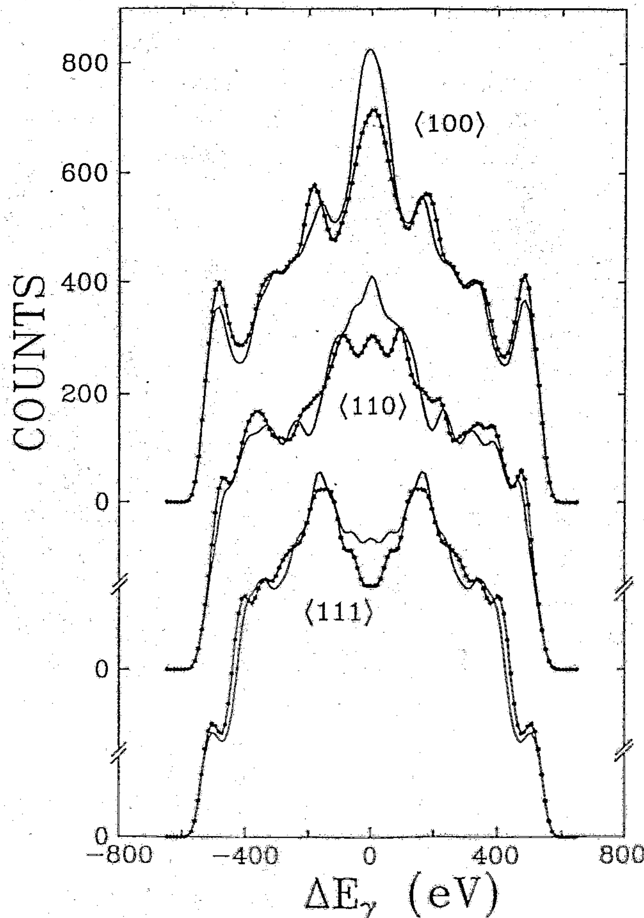

Fig. 1: Examples for Doppler-broadened lineshapes due to the slowing down of recoils in *monocrystalline* silicon. The Doppler-broadened lineshapes are predicted by our MD simulations for the secondary γ-decay with $E_\gamma = 2.43\ MeV$, $\tau = 10\ fs$, where the recoils are produced by the primary γ-decay with $E_p = 6.05\ MeV$ following the nuclear reaction $^{28}Si(n,\gamma)^{29}Si$. The structure in the lineshape reflects the dependence of the slowing down process of recoils on the recoil direction in the crystal. The temperature dependence is small, here we present results for $T = 0\ K$ only. With changing alignments between the spectrometer axis and the crystal orientations (denoted in the figure) the lineshape changes substantially. The universal potential (marked lines) and the Moliere potential (thin lines) result in different lineshapes which should be experimentally resolveable.

Recently, we predicted for the first time γ-lineshapes for single crystals [4]. Up to now no experiments have been carried out for single crystals [8]. We use

$$I(\Delta E_\gamma) = \frac{1}{\tau}\sum_i \int_0^\infty \mathrm{d}t\ \mathrm{e}^{-t/\tau}\delta(E - E_\gamma - \frac{\mathrm{v}_i(t)\mathrm{n}}{c}E_\gamma), \quad (3)$$

where $\Delta E_\gamma = E - E_\gamma$. Our more general formula (3) contains the direction of the spectrometer axis n (with respect to the crystal axis) and all velocity vectors $\mathrm{v}_i(t)$ of the recoiling atoms i. Using our MD code, we simulate for the nuclear reaction $^{28}Si(n,\gamma)\,^{29}Si$ the profile of the Doppler-broadened γ-line of the secondary γ-transition with $E_\gamma = 2.43\ MeV$ and $\tau = 10\ fs$, where the Doppler-broadening comes from the primary γ-decay with $E_\mathrm{p} = 6.05\ MeV$.
In our MD simulations, the recoil atoms start from a lattice point into 3000 randomly distributed directions. The slowing down of the recoils is calculated using a finite cell of 960 atoms with periodical boundary conditions. The crystal structure is of diamond type. After each time step t_j at the Doppler shift $\Delta E_\gamma = \mathrm{v_i}(t_\mathrm{j})\mathrm{n}/c$ the value $P_\mathrm{j} = \mathrm{e}^{-t_\mathrm{j}/\tau}$ has been added to the intensity $I(\Delta E_\gamma)$. This procedure is equivalent to the calculation of $I(\Delta E_\gamma)$ corresponding to eq. (3).
Our theoretical prediction proves that considerably improved GRID experiments can be carried out with monocrystalline samples. Then different crystal alignments lead to different lineshapes with a pronounced structure (see Fig. 1). These lineshapes contain sufficient information to fit several quantities (e. g. lifetimes, potential) in one experiment. Fig. 1 demonstrates that even small differences in potentials should be measureable in the energy region $50\ eV < E_\mathrm{I} < 1\ keV$, where other methods fail to give good results. After the reconstruction of the research reactor at the ILL Grenoble our proposed experiments will be carried out [8]. The new ultra-high-resolution gamma spectrometer GAMS5 should even allow to determine the location of impurities in a host crystal.
This work was supported in part by the Bundesministerium für Forschung und Technologie under Grant No. 211-5291-03-HE3ROS.

References

[1] K.-H. Heinig and D. Stock, to appear in Nucl. Instr. and Meth.;
D. Stock and K.-H. Heinig, MRS Fall Meeting, Symposium A *Beam-Solid Interactions: Fundamentals & Applications*, Boston, USA, Nov. 30 - Dec. 4, 1992, contr. paper A7.11.
[2] F.H. Stillinger and T.A. Weber, Phys. Rev. B31, 5262 (1985).
[3] J.F. Ziegler, J.P. Biersack and U. Littmark, *The Stopping and Range of Ions in Solids*, (Pergamon Press, New York,1985).
[4] K.-H. Heinig and D. Janssen, in: *Workshop on Applications of High Resolution Gamma Spectroscopy in Studies of Atomic Collisions and Nuclear Lifetimes*, Grenoble Oct 5-7, 1992, eds. H.G. Börner, J. Jolie, M. Pendlebury, and S. Ulbig , Inv. contr.; to appear in Phys. Letters.
[5] H.G. Börner, J. Jolie, F. Hoyler, S.J. Robinson, M.S. Dewey, G.L. Green, E.G. Kessler, and R.D. Deslattes, Phys. Lett. B215, 45 (1988);
J. Jolie, S. Ulbig, H.G. Börner, K.P. Lieb, S.J. Robinson, P. Schillebeeckx, E.G. Kessler, M.S. Dewey, and G.L. Greene, Europhys. Lett. **10**, 231 (1989).
[6] A. Kuronen, J. Phys. G3, 11 (1991);
A. Kuronen, J. Keinonen, H.G. Börner, J. Jolie, and S. Ulbig, Nucl. Physics **A549**, 59 (1992).
[7] A. Kuronen, J. Phys. Condens. Matter **3**, 1363 (1991).
[8] H.G. Börner, private communication.

The Diffractometer of the RCR at the Řež Reactor

A. Mücklich, M. Betzl, P. Reichel, and W. Boede

After the final decision for shutting down the Rossendorf Research Reactor (RFR) a neutron diffractometer was installed at the Řež Reactor (RR) by the Research Center Rossendorf (RCR). The RR providing a sufficient thermal neutron flux of $5\times10^8 cm^{-2}s^{-1}$ at its channel is of the same type as the RFR and allows therefore the use of existing parts of diffractometers situated at RFR before.

It was the intention to set up a conventional neutron powder diffractometer containing attachements for a quantitative texture analysis. Moreover measurements of geological specimens which cause a large secondary beam should be possible. The diffractometer TEXDIFFK9 was moved to RR after performing a complete upgrading of the installations. This includes the conversion to new electronics for registration and controlling (PC 386SX) the software of which was elaborated in the months before. Moreover TEXDIFFK9 was equipped with an Eulerian cradle of the large HUBER type with ∅ 400 mm and a gap of 127 mm. The step motors used allow rotations with a reproducibility better than 2". Immediately after transport the building up of the equipment at horizontal channel HK6 of the RR was started. Here the very time-consuming erection of the completely new designed shielding walls consisting of boron-polyethylen blocks has to be emphasized. For generating a useful initial neutron beam divergency ($\approx 1°$) three collimators were installed into the closing system of HK6 (∅ 60 mm). After that the mechanical and the optical adjustment of the basic device was carried out. Hence it followed a limitation of the scattering angle at $2\Theta_{max} = 114°$, where the detector and the monochromator shieldings touch one another.

Simultaneously with the beginning of the first cycle after the reactor rest in the summer period, we were ready to start the neutronographic adjustment. By means of Ni powder standard a wavelength $\lambda_{Zn} = 0.144$ nm could be determined for the (002)-lattice plane of a Zn monochromator. Via $Q = 4\pi\sin\Theta/\lambda$ it corresponds to $Q_{max} \approx 73\ nm^{-1}$. In Table 1 spacings, wavelengths and Q-values are given which become relevant if other monochromator materials as pyrolytic graphite (PG) or copper are used.

	d/nm	λ/nm	Q_{max}/nm^{-1}
Zn(002)	0.2474	0.144	73
PG(002)	0.3354	0.195	54
Cu(111)	0.2087	0.122	86

Taking into account the mosaic spread of the monochromators being available and the divergency of the collimator ($\Delta 2\Theta = 28'$) in front the ^3He detector (∅ 93 mm) a mean resolution $\Delta d/d \leq 2.8\times10^{-2}$ was achieved which is relatively low in favour of a good luminosity. The background counting rate is sufficiently small (0.1 cps). A top view of the whole arrangement at HK6 is given in Fig. 1. It demonstrates that the dosis rates, measured at points indicated as that of the lowest and the highest values outside of the cabin, are very low for both neutron and γ-radiation.

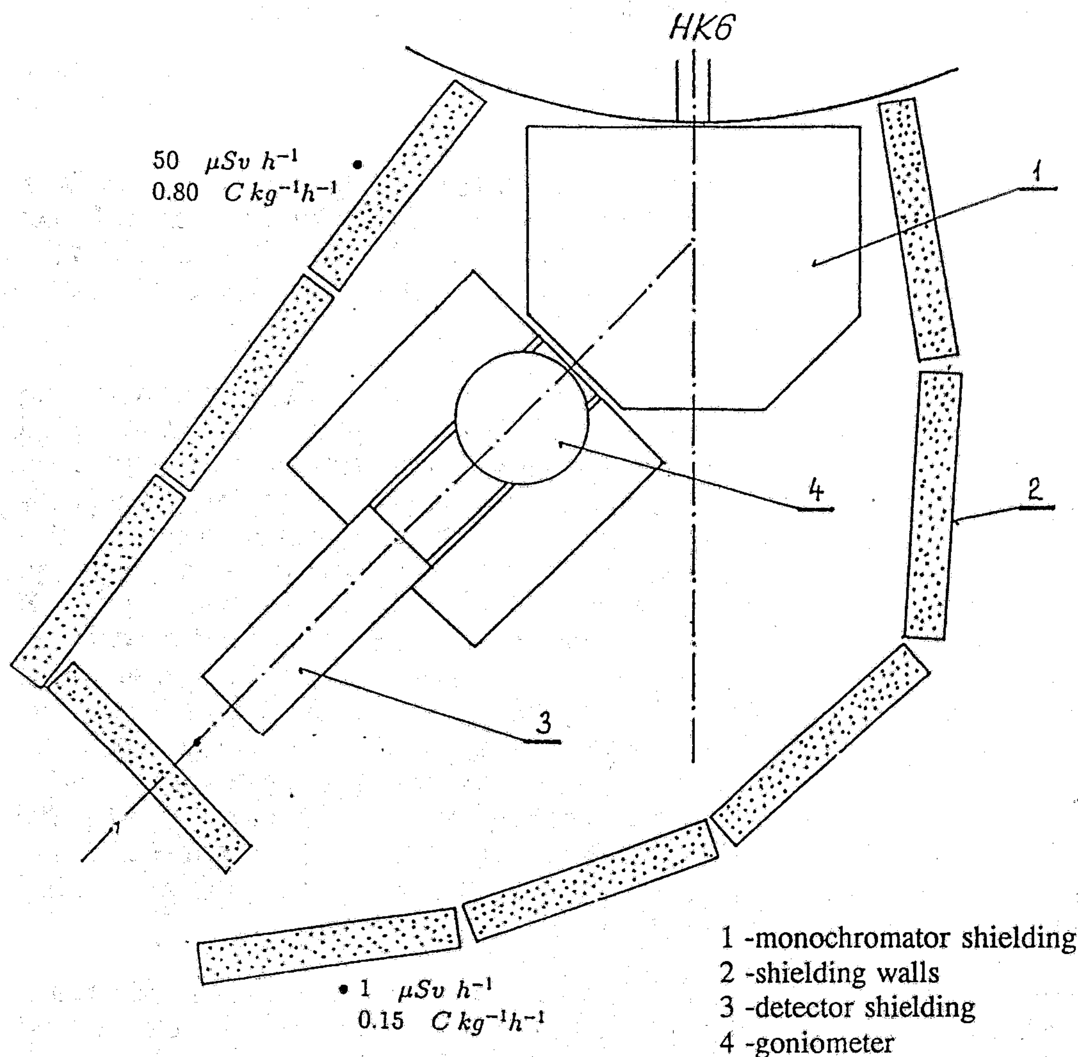

Fig. 1: Top view of the diffractometer at HK6 of RR

Disregarding a break of a week in December caused by an error in the controlling system the running of the diffractometer could be achieved for all reactor cycles in the last quarter of 1992. The distribution of measuring time was planned in a multi-user regime in which the RCR, the TU Mining Academy Freiberg, and the Geological Research Centre Potsdam were invoIed. Consequently, beside methodological problems the textures of both metallic (Fe sheets, brass tubes) and geological (Halite) samples were investigated.

The diffractometer at the RR is already a fully established equipment the using of which is open for German and Czech scientists. Thus, one of the new users starting in spring 1993 will be the TU Chemnitz the activities of whom will be focussed on the structure of molten alloys. For 1993 the intention is to convert the detection to a position-sensitive system of the JULIOS type. Moreover a PC 386DX exclusively for data evaluation will be installed.

Neutron Diffraction Analysis of Substructures in Polycrystalline Materials

P.Klimanek*, T.Kschidock*, A.Mücklich, P.Lukas**, P.Mikula**, M.Vrana**
*Department of Materials Science, TU Mining Academy Freiberg/Sa., P.O.Box 47, DO-9200 Freiberg/Sa., FRG
**Nuclear Physics Institute of the Czech Academy of Science, CR-250 68 Rez n.Prague, CR

Introduction

The mechanical properties of a polycrystalline material strongly depend on its substructure. An integrated substructure analysis (i.e. analysis of lattice disorder of the 2nd kind due to structure defects as dislocations, stacking faults etc.) is often performed by evaluation of the line broadening of X-ray diffraction peaks ([1,2,3] for instance). In this connection two difficulties have to be taken into account :

- the limited number of grains contributing to the observable line shape and broadening and, consequently, to the orientation averaging over the lattice disorder of the individual crystallites, and
- the strong decrease of the X-ray scattering intensities at higher diffraction angles which significantly complicates the detection of weak physical line broadening (or small level of lattice disorder, respectively).

Both problems can be avoided by use of elastic neutron scattering. It allows averaging over a large number of crystallites ,and second, the atomic scattering power of the sample material is, as a rule, independent of the scattering angle. Therefore shape analysis of physically broadened neutron diffraction peaks should be an attractive supplement of the procedure of integrated substructure investigation. Of course, because of the instrumental line broadening of the reflection due to non-ideal diffraction conditions, application of high-resolution neutron diffractometry is necessary for this purpose.

Experimental Procedures

Equipment: The present work was performed at the high-resolution triple axis neutron spectrometer TKSN 400 of the Nuclear Physics Institut Rez (n. Prague,[7]).
Beam monochromatisation and analysing uses bent Si(220)- crystals. The registration mode was θ-2θ-step scanning with a step size $\Delta\theta = 0.018°$.

Sample material: For the experiments technically pure copper and a X8CrNiTi18.7 steel were chosen. After annealing both materials were plastically deformed by compression at room temperature (ε_{Cu}-82%, $\varepsilon_{Mart.}$-75%). During the deformation the steel is partially transformed into cubic martensite.
Material of standards were annealed at 750°C/20min (Copper) and 900°C/20min (α-iron) to get the required structure.

Experimental Results and Conclusions

In Fig.1 the (110)-diffraction line shapes as obtained by X-ray and neutron scattering are compared. The graph demonstrates the equivalence of the data and the excellent resolution of the neutron spectrometer used.

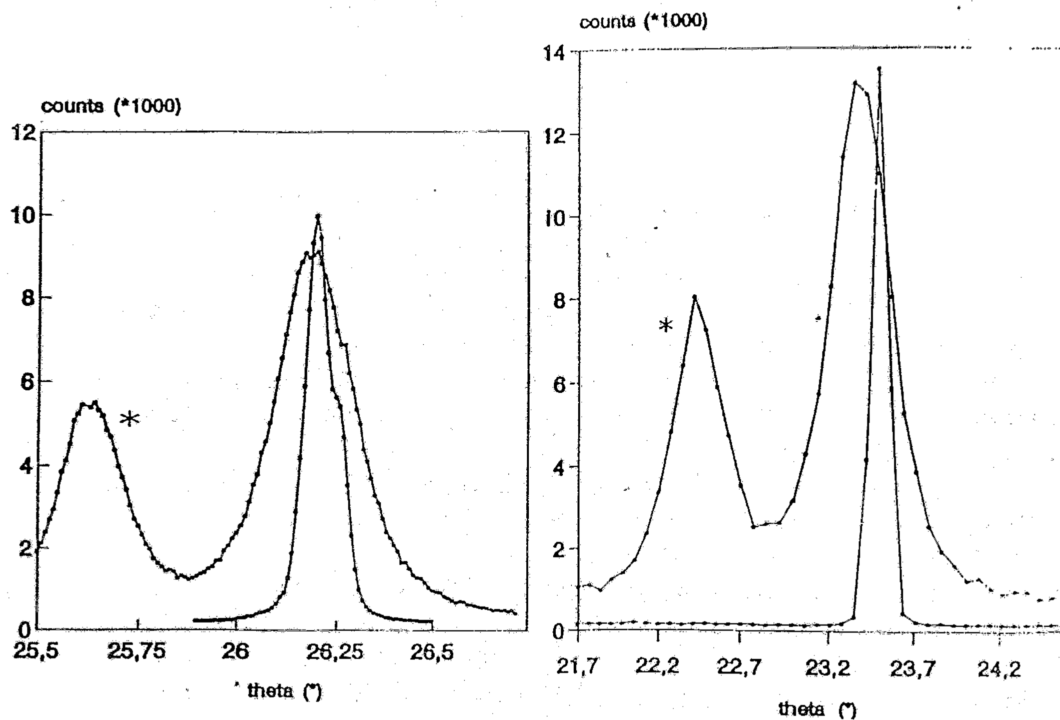

Fig.1: (110) diffraction line profiles of martensite as measured with X-rays (a) and neutrons (b)

Table 1: Structure parameters of copper and martensite

	Copper(111)	Martensite(110)	
	Neutron	X-Ray	Neutron
	diffraction		
Particle size T [nm]	17,2	9	13
Strain $<\varepsilon^2>^{1/2}*10^3$	5,8	4,5	1,9
Dislocation parameter B $*10^{-11}$ [cm^{-2}]	6,3	5,6	2,3

The substructure parameters calculated from Warren- Averbach and Krivoglaz-Wilkens plots of the Fourier coeffizients [4,5,6] are given in Table 1. Taking into account that the step size of the neutron diffraction experiment must yet be optimized and that the number of scattering crystallites is very different in X-ray and neutron diffraction , the agreement of the data is satisfactory. A good correspondenc to substructure parameters determined from X-ray diffraction is also given in the case of copper.

* * *

The present work is supported by the Federal Ministery for Research and Technology (BMFT) of the FRG.

References

[1] Warren, B.E.: Progr.Metal. Phys., 9, 147 (1969)
[2] Klimanek, P.: Freiberger Forschungsheft B 132, 33-65 (1968)
[3] Delhez,R.; de Keijser, Th.H.; Mittemeijer, E.J.: Fresenius Z. Phys. Chem., 312, 1 (1982)
[4] Krivoglaz, M.A.: -Theory of X-ray and thermal neutron scattering by real crystals (in russ.), Moscow 1967
-Theory of X-ray and neutron diffraction by imperfect cystals (in russ.), Kiev 1983
[5] Wilkens, M.:-phys. stat.sol.(a), 2, 359 (1970)
-in: Fundamental Aspects of Dislocation Theory (Editors: J.A.Simmons et al.), Vol. II, 1195, N.S.B. Special Publ. 317, Washington 1970
-Kristall & Technik, 11, 1159 (1976)
[6] Klimanek, P.:Freiberger Forschungsheft B 265, 76-94 (1988)
in:X-ray and Neutron Structure Analysis in Material Research (Ed. J.Hasek), Plenum Press, New York 1989, 125-137
in: EPDIC 1-European Powder Diffraction(Ed. R. Delhez, E.J. Mittemeijer), Mat.Sci.Forum 79-82, Pt.1, (1991)
[7] Kulda, P.; Mikula, P.; Lukas, P.; Kocsis, M.: Proc. Int.Conf. on Neutron Scattering, Oxford, Physika B (1991)

Study of Hardening of Portland Cement Paste by Small-Angle Neutron Scattering

F. Eichhorn, F. Häußler*, and H. Baumbach**

*Institute for Nondestructive Testing Saarbrücken (FhG), at present: Frank Laboratory for Neutron Physics of the Joint Institute for Nuclear Research Dubna, Russia

**Institute for Nondestructive Testing Saarbrücken (FhG)

Building materials like hardened (hydrated) cement or concrete are heterogeneous. Especially for such substances their useful properties (as strength, porosity, thermal insulation, permeability for gases and liquids) are determined by the structure within and between their components. The development of the material structure during the hydration process depends on the starting values (composition of the mixture, for instance the mass ratio of water to cement or the content of additives) and on the external physical parameters and technological conditions of the process (e. g. temperature, humidity, vibration).

To observe the mesoscopic structures in an averaged way the method of small-angle neutron scattering (SANS) was used with its possibility for contrast variation between different phases of the hydrating material. Hydration with H_2O, D_2O or a mixture of them, respectively, gives various values of the scattering length density.

Here results of an ordinary Portland cement (type 1/40 A) are presented which are obtained by the MURN device at the IBR-2 pulsed reactor of the JINR Dubna. SANS curves are measured in the scattering vector range between Q_{min} = 0.00863 $Å^{-1}$ and Q_{max} = 0.147 $Å^{-1}$ ($Q = 4\pi\sin\Theta/\lambda$, 2Θ - scattering angle). According to the sampling theorem [1] reliable results from this measuring conditions can be obtained for spherical particles with gyration radii between 8 and 141 Å.

For the present investigation the samples of hardened cement paste are prepared from ordinary Portland cement (OPC) and heavy water (D_2O) with a water-cement ratio of 0.38. For these preparation conditions the most abundant hydrated cement phases $C_3S_2 \cdot 2.5w$ (content 45 %), $Ca(OH)_2$ (22 %) and $C_3A \cdot CaSO_4 \cdot 12w$ (17 %) give the maximum contrast with the pore system (C = CaO, S = SiO_2 , A = Al_2O_3 , and w = water) [2] . The thicknesses of the specimens used were 0.50 mm, 1.05 mm, and 1.70 mm. The Figure 1 shows the measured scattering cross sections for the specimen of 0.5 mm thickness.

Assuming a logarithmic normal distribution for the size (geometric radius R) of spherical particles (pores or grains of different phases)

$$N(R) = N_g / (\sqrt{2\pi}\, p\, R) * \exp\{ - [\ln(R/R_o)/p]^2/2\}$$

the most probable radius R_o (centre of the distribution) and the dispersion of that distribution (p ~ FWHM) are given in the Table 1.

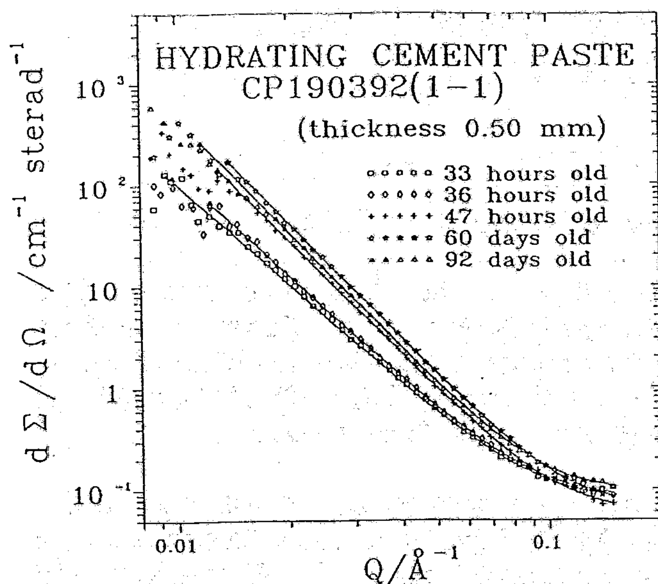

Fig.1: Small-angle scattering cross section of a hardening paste of ordinary Portland cement. The curve parameter is the time after the beginning of the hydration

Tab. 1: Parameters (the most probable radius R_o and the FWHM) of a logarithmic normal distribution for spherical particles in dependence on the hydration time of a Portland cement paste

Hydration time /d	R_o /Å	FWHM /Å
1	33 ± 1	31 ± 1
60	28 ± 5	43 ± 2
92	32 ± 4	45 ± 1

The results show that the mean particle size reaches its final value already in the early stage of hydration whereas the dispersion of the particle size increases during a longer period.

Analyzing the scattering cross section at higher values of Q a deviation from the Porod-law (valid for compact particles with sharp boundaries) is observed. This may be caused by a fractal-like surface or volume structure [3] . To study this problem further investigations are in preparation.

References

[1] Th. Gerber, P. W. Schmidt, J. Appl. Cryst. **16**, 581 (1983)
[2] A. J. Allen, C. G. Windsor, V. S. Rainey, D. Pearson, D. D. Double, and N. McN. Alford, J. Phys. D**15**, 1817 (1982)
[3] A. J. Allen, J. Appl. Cryst. **24**, 624 (1991)

Studies of $Sr_xBa_{1-x}Nb_2O_6$ Mixed Crystals by Neutron Diffraction at Temperatures between 15 K and 293 K

F. Prokert and B. N. Savenko*

*Lab. of Neutron Physics, Joint Institute of Nuclear Research, Dubna, Russia

At the time-of-flight (TOF) spectrometer DN-2, installed at the pulsed reactor IBR-2 in Dubna, $Sr_xBa_{1-x}Nb_2O_6$ mixed single crystals (SBN-100x) of different compositions ($0.50 \leq x \leq 0.75$) were investigated in a temperature range between 15 K and 293 K. The diffraction patterns are taken along the directions [001], [110], [111], and [100] from a sectorial area of the scattering plane (110) and (001), respectively.

The temperature dependence of the Bragg intensities as well as that of the lattice spacings show an anomalous behaviour. In Fig. 1 and Fig. 2 this is illustrated for the lattice parameters c and a. These data are collected from a SBN-70 crystal in TOF scans which were directed along the two basic directions. In extended regions anomalies of the thermal expansion are indicated by the slope of these curves.

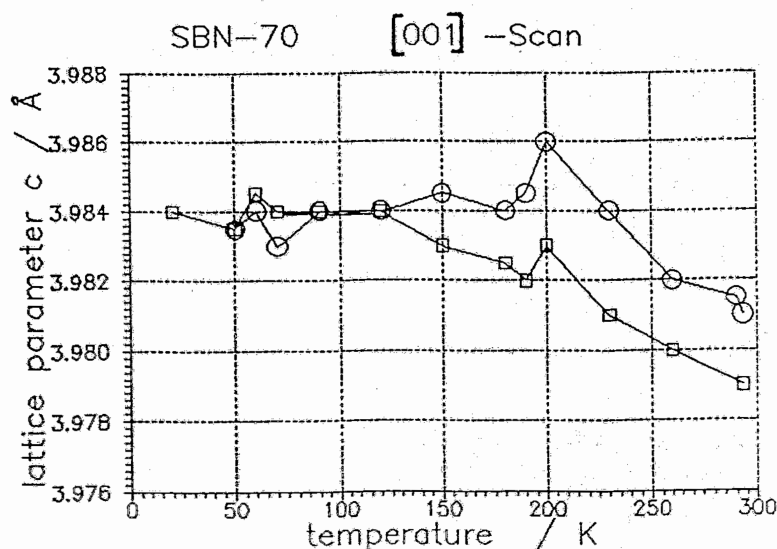

Fig.1: Temperature dependence of the lattice parameter c obtained from [001] scans on SBN-70
(□) - cooling from room temperature (RT) after a heating pretreatment (2h at about 600 K)
(O) - heating-up to RT

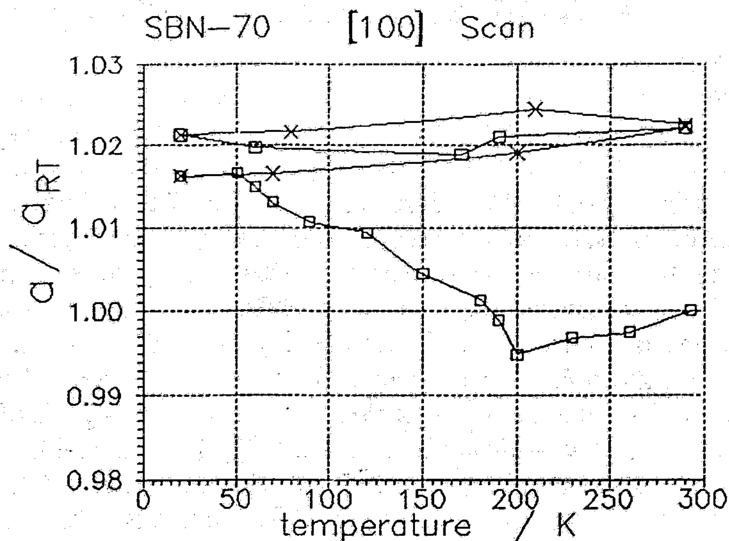

Fig. 2: Dependence of a relative lattice spacing (a/a_{RT}) on temperature obtained from [100] scans on SBN-70 at repeated cooling - heating cycle
(□) - cooling-down from RT (sample initially pretreated as described above)
(X) - heating-up to RT

Besides the known phase transition at about 190 K [1] and at about 60 K [2], which are clearly visible by anomalies at the most scan directions, in different scans another structural change occurs at about 250 K. In regions around these transitions the Bragg peak intensities as well as the lattice spacings show a large temperature hysteresis, and the widths of the Bragg peaks reach extremal values.

It is well-know, that the highly disordered relaxor material SBN at higher temperatures undergoes a diffuse ferroelectric phase transition [3]. Additionally, in the investigated lower temperature range an influence of electric field cooling on the diffraction pattern, checked at SBN-70 along [110], is found. Further, the investigated structural changes are sensitive to the thermal or electric sample history. These facts agree with speculations about field-induced orientation processes of 'frozen-in' polar clusters [3] and could fit into the picture of a change of polarization at low temperatures due to occurence of a [110]-component in the spontaneous polarization [2].

This work has been supported in part by the BMFT under registration number 03-GO3ROS-5.

References

[1] L. A. Bursill and Peng Ju Lin, Acta Cryst. B43, 49 (1987)
[2] Yuhuan Xu, Zhongrong Li, Wu Li, and Hong Wang, Ferroelectrics 108, 253 (1990)
[3] B. N. Savenko, D. Sangaa, F. Prokert, Ferroelectrics 107, 207 (1990)

The Neutron Time-of-Flight Diffractometer NSHR at IBR-2 in Dubna

J. Heinitz, K. Ullemeyer, and K. Walther

In order to improve technological processes or the properties of materials one has to consider the real structure of the (polycrystalline) material like grain size, grain boundaries or grain orientation. In material science the investigation of the preferred orientation began more than 70 years ago and the engineers have accumulated a lot of experience to solve the most problems connected with the development of the texture during processing. In natural objects preferred orientation of its structural elements also occurs. For instance, at geological formations this oriented structure is looking like foliation, lamination, folding etc. Because these structures can have gigant sizes and can be seen by unweaponed eyes they are described qualitativly more than one century ago before the development of powerfull microscopes or X-ray diffractometers. The quantitative description of the dynamical processes within the lithosphere and of the development of the texture are delayed in comparison with the materials science. For the investigation of geological samples one has to overcome some difficulties:

- Most geological samples are coarse grained and inhomogeneous. The investigation of the texture requires the use of neutron diffraction.
- Because of the low crystal symmetry the diffraction patterns show many peaks which are often overlapped. A diffractometer with a high resolution is therefore necessary.

A neutron time-of-flight diffractometer has been set in operation at a long flight path (104.66 m) at the 7th beam of the pulsed reactor IBR-2 in Dubna, Russia. This Neutron Spectrometer with High Resolution (NSHR) is mainly used for texture investigations.

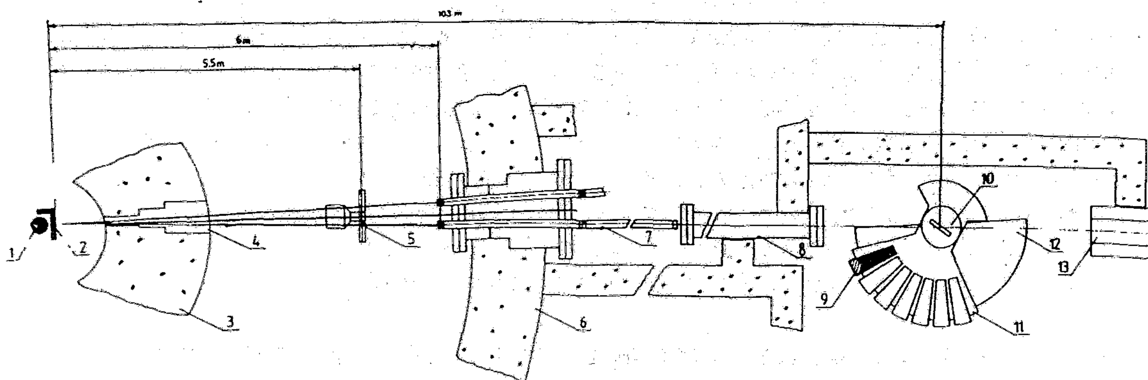

Fig 1.: The layout of the diffractometer NSHR at the beam 7A of the reactor IBR-2. (1) core of the reactor; (2) moderator; (3) reactor shield; (4) beam lock; (5) disk chopper; (6) biological shield; (7) first part of the neutron guide, Ar-filled; (8) second part of the neutron guide, vacuum; (9) detector shield; (10) texture goniometer; (11) platform, turnable; (12) base of the diffractometer; (13) beam stop.

The layout is shown in Fig. 1. After escaping the core (1) the fast neutrons are slowed down to thermal energies in a light-water moderator (2). An additional disk chopper (5) working synchronously with the reactor reduces the background between the reactor

pulses. The neutrons are guided by a Ni-coated straight neutron guide (7,8) to the sample fixed in a goniometer (10).

The diffractometer is equipped with a central sample desk carrying the goniometer or other sample environments like a furnace. Seven detectors in detector shields (9) are mounted on a moveable platform (11) achieving a wide range for the scattering angle 2θ from -10° to 190°. The minimal angular distance between two detectors is 14° in the 2θ-scale.

The cross section of the neutron beam is 50 x 170 mm^2 and the flux of thermal neutron is greater than 1 x 10^6 n $cm^{-2}s^{-1}$.

The diffractometer is remote controlled by a PC/AT via CAMAC-Interface. Step motors serve for a high precision in angle setting. The samples should have a spherical, cylindrical or cubic shape with a dimension of about 2.5 *cm*.

The good resolution and the relatively high neutron flux make the diffractometer very suitable for texture investigation of geological samples. Fig. 2 shows a diffraction pattern of quartz powder. The scattering angle 2θ was 160° and the measuring time 2

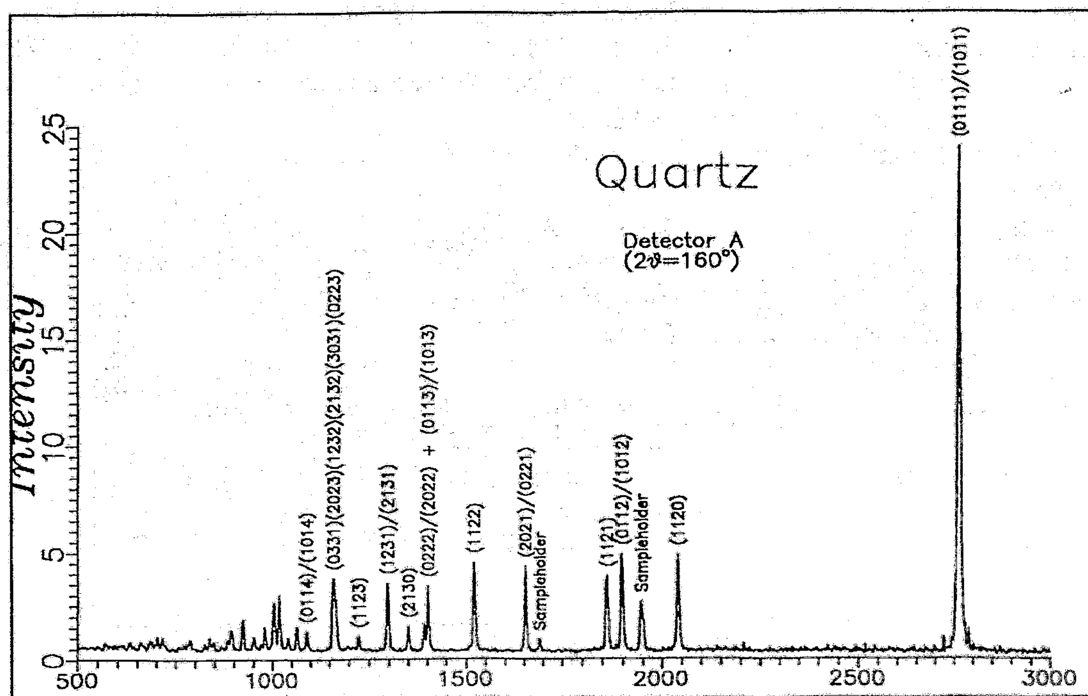

hours.

Fig. 2: Time-of-flight diffraction pattern of quartz powder. The figures on the abszissa refer to time channels (channel width 64 μs).

The further development of the sample environment includes the construction of two high-pressure cells. These cells are made of a special Ti-Zr-alloy with vanishing coherent cross section allowing measurements direct in the neutron beam without disturbing Bragg reflections of the construction material. The first cell should make

applicable an uniaxial load with forces of 10^5 N at temperature up to 1000 *K*. In the other cell in addition to the uniaxial load a hydrostatic pressure up to 15 *kbar* will be available, but the temperature exceeds only 600 *K*. The sample volume is about 5 cm^3. Several sensors are fixed at the sample in order to measure the strain rate, the sound velocities and the acoustic emission during the deformation.
Mainly these high-pressure devices will be constructed for the investigation of phase transition and the orientation relation between the α- and β- phases in quartz .

In order to minimize the experimental effort the detector arrangement should be changed that all detectors form a cone with the same scattering angle. At optimally chosen scattering angle the sample movement can be reduced to rotations about one axis only.

In Table 1 the characteristics of the diffractometer are compiled. A great spectrum of geological specimens was studied: samples from the super-deep drilling boreholes in Windisch-Eschenbach (Bavaria) and Kola (Russia), feldspars, micas, olivines, hornblendes, and other low-symmetric minerals.

Table 1: Characteristics of the diffractometer NSHR

Beam	Ni-coated straight neutron guide, total length 92 *m*
Beam cross section	50 x 170 mm^2
Chopper	at 5.50 *m* from the moderator
Moderator-sample distance	103.06 *m*
Mean flux of thermal neutrons at sample position	$\geq 1 \times 10^6$ n cm^{-2} s^{-1}
Wavelength	0.8 - 7.6 Å
Scattering angle	-10° - 190°
d-spacing (at 2θ = 60°)	0.8 - 7.6 Å
Resolution Δd/d, (2θ=160°, d>2Å)	0.4 %
Number of detectors	7
Type of detectors	^{3}He-counters, 1.7 *cm* ∅, 25 *cm* length, battery of 5 counters
Sample environment	texture goniometer, furnace (T≈ 1000 *K*) high temperature press (planned)
Experiment control	PC/AT with CAMAC-controller

7.25 GHz ECR Source for Highly Charged Ions

R. Hentschel and H. Tyrroff,
L. Friedrich*, E. Huttel* and L. Wiss*
*Kernforschungszentrum Karlsruhe GmbH (KfK)

A 7.25 GHz ECR ion source formerly delivering strong He^{2+} beams at KfK was modified and optimized to create well resolved beams of highly charged, slow ions to be used for atomic and surface physics research at Rossendorf [1].
The final setup of the magnetic elements generating longitudinal and radial field components, the R.F. feed, an additional electron emitter, and the ion extraction system are shown in Fig.1. In this figure the on axis longitudinal distribution of the magnetic flux density for a typical excitation current (820 A) is displayed, too [2].

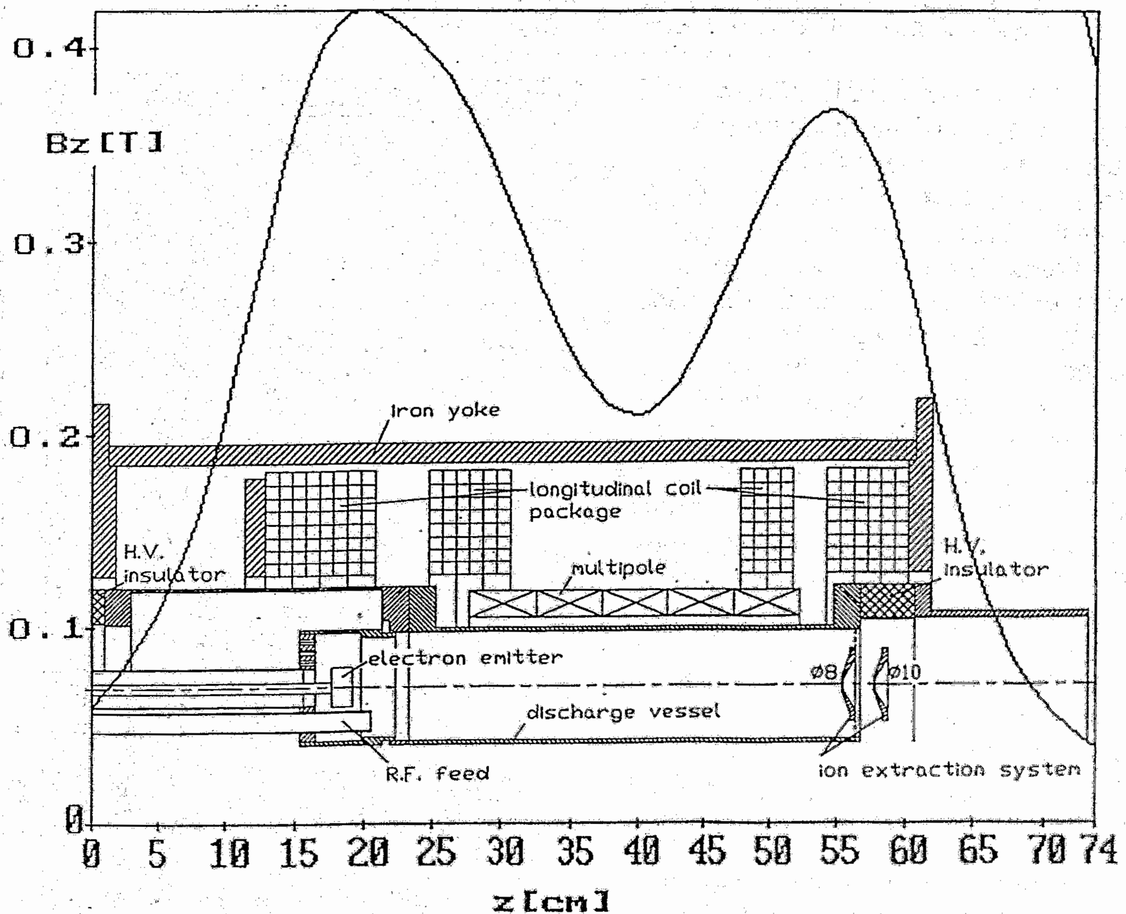

Fig. 1: Schematic layout of the 7.25 GHz ECR ion source and longitudinal magnetic flux density distribution.

Multipole cross section and magnetic flux density inside the multipole are demonstrated in Fig.2. Calculated and measured flux densities are in accordance.

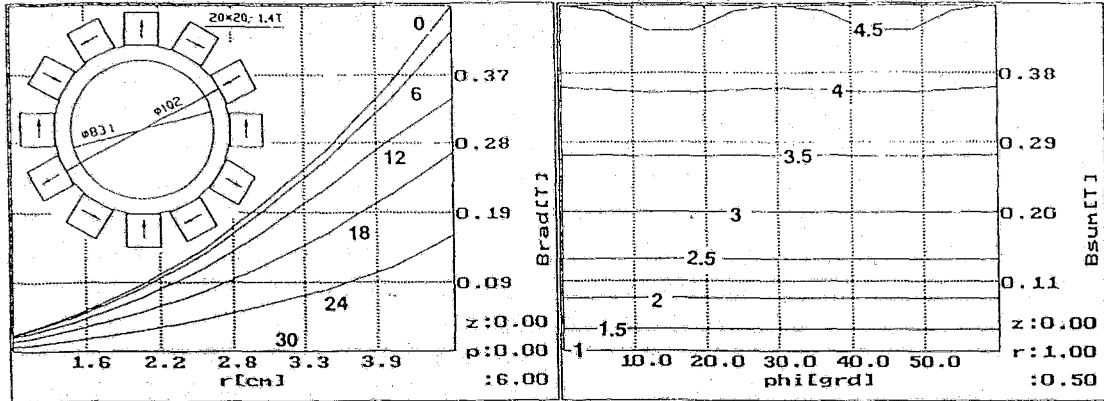

Fig. 2: Multipole cross section (smaller diameter corresponds to discharge vessel, pole size and remanence (NdFeB) indicated), radial component of flux density Brad(r) at azimuth = 0,6,12,..30° and total flux density Bsum(phi) at radii = 0.5,1,1.5,...4.5 cm [3].

At first, the positions of longitudinal field coil packages and magnetic shim inside the return yoke were optimized.
Further, the best position of the longitudinal field to the ion extraction system was found. The electron emitter consists of a cylindrical, insulated aluminium block, beeing charged to potentials between -5 and -10 V by the discharge itself. The best longitudinal position of the block was found experimentally. Using the emitter the ion current of highly charged nitrogen or argon ions was increased by at least a factor of two. Charge distribution spectra have been investigated by a stigmatic 90° analyzer magnet (bending radius 200 mm, magnification 1), image slit (width 10 mm) and Faraday cup.
Tab.1 and Fig.3 illustrate results of optimizing gas pressure, longitudinal field excitation, and R.F. power and gas mix-

Tab. 1: Charge states and corresponding ion currents ("?" means interference with mix gas).

Nitrogen & Helium		Argon &Oxygen	
Z(N)	I[eμA]	Z(Ar)	I[eμA]
1	7.3	6	2.1
2	10	7	4.3
3	17.3	8	10
4	26	9	7.8
5	23	10	?
6	5	11	1.6
7	?	12	0.4

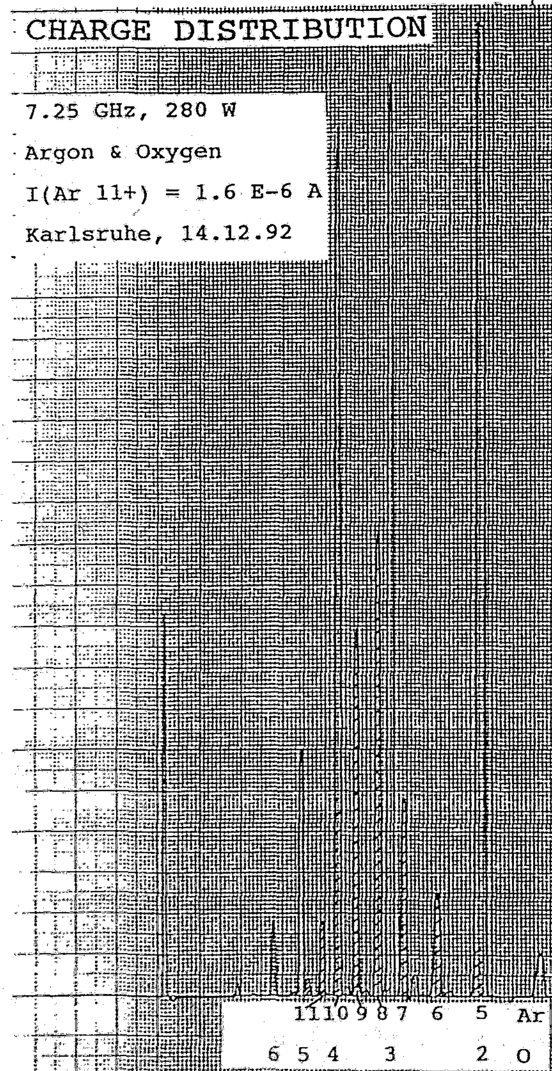

Fig. 3: Charge distribution spectrum for argon-oxygen mixture.
Source optimized for Ar^{11+}

ing for high charge states.
The source is installed at Rossendorf now. We intend to inflect Z/A resolved beams by a spherical condenser into the beam line of the Van de Graaff accelerator and to decelerate the ions on their way to the target station to kinetic energies of about 1/100 of the start value (Fig. 4). In this way the ion's kinetic and potential energy (potential energy represented by the charge state) at the target can be choosen independently .

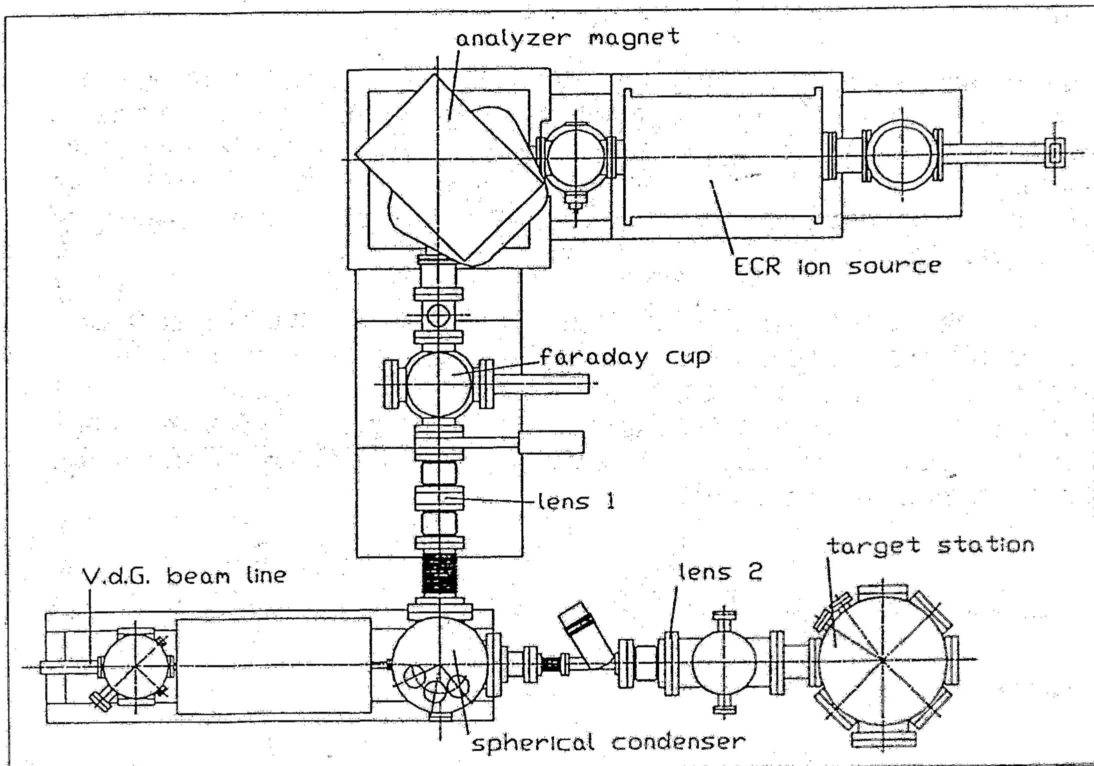

Fig. 4: Proposed experimental setup of ECR ion source and V.d.Graaf beam line at Rossendorf.

Acknowledgements

This work is supported by BMFT 06 DR 108 and Volkswagen-Stiftung I/66 139.
R.H. and H.T. thank C. Neelmeijer for stimulating discussions.

References

[1] R. Grötzschel, C. Neelmeijer, H. Tyrroff, H. Büttig and S. Preusche,
FZR 92-06, 65, Rossendorf (1992)
[2] H.T. thanks Michael Schlapp from Strahlenforschungszentrum U-Giessen for calculating Bz(z).
[3] calculated on the base of :Z.Q. Xie and T.A. Antaya, MSUCL-622, East Lansing, Sept. (1987)

Improvement of the Experimental Possibilities at the 2 MV Van de Graaff Accelerator

W. Bürger, M. Friedrich, R. Grötzschel, C. Neelmeijer, and S. Turuc

The 2 MV van de Graaff accelerator has been equipped since its starting 1963 with only one beam line. This does not allow any separation of experiments with high and ultrahigh vacuum.

During the out of operation period 1992 a switching magnet with +15° and -10° deflection was installed (see fig. 1 of tandetron status report). The RBS chamber is placed at the 10°-beam line and an ultrahigh vacuum equipment was built up at the 15°-beam line.
The belonging experiment chamber has been placed at our disposal from the group of Prof. Sitzmann from the Ludwig Maximilian University Munich.

Beside the high energy ions from the accelerator also highly charged ions from an ECR ion source will be injected in this chamber for surface investigations.
Both beam lines has been put into operation in February 1993.
The energy stabilizing system of the accelerator has been improved by installation of a new NMR device at the analyzing magnet made in the Institute of Nuclear Research Rez of the Czechoslovacian Academy of Sciences.

Status Report of the 3 MV Tandetron

M. Friedrich, S. Langer, S. Turuc, and E. Wieser

A contract for installation of a 3 MV tandetron (high current version) was made with High Voltage Engineering Europa B.V. at the end of 1991.
The tandetron will be applied mainly for high energy implantation. First experiments have been made already at the 5 MV tandem accelerator, but the beam current of this accelerator is not sufficient high for routine implantation.
Beside the implantation beam line a chamber for routine RBS-measurements and a nuclear microprobe will be built up.
The 3 MV tandetron will be installed in the second experimental room of the 5 MV tandem accelerator, the experiments will be arranged in a separate room (see fig. 1).

The direct vicinity to the other electrostatic accelerators allows the operation of the tandetron by the already existing accelerator staff. The chosen arrangement minimizes the staff and building expenditure.

The main activities in 1992 were directed to realize the installation requirements of the producer (cooling water, electric power, air-conditioning and room-preparation). These activities were finished in February 1993.

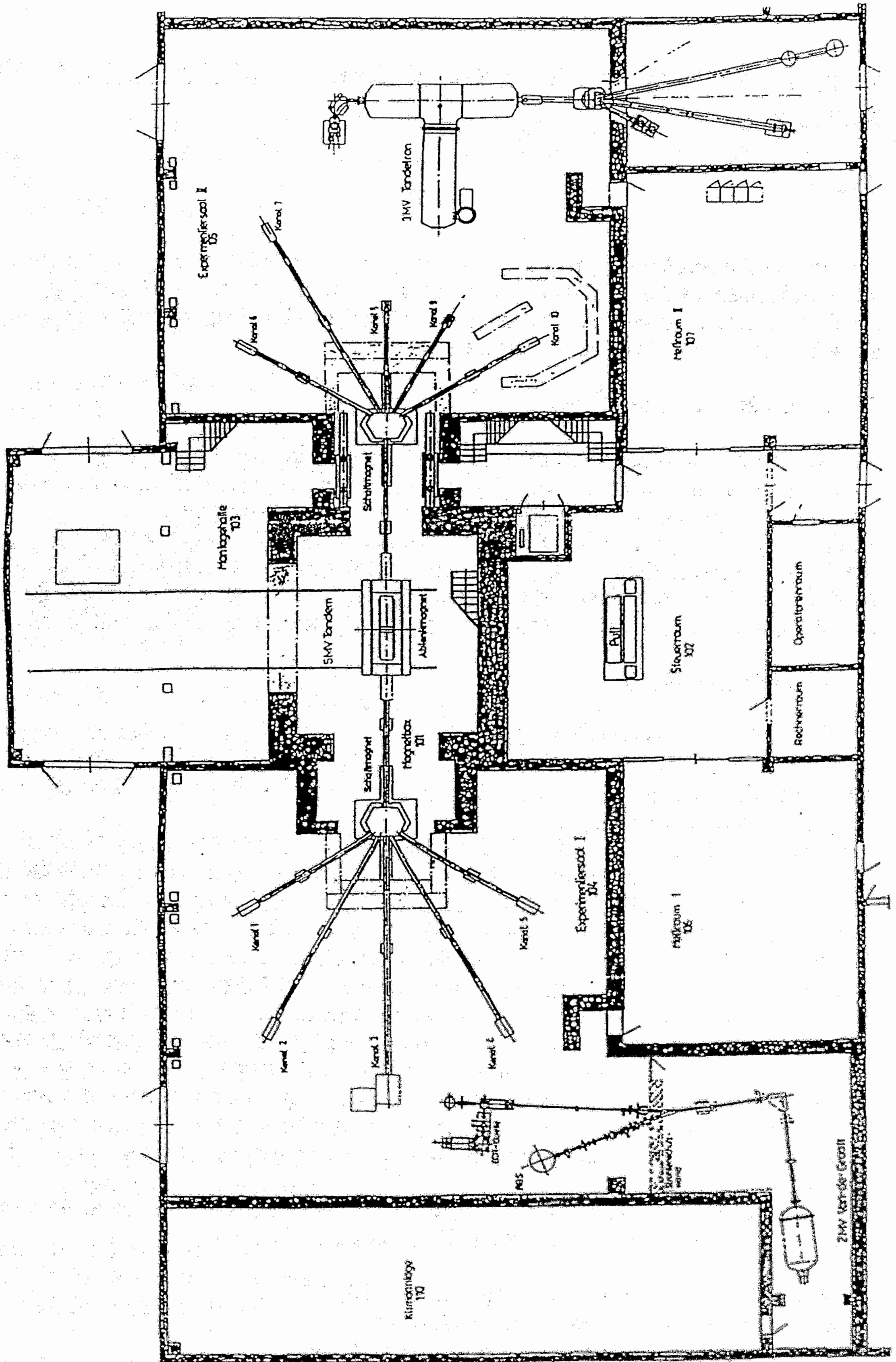

Fig. 1: Layout of the Rossendorf electrostatic accelerators

Developments for the Accelerator Control and Stabilizing Systems

W. Bürger

The time of the accelerators shut down was used for extended technical modernisation and development at the accelerators. This work was mainly directed on improving the accelerator control under the condition of reduced staff and on providing for the stepwise application of a modern computer system.

2 MV Van de Graaff accelerator

The vacuum control system has been improved in connection with the installation of new vacuum pumps. Activities at the charging current stabilizing system were directed on the increasing of the signal/noise ratio of the charging current measurement.
At the analyzing magnet a new NMR device was installed, which is of the same type as the NMR device at the tandem. The devices were developed and produced at the Institute of Nuclear Research Rez of the Czechoslovacian Academy of Sciences. They are microprocessor controlled and allow automatic magnet formation and signal finding.

5 MV Tandem accelerator

The installation of a new power supply system for the ion sources was started using a programable control unit SIMATIC S5 115 U (SIEMENS). For our sputter ion source these activities have made a large progress and the corresponding preparations for the duoplasmatron have been begun.
All ion optical elements now are equipped with high stabilized power supplies.
The transmission of analog control and measuring values across distances of more than a few meters is now done by using symmetric lines for improving the signal/noise ratio.
The energy stabilizing system was comprehensively revised. Investigations in the behaviour of linearized corona triode amplifiers with either current or voltage feedback were done but are not yet finished. Preliminarily it can be said that in dependence of the parameters of the accelerator (in particular in dependence of the relation of the acceleration voltage fluctuation caused by corona instabilities to that caused by the charging) either the current or the voltage feedback gives better stabilitiy and response.
The long-time stability of the pick-up amplifier has been improved on the base of modern integrated circuits. As slit amplifiers linear amplifiers with remote controlled gain are generally used now (contrary to the logarithmic amplifiers common in others laboratories).
We have begun to revise the generating voltmeter with respect to the conditions of accelerator mass spectrometry operation. The main goals of this work are

- simple adjustment of the mechanical part of the device
- high suppression of electromagnetic interferences
- high upper limiting frequency of the voltage measurement.

In the device conventional analog components are used in the processing of the sensor plate currents.

Publications

Brauer, G., Matz, W., Liszkay, L., Molnar, B., and Krause, R.,
Positron Annihilation and Mössbauer Studies of Neutron Irradiated Reactor Pressure Vessel Steels,
Materials Science Forum, **97-99**, 379 (1992)

Eichhorn, F., Podurets, K. M., Shilstein, S. Sh., and Soroko, Z. N.,
Surface X-Ray and Neutron Scattrering,
Springer Proceedings in Physics **61**, 251 (1992)

Erokhin, Yu.N., Grötzschel, R. Oktyabrsky, S.R., Roorda, S., Sinke, W., and Vyatkin, A.F.,
Mesotaxy by Ni diffusion into buried a-Si layer,
Mat. Sci. and Eng. B**12**,103 (1992)

Erzgräber, H. B., Zaunseil, P., Bugiel, E., Sorge, R., Tittelbach-Helmrich, K., Richter, F., Panknin, D., and Trapp, M.,
Properties of the $TiSi_2$/p+n structures formed by ion implantation through silicide and rapid thermal annealing,
J. Appl. Phys. **72**, 75 (1992)

Grambole, D., Herrman, F., and Klabes, R.,
Investigation of oxygen and fluorine distributions using nuclear reaction analysis at the Rossendorf nuclear microprobe,
Nucl. Instr. and Meth. in Phys. Res. B**64**, 399 (1992)

Grambole, D., Herrmann, F., Klabes, R., Hauffe, W., and Behrisch, R.,
Investigation of the deuterium distribution in a JET limiter using the nuclear microprobe and ion beam slope cutting,
Nucl. Instr. and Meth. in Phys. Res. B**68**, 154 (1992)

Grötzschel, R., Hentschel, E. Klabes, R., Kreißig, U., Neelmeijer, C., Assmann, W., and Behrisch, R.,
Elemental analysis of thin layers by elastic heavy ion scattering,
Nucl. Instr. and Meth. B**63**, 77 (1992)

Helming, K., Voitus, W., and Walther, K.,
Progress in texture investigations at the pulsed reactor IBR-2,
Physica B **180** & **181**, 1025 (1992)

Henke, D. and Hentschel, R.,
An ECR Ion Source for Ion Implantation,
Rev. Sci. Instr. **63**, 2538 (1992)

Hentschel, R. and Henke, D,
Oxygen and Carbon Ions from a Reflex Ion Source,
Rev. Sci. Instr. **63**, 2590 (1992)

Jäger, H.-U.,
Modelling of the formation of buried dielectric layers by ion implantation,
Nucl. Instr. and Meth. B**65**, 67 (1992)

Kurbakov, A.I., Rubinova E.E., Sokolov, A.E., Mäder, M., Tempel, A., and Tobisch, J.,
Gamma-ray diffraction study of MBE grown CaF_2/Si(111) Heterostructures,
Cryst. Res. & Technol. **27**, 791 (1992)

Küchler, R.,
Ultrasonic Surface Waves for Studying the Properties of Thin Films,
Phys. stat. sol. (a) **132**, K65 (1992)

Leiss, B., Voitus, W., and Walther, K.,
Neutronentexturanalyse von Dolomitmyloniten aus dem Damara-Orogen/Namibia (Teil 1),
Frankfurter geowiss. Arbeiten, **11**, 120 (1992)

Leiss, B., Helming, K., Siegesmund, S., and Weber, K.,
Neutronentexturanalyse von Dolomitmyloniten aus dem Damara-Orogen/Namibia (Teil 2),
Frankfurter geowiss. Arbeiten, **11**, 253 (1992)

Lohner, T., Skorupa, W., Fried, M., Vedam, K. Nguyen, N., Grötzschel, R., Bartsch, H., and Gyulai, J.,
Comparative study of the effect of annealing of nitrogen-implanted SOI-structures by spectroscopic ellipsometry, XTEM and RBS,
Mat. Sci. and Eng. B**12**, 177 (1992)

Matz, W. and Wieser, E.,
Konzeption für ein Strahlenforschungszentrum Rossendorf,
FZR **92-04**, Rossendorf, März 1992

Matz, W. and Einfeld, D. (verantw. Bearbeiter),
ROSY - Rossendorfer Synchrotronstrahlungsquelle,
FZR **92-10**, Rossendorf, Juni 1992

Neelmeijer, C., Grötzschel, R., Klabes, R., Kreißig, U., Müller, W., and Kruschke, D.,
Simultaneous analysis of Li and B in amorphous thin film glasses using ERDA,
Nucl. Instr. and Meth. B**68**, 231 (1992)

Panknin, D., Richter, F., Bugiel, E., and Erzgräber, H.,
Formation of titanium silicide during rapid thermal annealing: Influence of oxygen,
J. Appl. Phys. **72**, 815 (1992)

Panknin, D., Wieser, E., Grötzschel, R., Skorupa, W., Baither, D., Bartsch, H., Querner, G., and Danzig, A.,
Ion beam synthesis of buried $FeSi_2$ in (100) silicon,
Mat. Science and Engineering, **B12**, 119 (1992)

Pham, M. T.,
Characterization of ion-implanted gate insulator films for use as ion sensitive membrane in ISFETs,
Sensors and Actuators A, **7**, 576 (1992)

Pham, M. T., Hoffmann, W., and Hüller, J.,
Thin insulator films chemically sensibilized by ion implantation for application to ISFET microsensors,
Sensors and Actuators B, **8**, 227 (1992)

Posselt, M., and Biersack, J.P.,
Computer simulation of ion implantation on into crystalline targets,
Nucl. Instr. and Meth. B**64**, 706 (1992)

Posselt, M., Drechsler, L., Grötzschel, R., Klabes, R., Otto, G., Schöneich, A., Sobeslavsky, E., and Syhre, H.,
Particle reflection and reimplantation during grazing incidence implantation of As^+ and B^+ into silicon,
Nucl. Instr. and Meth. B**67**, 443 (1992)

Prokert, F., Balagurov, A. M., Savenko, B. N., and Seglins, J.,
TOF Neutron Diffraction Studies on Weakly Doped Single Crystals of $Sr_xBa_{1-x}Nb_2O_6$ - Investigation of the Influence of Doping on Diffuse Scattering and IC Modulation Structure,
Proc. 20th Int. Spring Conf. Ferroelectricity, Guentersberge, ed. G. Schmidt, Martin-Luther-University, Halle-Wittenberg, 1992, p.35

Rauschenbach, B., Posselt, M., Grötzschel, R., Brecht, E., Linker, G., and Meyer, O.,
Ion mixing of Cu/Ti and Cu/Fe bilayers,
Nucl. Instr. and Meth. B**69**, 277 (1992)

Reuther, H., Wieser, E., Panknin, D., Grötzschel, R., and Skorupa, W.,
Investigation of ion beam synthesized iron silicide by RBS, XRD and Mössbauer spectroscopy (CEMS),
Nucl. Instr. and Meth. in Phys. Res. B**68**, 241 (1992)

Reuther, H.,
A magnetron source for ion implantation,
Nucl. Instr. and Meth. in Phys. Res. B**71**, 87 (1992)

Skorupa, W., Schöneich, J., Grötzschel, R., Wollschläger, K., De Veirman, A., Albrecht, J., and Vöhse, H.,
The buried stacked insulator: A new SOI-structure formed by ion beam synthesis,
Mat. Sci. Eng. **B12**, 63 (1992)

Skorupa, W. Grötzschel, R., Wollschläger, K. Albrecht, J., and Vöhse, H.,
Formation of a buried stacked insulator by ion beam synthesis,
Mat. Res. Soc. Symp. Proc. **235**, 127 (1992)

Skorupa, W., Kögler, R., Voelskow, M., Schmalz, K., Morgenstern, G., and Gaworzewski, P.,
MeV-carbon implantation into silicon: microstructure and electrical properties,
Nucl. Instr. Meth. B**68**, 241 (1992)

Teichert, J. and Janssen, D.,
Time of flight corrected beam blanker for ion beam lithography systems,
Optic 91, 46 (1992)

Tempel, A., and Mäder, M.,
Strain, Stress and Symmetry in Pseudomorphically Grown Epitaxial Layers,
Cryst. Res. & Technol. **27**, 265 (1992)

Uhlemann, J., Schmidt, B., and Lange, P.,
Innovative Techniken für die Mikrodosierung,
Mikroelektronik, Beilage Mikroperipherik/Mikrosysteme, H. **2/3** VDI/VDE-Technologiezentrum Berlin (1992)

Zschau, H.-E., Plier, F., Vogt, J., Otto, G., Duschner, H., Arends, J., Grambole, D., Herrmann, F., Klabes, R., Salomonovich,R., Hulek, Z., and Setvak, M.,
Test of a new standard for fluorine determination with PIGE,
Nucl. Instr. and Meth. B**68**, 158 (1992)

Conference Contributions

Bischoff, L., Hesse, E., Hofmann, G., Naehring, F.-K., Probst, W., Schmidt, B., and Teichert, J.,
High Current FIB System for Micromechanics Application,
Int. Conf. Microcircuit Engineering '92, Erlangen, 21 - 24 Sept. 1992

Borany, J. von, and Kögler, R.,
The influence of preamorphization on the properties of shallow p+n-junctions in silicon radiation detectors,
6th Europ. Symp. on Semiconductor Detectors, Milano, Italy 1992

Brauer, G., Eichhorn, F., Frisius, F., and Kampmann, R.,
Investigation of neutron irradiated Soviet-type reactor pressure vessel steels by small angle neutron scattering, ASTM STP 1175,
16th Int. Symp. on the Effects of Radiation on Materials, Aurora (USA), 23.-25.06.1992

Brauer, G., and Eichhorn, F.,
Considerations about irradiation-induced precipitates in Soviet-type reactor pressure vessel steels,
Meeting IG-RDM, Paris, 16.-20.11.1992

Danzig, A., Querner, G., Wieser, E., and Panknin, D.,
Untersuchung der Silicidbildung an eisenimplantiertem Silicium,
Frühjahrstagung des Arbeitskreises "Festkörperphysik" bei der DPG;
Regensburg, 16.-20.03.1992

Eichhorn, F., Podurets, K. M., and Shilstein, S. Sh.,
Untersuchung von Oberflächen mittels Neutronendoppelkristalldiffraktometrie,
Röto '92, Jena, 17./18.09.1992

Eichhorn, F., and Treimer, W.,
Doppelkristalldiffraktometer mit perfekten Kristallen,
BENSC User Meeting, HMI Berlin, 12./13.10.1992

Friedrich, M., Bürger, W., Curian, H., Hartmann, B., Hentschel, E., Matthes, H., Probst. W., Seidel, M., Turuc, S., Hebert, D., Rothe, T., and Stolz, W.,
Accelerator Mass Spectrometry (AMS) at the Rossendorf 5 MV Tandem Accelerator,
6th Int. Conf. on Electrostatic Accelerators and Associated Boosters,
Padua, June 1-5, 1992

Grambole, D., Herrmann, F., and Hauffe, W.,
Large-depth profiling of hydrogen by line scans of the nuclear microbeam over slope planes cut with an ion beam,
3rd Int. Conf. on Nucl. Microprobe Technology and Applications, Uppsala, Sweden, June 8-12, 1992

Gorski, N.,
Kleinwinkelstreumessung am System $C_{12}E_4 + D_2O$,
Poster auf Verbundtreffen "Forschung mit Neutronen",
Bad Schandau, 29.03.-01.04.1992

Gorski, N., Ostanevic, Yu. M., and Klose, G.,
Form und Größe von $C_{12}E_4$-Mizellen in $C_{12}E_4$-D_2O-Lösung anhand der SANS-Untersuchungen,
Poster auf Verbundtreffen "Forschung mit Neutronen",
Bad Schandau, 29.03.-01.04.1992

Gorski, N., and Ostanevic, Yu. M.,
Critical Mizelle Concentration in AOT + xH_2O + $C_{10}D_{22}$ as determined by Small Angle Neutron Scattering,
VI. ECIS Conference, Graz, Sept. 21-25, 1992

Gorski, N., and Ostanevic, Yu. M.,
Kleinwinkelstreumessung der Systeme AOT + $C_{10}D_{22}$, AOT + 22.3 H_2O+$C_{10}D_{22}$ und AOT + 32.4 H_2O + $C_{10}D_{22}$,
Poster: VI. ECIS Conference, Graz, Sept. 21-25, 1992

Häußler, F., Eichhorn, F., Baumbach, H., and Birkholz, W.,
Strukturbildung in hydratisierendem Zementstein,
Poster auf Verbundtreffen "Forschung mit Neutronen",
Bad Schandau, 29.03.-01.04.1992

Häußler, F., Eichhorn, F., Birkholz, W., and Baumbach, H.,
SANS study of hardening cement pastes and solid state nuclear track detectors,
Int. Seminar on Structural Investigations at Pulsed Neutron Sources,
Dubna, 01.-04.09.1992

Häußler, F., Eichhorn, F., and Baumbach, H.,
SANS studies of hydrating cement pastes,
VI. ECIS Conference, Graz, 21.-25.09.1992

Heera, V., Kögler, R., Skorupa, W., and Grötzschel, R.
Dose rate dependence of the ion beam induced epitaxial crystallization in silicon,
"MRS, Fall Meeting", Boston, USA, Nov. 30-Dez. 4, 1992

Heinig, K.-H., and Janssen, D.,
The structure of GRID lineshapes of single crystals (c-GRID) predicted by molecular dynamics calculations,
Workshop on Applications of High Resolution Gamma Spectroscopy in Studies of Atomic Collisions and Nuclear Lifetimes, Grenoble (France), Oct. 5-7, 1992,
invited lecture

Helming, K., Leiss, B., Siegesmund, S., Voitus, W., Walther, K., and Weber, K.,
Bestimmung von Gesteinstexturen,
Poster auf Verbundtreffen "Forschung mit Neutronen",
Bad Schandau, 29.03.-01.04.1992

Invankina, T. I., Nikitin, A. N., Heinitz, J., and Kovalev, L. A.,
Influence of texture transformations with inclusions on the stress state of an elastic medium,
Poster: XXIII. General Assembly of the European Seismological Commission,
Prague, Sept. 7-12, 1992

Jäger, H.-U.,
An explanation of transient enhanced diffusion and electrical activation of boron in crystalline silicon during post-implantation annealing,
8th Int. Conf. on Ion Beam Modification of Materials (IBMM '92), Heidelberg,
Sept. 7-11, 1992

Jäger, H.-U., Heinig, K.-H., and Posselt, M.,
Computer simulation of ion implantation and diffusion in silicon,
Treffen des Verbundes "Festkörperphysik und Materialforschung mit nuklearen Methoden", Saarbrücken, Oct. 5-7, 1992

Klimanek, P., and Mücklich, A.,
Korngrößenbestimmung mit Hilfe der Neutronen-Großwinkelstreuung,
Poster auf Verbundtreffen "Forschung mit Neutronen",
Bad Schandau, 80, 29.03.-01.04.1992

Klimanek, P., Kschidock, T., Mücklich, A. Lukas, P., and Mikula, P.,
Neutron Diffracion Analysis of Substructures in Polycrystalline Materials,
Poster auf Verbundtreffen "Forschung mit Neutronen",
Bad Schandau, 81, 29.03.-01.04.1992

Kolitsch, A., Hentschel, E., and Richter, E.,
Depth profiles of C, N and O on carbon coated steel surfaces made by IBAD,
Diamond Films '92, Heidelberg, Aug. 31-Sept. 4, 1992

Kolitsch, A., Hentschel, E., and Richter, E.,
Depth profiles of metalloides on carbon coated steel surfaces made by IBAD,
8th Int. Conf. on Ion Beam Modification of Materials (IBMM '92), Heidelberg,
Sept. 7-11, 1992

Kögler, R., Heera, V., Skorupa, W., Glaser, E., and Rück, D.,
Reduced Reverse Temperature of Ion Beam Amorphization/Crystallization for Intermittent Beam Irradiation of Silicon,
8th Int. Conf. on Ion Beam Modification of Materials (IBMM '92), Heidelberg,
Sept. 7-11, 1992

Küchler, R., and Richter, E.,
Schichtcharaktierisierung mittels Ultraschalloberflächenwellen,
Verbundwerkstoffe und Werkstoffverbunde, Chemnitz, Juni 17-19, 1992

Lukas, P., Kulda, J., Mikula, P., Vrana, M., Klimanek, P., and Mücklich, A.,
Utilisation of Neutron Optics with Bent-Crystal Elements for Investigation of Polycrystalline Materials,
Poster auf Verbundtreffen "Forschung mit Neutronen",
Bad Schandau, 113, 29.03.-01.04.1992

Matz, W. and Betzl, M.,
Neutronenstreuung im Forschungszentrum Rossendorf,
Verbundtreffen "Forschung mit Neutronen",
Bad Schandau, 29.03.-01.04.1992

Matz, W. and Einfeld, D.,
Vorstellung des Projektes einer Synchrotronstrahlungsquelle in Rossendorf,
Arbeitstreffen "Nutzung einer künftigen Synchrotronstrahlungsquelle",
Dresden, 15./16.12.1992

Matz, W.,
Nutzung von Synchrotronstrahlungsmethoden für die Ionenstrahlphysik im FZR,
Arbeitstreffen "Nutzung einer künftigen Synchrotronstrahlungsquelle",
Dresden, 15./16.12.1992

Mücklich, A. and Klimanek, P.,
Sample-Induced Errors in Quantitative Texture Analysis from Diffraction Pole Figures,
Abstr. Int. Conf. Accuracy in Powder Diffraction II, Gaithersburg (USA), 34,
Mai 25-29, 1992

Mücklich, A., Betzl, M., Mikula, P., and Lukas, P.,
The Diffractometer of the RCR at the Rez Reactor,
Meeting Application of Nuclear Methods in Solid State Research,
Rossendorf, 03./04.11.1992

Nikitin, A. N., Archipov, I. K., Kurtasov, S. F., and Walther, K.,
The Model of induced anisotropy in crystalline rocks,
Poster: XXIII. General Assembly of the European Seismological Commission,
Prague, Sept. 7-12, 1992

Panknin, D., Wieser, E., Wollschläger, K., Querner G. Grötzschel, R., and Skorupa, W.,
Investigation of Ion Beam synthesized $FeSi_2$ and the α <----> β phase Transition,
Conf. of Technology and Applications of Ion Beams,
Loughborough, England, April 7-10, 1992

Panknin, D., Wieser, E., Skorupa, W., Querner, G., Vöhse, H., and Albrecht, J.,
Formation of Buried Ternary Silicide Layers in Silicon by Ion Beam Synthesis (IBS),
"MRS, Fall Meeting", Boston, USA, Nov. 30-Dez.4, 1992

Panknin, D., Wieser, E., Skorupa, W., Vöhse, H., and Albrecht, J.,
Formation of Buried Ion-Cobalt-Silicide Layers by High Dose Implantation,
8th Int. Conf. on "Ion Implantation Technology", Gainesville, USA,
Sept. 21 - 24, 1992

Pham, M. T., Howitz, S., Hüller, J., Albrecht, J. et. al.,
Spectroscopic and electrochemical properties of ion-sensing membranes fabricated by ion implantation,
4th Int. Meeting on Chemical Sensors, Tokyo, Sept. 1992

Posselt, M.
Chrystal TRIM and its application to investigations on channeling effects in ion implantation,
Invited Paper, Int. Conf. on Computer Simulations of Radiation Effects in Solids (COSIRES 92), Berlin, Aug. 23-28, 1992

Posselt, M.,
Computer simulation of channeling implantation at high and medium energies,
8th Int. Conf. on Ion Beam Modification of Materials (IBMM 92), Heidelberg,
Sept. 7-11, 1992

Posselt, M.,
Particle reflection and re-implantation during ion implantation into non-planar structures,
12th Int. Conf. on the Application of Accelerators in Research and Industry,
Denton (Texas), Nov. 2-5, 1992

Posselt, M.,
Computer simulation of channeling effects in ion implantation,
Symp. A (Beam Solid Interactions), MRS, Fall Meeting, Boston (USA),
Nov. 30-Dez. 4, 1992

Prokert, F. and Aleksandrov, K. S.,
Neustronenstreuuntersuchungen struktureller Phasenübergänge in Elpasolithen,
Verbundtreffen "Forschung mit Neutronen",
Bad Schandau, 11, 29.03.-01.04.1992

Prokert, F.,
"INS studies on Strontium-Barium-Niobate (SBN-45)", HMI-Proposal E1 (X-02-13),
HMI User Meeting, Berlin 12./13.10.1992

Prokert, F., and Aleksandrov, K. S.,
"TA Phonon Study at the Phase Transition of $RbMnCl_3$", HMI-Proposal V2 (FLEX) (X-02-14),
HMI User Meeting, Berlin 12./13.10.1992

Reuther, H. Brand, R. A., and Keune, W.,
High dose implantation of aluminium into iron,
8th Int. Conf. on Ion Beam Modification of Materials (IBMM '92), Heidelberg, Sept. 7-11, 1992

Reuther, H., Brand, R. A., and Keune, W.,
CEMS and DCEMS-Untersuchungen an Al-implantiertem Eisen,
Mößbauer-Kolloquium, Freiberg, Febr. 17-19, 1992

Schmidt, B., von Borany, J., and Schubert, D.,
Application of wet chemical selective etch techniques to the fabrication of thin silicon detectors,
6th Europ. Symp. on Semiconductor Detectors, Milano, Febr. 24-26, 1992

Schwarz, A., Schmidt, B., Bley, P., Heim, H., Menz, W., and Vollmer, J.,
Techniken zur Entwicklung fluidischer Mikrostrukturen,
Aachener Fluidikkolloquium, Aachen, 17.-19.03.1992

Skorupa, W., Kögler, R., Schmalz, K., Gemonzenovski, P., Morgenstern, G., and Syhre, H.,
Iron Gettering and Doping in Silicon Due to MeV-Carbon-Implantation,
8th Int. Conf. on "Ion Implantation Technology", Gainesville, USA,
Sept. 21 - 24, 1992

Skorupa, W.,
Ionenstrahlsynthese vergrabener Compoundschichten,
Arbeitstreffen des BMFT-Verbundes "Festkörperphysik und Materialforschung mit nuklearen Methoden", Saarbrücken, Oct. 4 - 7, 1992

Stock, D., and Heinig, K.-H.,
Molecular dynamics simulation of disordering of silicon induced by low-energy collision cascades,
Symp. A (Beam Solid Interactions), MRS, Fall Meeting, Boston (USA),
Nov. 30-Dez. 4, 1992

Voitus, W., Heinitz, J., Walther, K., and Isakov, N. N.,
Neutronengraphische Bestimmung von Polfiguren am Diffraktometer NSWR,
Poster auf Verbundtreffen "Forschung mit Neutronen",
Bad Schandau, 29.03.-01.04.1992

Vrana, M., Lukas, P., Mikula, P., Klimanek, P., Alefeld, B., and Mücklich, A.,
Strain Measurements on Neutron Three Axis Setup Employing Cylindrically Bent Perfect Crystals,
Meeting Application of Nuclear Methods in Solid State Research,
Rossendorf, 03./04.11.1992

Wieser, E.,
Use of Accelerators in Material Research, (Invited Paper)
3rd European Particle Accelerator Conference, Berlin,
March 24 - 28, 1992

Wieser, E., Panknin, D., Skorupa, W., Querner, G., Henrion, W., and Albrecht, J.,
Ion Beam Synthesis of Ternary $(Fe_{1-k}Co_k)Si_2$,
8th Int. Conf. on Ion beam modification of materials (IBMM '92), Heidelberg,
Sept. 7 - 11, 1992

Seminars at other Institutes

Albrecht, J., Koch, B., and Pham, M. T.,
Bestimmung der Tiefenverteilung von Na, Ca und Al in dünnen Isolatorschichten mit verschiedenen Analysetechniken,
Tagung der DPG, Regensburg, März 1992

Bischoff, L. and Teichert, J.,
Focused Ion Beam Activities in Rossendorf,
Österreichisches Forschungszentrum Seibersdorf, 11.11.1992

Gorski, N.,
Bestimmung der CMC-Werte reverser Mizellen mit wäßrigem Kern mit Hilfe der Neutronenkleinwinkelstreuung (SANS),
Uni Bayreuth, Physik.-chem. Institut I, 29.10.1992

Heinig, K.-H.,
Hochauflösende Gammaspektroskopie Doppler-verbreiteter Linien (Molekular-dynamische Simulation der Abbremsung der Rückstoßkerne in kristallinen Targets),
Seminarvortrag am Institut für Kern- und Hadronenphysik, FZR, 2.11.1992

Howitz, S.,
Selektives Si-Si-Waferbonden und selektives Si-Glass-Anodic Bonding mittels Ionenimplantation,
TU Berlin, 12.03.1992

Howitz, S., Pham, M. T., and Hüller, J.,
Schwermetallionen ISFET durch Ionenstrahlsynthese,
AIF-Projektvorstellung, Frankfurt/M., 29.10.1992

Howitz, S. and Pham, M. T.,
Entwicklung eines integrierten ISFET-Fluidik-Mikrosystems zur dynamischen ionometrischen Meßwerterfassung,
Statusseminar SSWA-Projekt, Fraunhofer Institut IMS-2 Dresden, Dezember 1992

Kolitsch, A., Hentschel, E., and Richter, E.,
Wear reduction by ion implantation assisted deposition technology and application of ion beams,
Loughborough University of Technology, April 7-10, 1992

Kreißig, U.,
Simultaneous light element analysis of Tokamak inner wall samples by Heavy Ion ERD,
Vortrag auf der 12. Int. Conf. on the Application of Accelerators in Research and Industry, Denton, USA, Nov. 2-5, 1992

Matz, W.,
Projekt einer Synchrotronstrahlungsquelle in Rossendorf für die Materialforschung,
Physikalisches Kolloquium, TU Chemnitz-Zwickau, Chemnitz, 30.11.1992

Matz, W. and Wieser, E.,
Strahlenforschungszentrum Rossendorf,
Festkolloquium zum 65. Geburtstag von Prof. Dr. W. Häfele,
Rossendorf, 22.04.1992

Pham, M. T.,
Ionenimplantation zur Herstellung von Gatemembranen für ISFET-Differenz-messungen,
Statusseminar "Ionensensitive Feldeffekttransistoren",
Forschungsinstitut "Kurt Schwabe" Meinsberg, Mai 1992

Posselt, M.,
Computer simulation of ion implantation using the program Crystal-TRIM,
Seminarvortrag, IBM T.J. Watson Research Center, Yorktown Heights (USA),
9.11.1992

Posselt, M.,
Computer simulation of ion implantation into single-crystalline silicon using the program Crystal-TRIM,
Seminarvortrag, Theoretical Modeling Department, IBM Semiconductor Research and Development Center, East Fishkill Facility, Hopewell Junction (USA),
12.11.1992

Posselt, M.,
Computer simulation of channeling effects in ion implantation,
Seminarvortrag, AT&T Bell Laboratories, Murray Hill (USA),
17.11.1992

Richter, E.,
Werkstoffmodifizierung mittels Ionenstrahltechnik,
Dresdner Dünnschichtseminar, Dresden, Febr. 1992

Skorupa, W.
Hochenergieimplantation,
Symp. "20 Jahre Tandemgenerator des FZR", Rossendorf, 2.11.1992

Teichert, J.,
Der feinfokussierte Ionenstrahl als ein Werkzeug zur Mikrostrukturierung,
Institut für Halbleiterphysik, Frankfurt/O., 27.10.1992

Wieser, E.,
Use of ion beams at the Research Center Rossendorf,
JAERI - Takasaki Radiation Research Establishment, Takasaki, 12.11.1992

Wieser, E.,
Nutzung von Ionenbeschleunigern in der Materialforschung,
DESY Hamburg, 3.6.1992

Personnel

Scientific Staff

Dr. M. Betzl
Dr. L. Bischoff
Dr. J. von Borany
Dr. W. Bürger
Dr. F. Eichhorn
Dr. M. Friedrich
Dr. D. Grambole
Dr. R. Grötzschel
Dr. R. Günzel
Dr. V. Heera
Dr. K.-H. Heinig
D. Henke
Dr. R. Hentschel
Dr. S. Howitz
Dr. J. Hüller
Dr. H.-U. Jäger
Dr. A. Kolitsch
Dr. R. Kögler
Dr. U. Kreißig
R. Küchler
Dr. W. Matz
Dr. A. Mücklich
Dr. C. Neelmeijer
Dr. D. Panknin
Dr. M.T. Pham
Dr. M. Posselt
Dr. F. Prokert
Dr. H. Reuther
Dr. E. Richter
Dr. H. Seifarth
Dr. W. Skorupa
Dr. B. Schmidt
Dr. J. Schöneich
Dr. J. Steffen
Dr. J. Teichert
Dr. H. Tyrroff
Dr. M. Voelskow
Dr. K. Walther
Prof. E. Wieser

Technical Staff

J. Altmann
R. Aniol
I. Beatus
W. Boede
K.-D. Butter
W. Gäßner
B. Gebauer
H.-J. Grahl
P. Hartmann
H. Hempel
F. Herrmann
G. Hofmann
R. Hüller
M. Iseke
S. Klare
R. Kliemann
L. Kumpf
G. Küster
D. Maul
M. Mäder
M. Mißbach
K. Müller
F. Nötzold
W. Probst
A. Protze
P. Reichel
B. Richter
M. Roch
E. Rost
C. Rußig
K. Sommerfeld
B. Scheumann
H. Schluttig
E. Schmidt
G. Schnabel
J. Schneider
A. Scholz
J. Schröter
C. Schulenberg
U. Strauch
K. Thiemig
H. Thümer
S. Turuc
A. Vetter
A. Weise
I. Winkler

Postgraduate Students

T. Chudoba
J. Goerigk
A. Hempel
T. Henkel
E. Hesse
R. Mathar
S. Reiß
R. Weber